February 24, 2021

TECHNICAL PROPOSAL

SND@LHC

Scattering and Neutrino Detector at the LHC

SND@LHC Collaboration

Abstract

SND@LHC is a proposed, compact and stand-alone experiment to perform measurements with neutrinos produced at the LHC in an hitherto unexplored pseudo-rapidity region of $7.2 < \eta < 8.6$, complementary to all the other experiments at the LHC. The experiment is to be located 480 m downstream of IP1 in the unused TI18 tunnel. The first phase aims at operating the detector throughout LHC Run 3 to collect a total integrated luminosity of $150\,\mathrm{fb}^{-1}$.

Following the review of the Letter of Intent [1], submitted in August 2020, LHCC recommended the collaboration to proceed with the preparation of a Technical Proposal (TP), reported herein.

CERN-LHCC-2021-003 / LHCC-P-016
24/02/2021

C. Ahdida[24], R. Albanese[9,c,g], A. Alexandrov[9,19,21,c], M. Andreini[24], A. Anokhina[22], C. Baldanza[7], A. Bay[25], P. Bestmann[24], C. Betancourt[26], I. Bezshyiko[26], A. Blanco[33],M. Bogomilov[1], K. Bondarenko[24,25], W.M. Bonivento[8], P. Boisseaux-Bourgeois[24], A. Boyarsky[18,d], L. Buonocore[26], A. Buonaura[26], S. Buontempo[9], V. Cafaro[7], M. Callignon[24], T. Camporesi[24], M. Campanelli[30], V. Canale[9,c], F. Cerutti[24], N. Charitonidis[24], M. Chernyavskiy[19], K.-Y. Choi[17], S. Cholak[25], V. Cicero[7], A.P. Conaboy[3], L. Congedo[6,a], O. Crespo[24], M. Cristinziani[4], A. Crupano[7], G.M. Dallavalle[7], A. Datwyler[26], N. D'Ambrosio[10], A. Dashkina[21], J. De Carvalho Saraiva[33], P.T. De Bryas Dexmiers D'Archiac[25], G. De Lellis[9,21,c], M. de Magistris[9,c], A. De Roeck[24], A. De Rujula[31], M. De Serio[6,a], D. De Simone[26], L. Dedenko[22], A. Di Crescenzo[9,c], L. Di Giulio[24], A. Dolmatov[20], O. Durhan[27], D. Fasanella[7], F. Fedotovs[30], M. Ferrillo[26], M. Ferro-Luzzi[24], R.A. Fini[6], P. Fonte[33],R. Fresa[9,c], G. Galati[9,c], J. Gall[24], R. Garcia Alia[24], V. Gentile[9,21,c], V. Giordano[7], A. Golovatiuk[9,c], A. Golutvin[29,21], P. Gorbounov[24], M. Gorshenkov[21], E. Graverini[25], J.-L. Grenard[24], A.M. Guler[27], G.J. Haefeli[25], E.van Herwijnen[21], G. Iaselli[6,a], P. Iengo[9,24], S. Ilieva[1] A Infantino[24], A. Iuliano[9,c], R. Jacobsson[24], M. Jonker[24], C. Kamiscioglu[27,f], Y. Karyotakis[32], E. Khalikov[22], Y.G. Kim[14], S.H. Kim[14], D.I. Kolev[1], M. Komatsu[11], N. Konovalova[19,21], S. Kovalenko[34], I. Krasilnikova[21], S. Kuleshov[34], H.M. Lacker[3], O. Lantwin[26,21], A. Lauria[9,c], K.S. Lee[16], K.Y. Lee[13], N. Leonardo[33], G. Lerner[24], S. Lo Meo[7,b], V.P. Loschiavo[9,g], L. Lopes[33], A. Magnan[29], M. Maietta[24], A. Malinin[20], Y. Maurer[24], A.K. Managadze[22], S. Marsh[24], A. Miano[9,c], A. Mikulenko[18], A. Montanari[7], M.C. Montesi[9,c], T. Naka[12], F.L. Navarria[7], P. Ninin[24], S. Ogawa[12], N. Okateva[19,21], J. Osborne[24], N. Owtscharenko[4], P.H. Owen[26], M. Ovchynnikov[18], B.D. Park[13], G. Passeggio[9], A. Pastore[6], M. Patel[29,21], L. Patrizii[7,b], A. Petrov[20], D. Podgrudkov[22], G.L. Petkov[1], K. Petridis[28], N. Polukhina[19,21,e], D. Prelipcean[24], A. Prota[9,c], F. Queiroz[35], A. Quercia[9,c], F. Ratnikov[23], F. Redi[25], A. Reghunath[3], A.B. Rodrigues Cavalcante[25], J. Rodrigues Fernandez[24], T. Roganova[22], T. Rovelli[7,b], O. Ruchayskiy[2], T. Ruf[24], M. Sabate Gilarte[24], F. Sanchez Galan[24], P. Santos Diaz[24], O. Schneider[25], G. Sekhniaidze[9], N. Serra[26,21], M. Shaposhnikov[25], T. Shchedrina[19,21], L. Shchutska[25], V. Shevchenko[20,21], H. Shibuya[12], S. Shirobokov[29], E. Shmanin[21], S. Simone[6,a], G. Sirri[7,b], G. Soares[33],J.Y. Sohn[13], M. Souaya[24], N. Starkov[19,21], J.L. Tastet[2], I. Timiryasov[25], V. Tioukov[9], N. Tosi[7,b], C. Trippl[25], F. Tramontano[9,c], R. Tsenov[1], E. Ursov[22], A. Ustyuzhanin[23,21], G. Vankova-Kirilova[1], C. Vendeuvre[24], C. Visone[9,c], R. Wanke[5], J.-K. Woo[15], C.S. Yoon[13], J. Zamora-Saa[34],E. Zaffaroni[25]

[1] *Faculty of Physics, Sofia University, Sofia, Bulgaria*
[2] *Niels Bohr Institute, University of Copenhagen, Copenhagen, Denmark*
[3] *Humboldt-Universität zu Berlin, Berlin, Germany*
[4] *Department Physik, Universität Siegen, Siegen, Germany*
[5] *Institut für Physik and PRISMA Cluster of Excellence, Johannes Gutenberg Universität Mainz, Mainz, Germany*
[6] *Sezione INFN di Bari, Bari, Italy*
[7] *Sezione INFN di Bologna, Bologna, Italy*
[8] *Sezione INFN di Cagliari, Cagliari, Italy*
[9] *Sezione INFN di Napoli, Napoli, Italy*
[10] *Laboratori Nazionali dell'INFN di Gran Sasso, L'Aquila, Italy*

[11] Nagoya University, Nagoya, Japan
[12] Toho University, Funabashi, Chiba, Japan
[13] Physics Education Department & RINS, Gyeongsang National University, Jinju, Korea
[14] Gwangju National University of Education, Gwangju, Korea
[15] Jeju National University, Jeju, Korea
[16] Korea University, Seoul, Korea
[17] Sungkyunkwan University, Suwon-si, Gyeong Gi-do, Korea
[18] University of Leiden, Leiden, The Netherlands
[19] P.N. Lebedev Physical Institute (LPI RAS), Moscow, Russia
[20] National Research Centre 'Kurchatov Institute', Moscow, Russia
[21] National University of Science and Technology 'MISiS', Moscow, Russia
[22] Skobeltsyn Institute of Nuclear Physics of Moscow State University (SINP MSU), Moscow, Russia
[23] National Research University Higher School of Economics, Moscow, Russia
[24] European Organization for Nuclear Research (CERN), Geneva, Switzerland
[25] École Polytechnique Fédérale de Lausanne (EPFL), Lausanne, Switzerland
[26] Physik-Institut, Universität Zürich, Zürich, Switzerland
[27] Middle East Technical University (METU), Ankara, Turkey
[28] H.H. Wills Physics Laboratory, University of Bristol, Bristol, United Kingdom
[29] Imperial College London, London, United Kingdom
[30] University College London, London, United Kingdom
[31] Inst. de Estructura de la Materia, Consejo Superior de Investigaciones Cientificas (CSIC), Madrid, Spain
[32] Laboratoire d'Annecy-le-Vieux de Physique des Particules (LAPP), Annecy-le-Vieux, France
[33] Laboratory of Instrumentation and Experimental Particle Physics (LIP), Lisbon, Portugal
[34] Universidad Andres Bello, Department of Physics, Santiago, Chile
[35] International Institute of Physics at the Federal University of Rio Grande do Norte, Rio Grande do Norte, Brazil
[a] Università di Bari, Bari, Italy
[b] Università di Bologna, Bologna, Italy
[c] Università di Napoli "Federico II", Napoli, Italy
[d] Taras Shevchenko National University of Kyiv, Kyiv, Ukraine
[e] National Research Nuclear University (MEPhI), Moscow, Russia
[f] Ankara University, Ankara, Turkey
[g] Consorzio CREATE, Napoli, Italy

Contents

Executive Summary **6**

1 Introduction **7**

2 Physics goals and detector concept **8**
- 2.1 Neutrinos . . . 10
- 2.2 Feebly Interacting Particles . . . 13
- 2.3 Detector concept . . . 15

3 Detector environment **19**
- 3.1 Detector geometry constraints . . . 19
  - 3.1.1 Proton-beam crossing angle . . . 20
- 3.2 Backgrounds in TI18 . . . 20
  - 3.2.1 Muon flux . . . 21
  - 3.2.2 Neutrons and K_Ls from muon DIS . . . 21
  - 3.2.3 Thermal neutrons . . . 23

4 Veto system **25**
- 4.1 Overview . . . 25
- 4.2 Mechanics . . . 25
- 4.3 Readout and powering . . . 25
- 4.4 Calibration . . . 26
- 4.5 Cost and schedule . . . 26

5 Target and vertex detector **29**
- 5.1 Overview . . . 29
- 5.2 Target walls . . . 30
  - 5.2.1 Emulsion films . . . 30
  - 5.2.2 Tungsten target . . . 30
  - 5.2.3 Target assembly . . . 31
  - 5.2.4 Exchange of emulsion films . . . 31
  - 5.2.5 Chemical development . . . 32
  - 5.2.6 Requirements for the emulsion facility . . . 32
- 5.3 Mechanics . . . 33
- 5.4 Cooling and neutron shield . . . 34
- 5.5 Microscopy . . . 34
- 5.6 Cost and schedule . . . 35

6 Target trackers and electromagnetic calorimeter **38**
- 6.1 Overview . . . 38
- 6.2 Mechanics . . . 39
- 6.3 Powering . . . 39
- 6.4 Readout . . . 39
- 6.5 Calibration . . . 41
- 6.6 Alignment . . . 41
- 6.7 Cost and schedule . . . 41

7 Muon system and hadronic calorimeter **43**
7.1 Overview . . . 43
7.2 Mechanics . . . 44
7.3 Readout and powering . . . 44
7.4 Calibration . . . 45
7.5 Alignment . . . 45
7.6 Cost and schedule . . . 46

8 Data acquisition **50**
8.1 DAQ architecture . . . 50
8.2 DAQ electronics . . . 50
8.3 LHC signals and TTC system . . . 52
8.4 Event building, data-quality and storage . . . 53
8.5 Detector Control System (DCS) . . . 54
8.6 DAQ software . . . 54
8.7 Cost and schedule . . . 55

9 Installation and integration **57**
9.1 Component transport . . . 57
9.2 Detector services . . . 58
9.3 Detector alignment during installation . . . 62
9.4 Integration . . . 63
9.5 Radiation effects to electronics (R2E) . . . 64
9.6 Radiation Protection . . . 65
9.7 Personnel access . . . 65
9.8 Schedule and cost . . . 65

10 Commissioning **67**

11 Safety **67**

12 Offline software and computing **69**
12.1 FLUKA simulation framework . . . 69
12.2 Detector simulation . . . 71
12.3 Data reconstruction . . . 73
12.3.1 Analysis tools . . . 74
12.4 Performance studies . . . 75
12.4.1 Neutrino detection . . . 75
12.4.2 Neutrino energy measurement . . . 77
12.5 Software and computing infrastructure . . . 80
12.6 Cost and schedule . . . 80

13 Physics performances **82**
13.1 Neutrino physics . . . 82
13.1.1 Charmed-hadron production in *pp* collisions . . . 82
13.1.2 Lepton flavour universality test in ν interactions . . . 88
13.1.3 Measurement of the NC/CC ratio . . . 91
13.1.4 Neutrino-induced charm production . . . 92

13.1.5 Summary of physics results with neutrinos 95
13.2 Search for Feebly Interacting Particles 95
13.2.1 Scattering off nucleons 95
13.2.2 Elastic scattering off electrons 99

14 Overall cost and schedule 101
14.1 Cost 101
14.2 Schedule 103
14.3 Risk analysis 105

15 Organisation 106

16 Future prospects 107

Executive Summary

SND@LHC is a proposed, compact and stand-alone experiment to perform measurements with neutrinos produced at the LHC in a hitherto unexplored pseudo-rapidity region of $7.2 < \eta < 8.6$, complementary to all the other experiments at the LHC, including FASER.

The SHiP collaboration expressed interest in performing measurements of neutrinos at the LHC with a document submitted to the LHCC in Feb. 2020. After discussions with XSEN and forming a new collaboration, SND@LHC submitted a Letter of Intent in August 2020. Following investigations that confirmed the possibility of preparing the experimental area and installing the detector during 2021, with the LHC in cold operating conditions, the LHCC recommended the collaboration to proceed with the preparation of a Technical Proposal, reported herein.

The experiment is to be located 480 m downstream of IP1 in the unused TI18 tunnel. The detector is composed of a hybrid system based on an 800 kg target mass of tungsten plates, interleaved with emulsion and electronic trackers, followed downstream by a muon system. The configuration allows efficiently distinguishing between all three neutrino flavours, opening a unique opportunity to probe physics of heavy flavour production at the LHC in the region that is not accessible to ATLAS, CMS and LHCb. The detector concept is also well suited to searching for Feebly Interacting Particles via signatures of scattering in the detector target. The first phase aims at operating the detector throughout Run 3 to collect a total of $150\,\mathrm{fb}^{-1}$.

With data from Run 3, SND@LHC will be able to study about two thousand high-energy neutrino interactions. The performance studies show that the charmed-hadron production in the SND@LHC pseudo-rapidity range can be determined with a statistical and systematic accuracy of 5% and 35%, respectively. The result may be further used to constrain the gluon PDF in the very-small-x region. Unique tests of lepton flavour universality with neutrino interactions can reach 30% statistical and 22% systematic uncertainty for ν_e and ν_τ, and 10% for both uncertainties for ν_e and ν_μ at high energy.

The SND@LHC schedule assumes project approval by end of March 2021 and start of data taking with a full detector in 2022. It is recognised that the preparatory works and detector installation in 2021 are on a challenging critical path. However, the definition of the infrastructure and services is mature, and the preliminary plan for the preparatory works has been elaborated in detail with the CERN equipment groups and the LHC coordination. The detector is based on well-known technologies, no further R&D is needed, and the collaboration has significant experience with the technologies from OPERA, SHiP, SHiP-charm, and LHCb. Several technological changes have been made to the detector since the LoI, to further optimise the construction time and the resources required. The sub-detector designs have been consolidated and are ready to be reviewed for production. The preparations for the detector construction are proceeding as expected in terms of the availability of material and personnel. The costs of the sub-systems are based on commercial offers, or similar systems recently produced elsewhere. The total cost of the detector is estimated to 1.5 MCHF. Owing to already requested funding and reuse of detector components, 40% of the detector cost can be considered pledged.

On the longer term, the collaboration intends to continue detector R&D in order to develop a system that could also operate at the HL-LHC. In addition to collecting significantly more statistics, the aim is to investigate the possibility of performing measurements in the range of pseudo-rapidity $\sim 4-9$ to overlap with LHCb, in order to constrain the heavy-flavour production, and so expand the physics programme with more complete measurements of neutrino interactions of all flavours.

1 Introduction

SND@LHC is a compact experiment proposed to make measurements with neutrinos of all three neutrino flavours from the LHC in the pseudo-rapidity range of $7.2 < \eta < 8.6$. This range of pseudo-rapidity is currently unexplored [2], and a large fraction of the corresponding neutrinos originate from charmed-hadron decays. Thus, neutrinos can be seen as a probe of heavy-flavour production in a region that is not accessible to the other LHC experiments. Together with the FASERν [3] experiment, SND@LHC will first observe the neutrinos produced by a collider, in an energy range which is also otherwise inaccessible at accelerators. In addition to distinct detector concepts, SND@LHC and FASERν will explore different angular ranges in which the relative compositions of the various sources of neutrinos are different. Hence, the neutrino physics programmes of the two experiments are complementary. Moreover, SND@LHC is sensitive to Feebly Interacting Particles (FIP) through scattering off atoms in the detector target. The direct-search strategy gives the experiment sensitivity in a region of the FIP mass-coupling parameter space that is complementary to other indirect searches.

In order to shield the detector from most of the charged particles produced in the LHC collisions, SND@LHC is to be located in the unused TI18 tunnel, 480 m downstream of the ATLAS interaction point. Measurement of neutrino energy and an efficient charged lepton identification are essential features to distinguish the three flavours in neutrino interactions, and to identify and study the corresponding neutrino source. These features were thus the main drivers in the design of the SND@LHC apparatus. SND@LHC is proposed for installation in TI18 in 2021, during the Long Shutdown 2, in time to collect 150 fb^{-1} of data in 2022–24 during Run 3 of the LHC.

The detector concept and the basic physics goals of the SND@LHC experiment have been described in the Letter of Intent [1]. This document gives more detail about the physics potential in the exploitation of both neutrino measurements and FIP searches, including light dark matter candidates, and about the technical aspects of the experiment. Section 2 gives an overview of the physics and the experiment. We then describe the detector environment in Section 3. Sections 4 to 8 describe the sub-systems of the detector, starting with the veto system that flags events with charged particles entering the detector from the front. It is followed by the emulsion target, which acts as a vertex detector, and the target trackers that provide the time stamp to the events reconstructed in the emulsion. The combination of the emulsion target and the target tracker also acts as an electromagnetic calorimeter. The target system is followed by the muon identification system, which also serves as a hadronic calorimeter. The last detector section describes the data acquisition and online systems. In Sections 9 to 11 we give details about the installation and integration, commissioning, and safety aspects. We discuss offline software and computing in Section 12, the physics performance in Section 13 and summarise the overall cost and schedule in Section 14. Section 15 summarises the organisational structure of the Collaboration and, finally, Section 16 reports possible future prospects of this physics programme.

2 Physics goals and detector concept

Neutrinos allow precise tests of the Standard Model (SM) [4, 5, 6, 7], and are a probe for new physics [8, 9], in an otherwise veiled view of the Universe [10]. Neutrino interactions have been measured in the energy regime below 350 GeV. An overview of all available ν cross-section measurements is given in [11]. Recently, the IceCube collaboration reported a few tens of events in the region 10 TeV–1 PeV [12]. The existing measurements of the neutrino cross-section in Figure 1 show that the region between 350 GeV and 10 TeV is currently unexplored [13]. Indeed, measurements of neutrino interactions in the last decades were mainly performed at low energies, where neutrino oscillations over the available baselines are enhanced.

The data reported in Figure 1 are mostly from measurements of muon neutrinos, see e.g. [11] and references therein. Electron neutrino measurements are rather scarce and mostly below 12 GeV. The Gargamelle [14] experiment reported ν_e-nucleon cross-sections up to 12 GeV. At higher energies, E53 [15] reported $\nu_e - \nu_\mu$ universality in the neutrino cross-sections for energies up to 200 GeV with a bubble chamber. HERA studied the reaction $e^- p \to \nu_e X$ by requiring missing energy in the final state. In their SM interpretation of the missing energy as due to an electron neutrino, they showed results consistent with the SM neutrino cross-section, constraining the inverse reaction of $\nu_e p$ interactions with an accuracy of 2÷3%, at the equivalent fixed target neutrino energy of 50 TeV [16]. As far as tau neutrinos are concerned, only a handful of events have been recorded by the DONUT [17] and OPERA [18, 19] experiments. The DONUT experiment at Fermilab performed the first observation of tau neutrinos using a 800 GeV proton beam dump onto a tungsten target. The experiment observed nine tau neutrino candidates [17], without distinguishing between neutrinos and anti-neutrinos, and did not study interactions of other neutrino types. OPERA observed ten tau-neutrino candidates coming from muon-neutrino oscillations and also detected 35 electron-neutrino interactions [20]. The emulsion technology developed by OPERA in a hybrid detector proved to be capable of identifying all three neutrino flavours.

Neutrinos in proton–proton interactions at the CERN LHC arise promptly from leptonic W and Z decays, and b and c decays, and are produced in the subsequent decays of pions and kaons. LHC neutrinos offer the unique possibility of observing neutrino interactions in the largely unexplored range from a few hundred GeV to a few TeV in a laboratory. Furthermore, the contribution of the τ flavour to the LHC neutrino flux is sizeable. The use of LHC as a neutrino factory was first envisaged about 30 years ago [21, 22, 23, 24], also for the then undiscovered ν_τ [22, 25]. The idea suggested a detector intercepting the very forward flux ($\eta > 7$) of neutrinos (about 5% have τ flavour) from b and c decays. Recently, it was pointed out [26] that at larger angles ($4 < |\eta| < 5$) leptonic W and Z decays also provide an additional contribution to the neutrino flux, of which one third has τ flavour. In these events, the charged lepton could be detected in coincidence at the collision point by the existing collider detector, thus providing an independent determination of the neutrino flavour. Today, two effects make it possible and particularly interesting to add a compact neutrino detector at the LHC. The high intensity of proton-proton collisions achieved by the machine turns into a large expected neutrino flux in the forward direction, and the high neutrino energies imply relatively large neutrino cross-sections. As a result, even a detector with a relatively modest size to fit into one of the existing underground areas has significant physics potential. Machine-induced backgrounds decrease rapidly while moving along and away from the beam line. A detailed study of a possible underground location for a neutrino detector was conducted in 2018 [27], during the LHC Run 2.

Four locations were considered to host a possible neutrino detector: the CMS quadrupole region (25 m from the CMS Interaction Point (IP)), UJ53 and UJ57 (90 and 120 m from the CMS IP), RR53 and RR57 (240 m from the CMS IP), TI18 (480 m from the ATLAS IP). The potential sites were studied on the basis of expected neutrino rates, flavour composition and energy spectrum, predicted backgrounds, and in-situ measurements performed with a nuclear emulsion detector and radiation monitors. TI18 emerged as the most favourable location. Assuming a luminosity of 150 fb^{-1} in the LHC Run 3, a detector with a mass of about 1 tonne located in TI18 could observe and study about two thousand high-energy neutrino interactions, including all neutrino flavours [27]. The FASER collaboration [28] in 2019 proposed to extend its physics case and also measure neutrinos with a detector, FASERν [3], located in the TI12 tunnel, on the opposite side of the ATLAS IP. The location is on-axis at $\eta > 9$. The role of an off-axis setup has been emphasised in a recent paper [29].

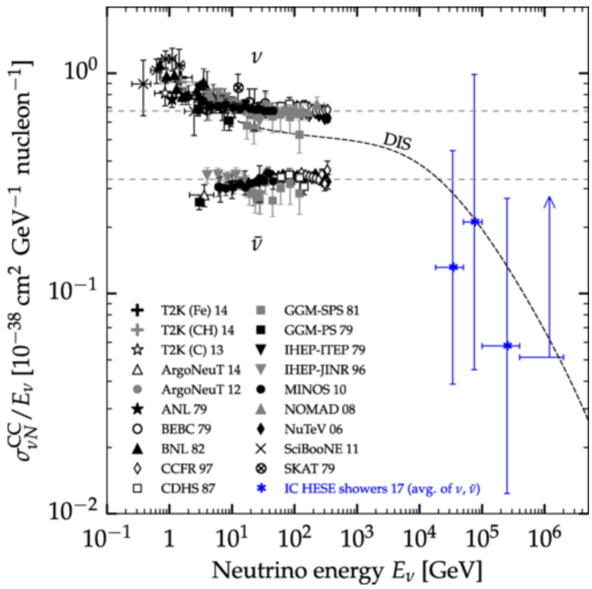

Figure 1: Available measurements of the neutrino cross-section [13]. The thick dashed curve (DIS) is a prediction of deep-inelastic scattering, averaged between ν and $\bar{\nu}$.

The SND@LHC Collaboration in 2020 proposed [1] a new detector to be located off-axis in TI18. The detector will operate during Run 3 and measure the $pp \to \nu X$ cross-section in the $7.2 < \eta < 8.6$ range, for all three neutrino flavours. The off-axis location is ideally suited to explore heavy-quark production in a pseudo-rapidity range that is still unexplored, because it is far beyond the reach of current LHC experiments. Apart from ν_τs and $\bar{\nu}_\tau$s originating exclusively from heavy-hadron decays, ν_e and $\bar{\nu}_e$ mostly come from charmed hadron decays with a small contamination from kaons at low energies where the interaction cross-section with the detector is lower, while ν_μs and $\bar{\nu}_\mu$s show a sizeable contribution from pion and kaon decays. In the proposed η range, ν_μs from π and K decays show a softer energy spectrum. This allows distinguishing between the components from charm and from π/K decays through the neutrino-energy measurement.

The experiment's neutrino yield depends on the neutrino flux and the neutrino-interaction cross-section. The main uncertainty in the flux of neutrinos originating from heavy quarks lies in the production. Consequently, measuring the high-energy neutrinos provides a direct insight in the heavy-flavour production.

In the following we illustrate the main physics goals of the SND@LHC detector and the experimental layout.

2.1 Neutrinos

Figure 2 shows the flux of the different neutrino and anti-neutrino types in the (η, E_ν) plane. In Run 3, SND@LHC has three goals in the analysis of neutrinos, described in this section. The corresponding sensitivities are derived in Section 13. Additional goals such as the measurement of the strange-quark content of the nucleons using neutrino interactions with charmed hadrons in their final state are also mentioned.

Charmed-hadron production in pp collisions

Charmed-hadron production in pp collisions has been studied at the LHC at smaller pseudo-rapidity. The LHCb experiment explores the range closest to SND@LHC: LHCb has measured charm and beauty production at high accuracy at $\eta < 4.5$ [2]. Figure 3 shows the energy spectrum of incoming neutrinos and anti-neutrinos in the pseudo-rapidity range covered by the SND@LHC detector, $7.2 < \eta < 8.6$, normalised to $150\,\mathrm{fb}^{-1}$. In this η range, electron neutrinos and anti-neutrinos are predominantly produced by charmed-hadron decays. As a result, SND@LHC is capable of measuring charmed-hadron production indirectly through the observation of electron neutrinos and anti-neutrinos.

The simulation, developed by the CERN EN-STI team and described in Section 12.1, includes a detailed propagation of particles through all the machine elements. It predicts that 10% of the ν_e and $\bar{\nu}_e$ that interact in the detector originate from kaon decays, in particular from decays of K^0s, and have energies below 200 GeV. The contribution of beauty-hadron decays at IP1 has been estimated with the help of the Pythia8 event generator to be about 3%. Therefore, if one assumes that the deep-inelastic charged-current cross-section of the electron neutrino follows the SM prediction, as also supported by the HERA results in their SM interpretation [16], electron neutrinos can be used as a probe of the production of charm in the pseudo-rapidity range of SND@LHC, after unfolding the instrumental effects and subtracting the K contribution. A procedure has been developed that starts from the electron-neutrino energy spectrum, and unfolds the energy-resolution effects to predict the energy spectrum of the incoming electron-neutrino flux. At this stage, data can be used to measure the $pp \to \nu_e X$ cross-section with an accuracy of 15%, dominated by the systematic uncertainty of the unfolding procedure.

Different event generators produce different levels of kaon contribution, but all agree that the events are restricted to energies below 200 GeV. When subtracting the kaon contribution, the uncertainty on the kaon production gives an additional uncertainty of 20% in the heavy-quark production.

A detailed procedure with a full simulation has been setup to correlate the yield of charmed hadrons in a given η region with the neutrinos in the measured η region, yielding another 25% systematic uncertainty in the charmed-hadron yield. The procedure is described in detail in Section 13. As a result, the measurement of the charmed-hadron production in pp collision can be done with a statistical uncertainty of about 5% while the leading contribution to the uncertainty is the systematic error of 35%. From there, one can also derive information on the

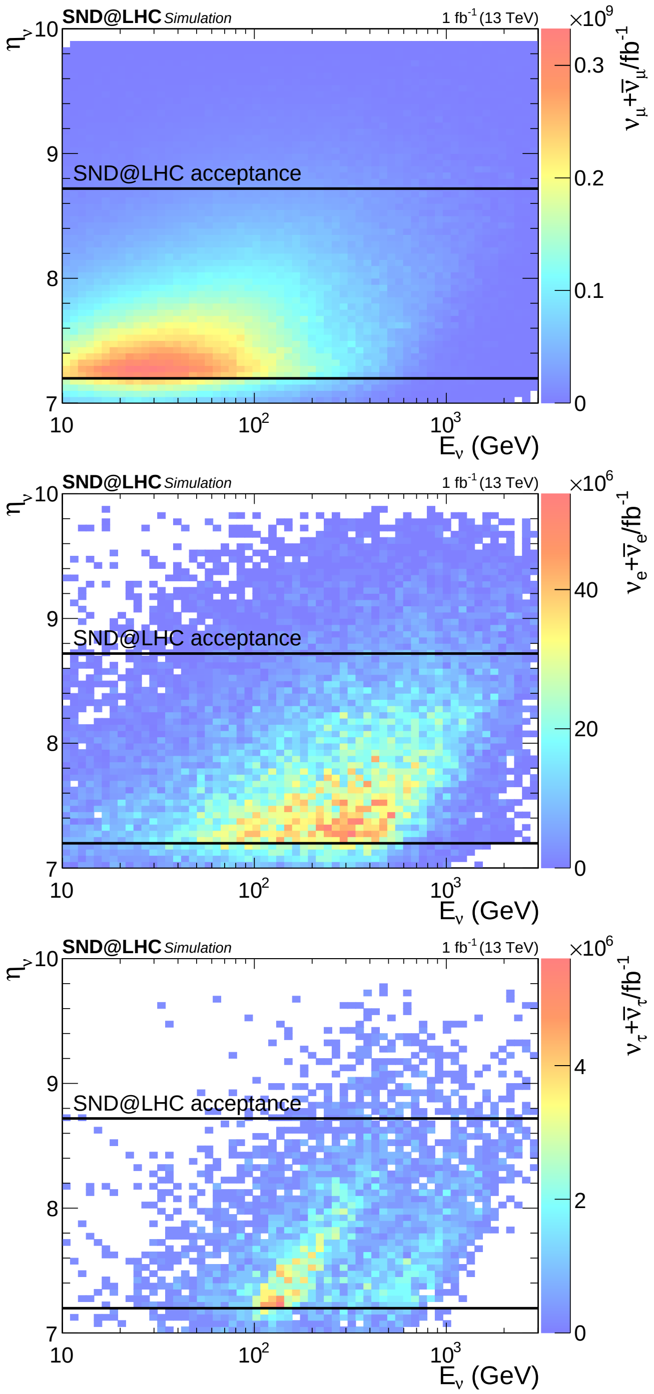

Figure 2: Neutrino and anti-neutrino flux as a function of ν energy E_ν and pseudo-rapidity η_ν for muon (top), electron (middle) and tau (bottom) neutrinos.

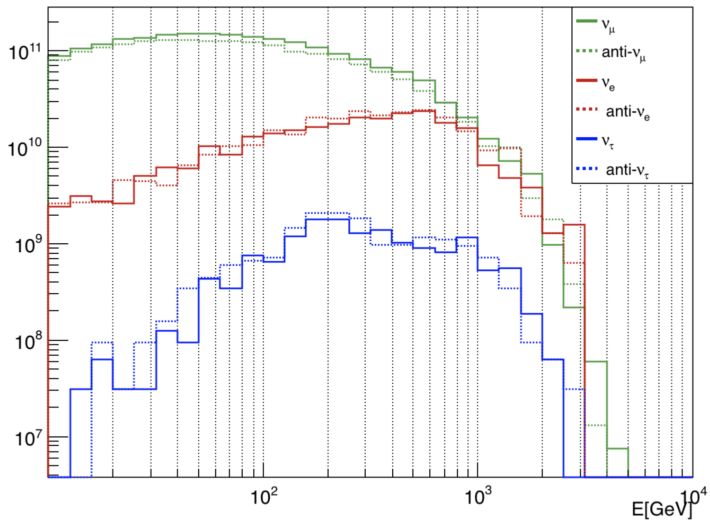

Figure 3: Energy spectrum of the different types of incoming neutrinos and anti-neutrinos as predicted by the DPMJET/FLUKA simulation. The normalisation corresponds to 150 fb^{-1}.

gluon parton distribution function in an unexplored x region, as explained in Section 13.

Lepton flavour universality test in ν interactions

In the pseudo-rapidity range of interest, tau neutrinos are essentially only produced in $D_s \to \tau\nu_\tau$ and the subsequent τ decays. According to the Pythia event generator, about 8% of ν_τs comes from beauty hadron decays. One can thus assume that the source of both ν_e and ν_τ is essentially provided by semi-leptonic and fully leptonic decays of charmed hadrons. Unlike ν_τs produced only in D_s decays, ν_es are produced in the decay of all charmed hadrons, essentially D^0, D, D_s and Λ_c. Therefore, the ν_e/ν_τ ratio depends only on the charm hadronisation fractions and decay branching ratios. The systematic uncertainties due to the charm-quark production mechanism cancel out, and the ratio becomes sensitive to the ν-nucleon interaction cross-section ratio of the two neutrino species. The measurement of this ratio can thus be considered a lepton flavour universality test in neutrino interactions. As it will be described in Section 13, the ν_e/ν_τ ratio can be written in terms of the known branching ratios convoluted with the charmed hadron species in the acceptance. The estimate of these “weighted” branching ratios is affected by a systematic uncertainty of about 22% while the statistical uncertainty is dominated by the low statistics of the ν_τ sample, which corresponds to a 30% accuracy.

SND@LHC plans to use also the ν_e/ν_μ ratio as a lepton flavour universality test in neutrino interactions. The situation is rather different for ν_μs when compared to ν_τs. The ν_μs are much more abundant but heavily contaminated by π and K decays, and therefore the production mechanism cannot be considered the same as in the case of ν_e. However, this contamination is mostly concentrating at low energies. Above 600 GeV, the contamination is predicted to be reduced to about 35%, and stable with the energy. Moreover, charmed hadron decays have practically equal branching ratios into electron and muon neutrinos. Therefore the ν_e/ν_μ ratio is not affected by the systematic uncertainties in the weighted branching fractions. The yield of muon neutrinos from π and K decays is affected by two systematic uncertainties, one due to the π and K production in this η range, and the other due to their propagation through the machine elements along the beamline. Both contributions can be assessed thanks to the available measurements used to constrain the simulation, as discussed in Section 13. As a result, the ν_e/ν_μ ratio provides a test of the lepton flavour universality with an uncertainty of 15%, with an equal 10% statistical and systematic contribution. It has to be noted that SND@LHC will measure the particle flux in TI18 with high accuracy and possibly also in other locations along the beamline, thus contributing to benchmark the tools for the propagation of particles to further reduce systematic uncertainties.

Measurement of the NC/CC ratio
At the high energies of the LHC neutrinos, deep-inelastic scattering is by far the dominating interaction mechanism. Thus, the scattering off nuclei can be well approximated as the incoherent sum over protons and neutrons. The neutrino flavour is identified in charged-current (CC) interactions through the identification of the corresponding charged lepton produced in the final state. The neutral-current (NC) process is flavour insensitive. By summing over neutrinos and anti-neutrinos, the ratio between NC and CC deep-inelastic interaction cross-sections at a given energy can be written as a simple function of the Weinberg angle, with a correction factor accounting for the non-isoscalarity of the target [30]. In the approximation that the differential ν and $\bar{\nu}$ fluxes, as a function of their energy, are equal, the same formula also applies to the observed interactions since the convolution with the flux would bring the same factor everywhere, that then cancels out in the ratio. Therefore, the measurement of this ratio can be turned into a measurement of the Weinberg angle.

SND@LHC plans to measure this ratio as an internal consistency test, as described in detail in Section 13, rather than as a measurement of the Weinberg angle, known with a precision of 1% [31, 32]. The propagation through the LHC machine elements introduces a source of asymmetry between neutrinos and anti-neutrinos. This is particularly true for muon neutrinos that mainly come from non-prompt decays (π and K). Nevertheless, the asymmetry between muon neutrinos and anti-neutrinos is estimated to be well below 20% in all energy bins, and it mostly concerns the low energy region where the neutrino interaction cross-section is lower. As a result, the systematic uncertainty on this ratio for the observed events is below 5%. Another source of systematic uncertainty comes from the unfolding of the instrumental effects, such as the muon identification and the subtraction of neutron-induced events that can mimic NC neutrino interactions, amounting to about 10%. Therefore, the overall systematic uncertainty is 10% while the statistical error is 5%, associated to the number of NC observed interactions.

2.2 Feebly Interacting Particles

One of the main challenges in particle physics today is determining the microscopic identity and the cosmological origin of dark matter (DM). The theoretical landscape is broad and spans many orders of magnitude in the mass/coupling parameter space. A compelling idea to be explored is DM as a thermal relic of the early universe. A much explored example of this scenario is the Weakly Interacting Massive Particle (WIMP), a particle in the GeV–TeV mass range interacting with the visible sector via interactions with couplings comparable to those of the weak interaction. Searches for WIMPs are in full swing [33, 34] and, more generally, there is currently an explosion of interest [35] in searches for Feebly Interacting Particles (FIPs). This interest is also stimulated by the lack of any discovery in various direct detection dark matter experiments, which have reached unprecedented levels of precision, as well as in collider experiments that have collected large data samples, which are being analysed with increasingly sophisticated techniques. The majority of these efforts are targeting masses from about 10 GeV to 1 TeV, leaving the lower mass range much less explored. Recently, a lot of attention has been directed towards light DM (LDM) in the keV–GeV mass range [36]. The scarce sensitivity at lower masses is related to the difficulty of detecting the corresponding very soft recoils, given the expected non-relativistic nature of galactic dark matter.

A pioneer in direct-detection light DM searches, the CRESST-III low-mass DM experiment [37] recently published its first result for masses below 1 GeV. These results show a sensitivity about ten orders of magnitude worse than the XENON1T results for masses above 10 GeV (see Figure 4 left). The SuperCDMS SNOLAB experiment has the potential to improve these constraints by about four orders of magnitude in the future [38], but its potential impact on the DM parameter space strongly depends on the DM nature and on other parameters, as discussed in Refs. [39, 40] (see Figure 4 right).

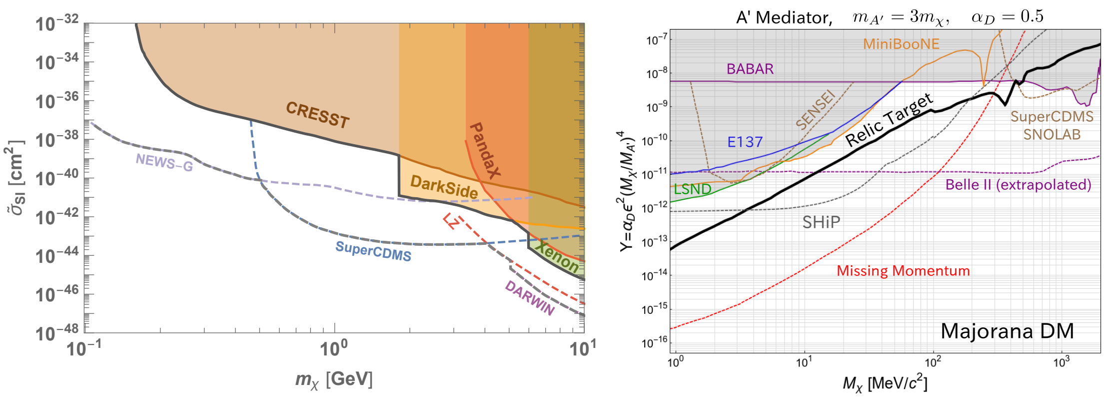

Figure 4: (Left) Current (solid lines) and expected (dashed lines) constraints on the DM-nucleon scattering cross section from direct detection experiments' [41]. (Right) Direct detection experiments results (solid lines) and projections (dashed lines) translated to the same parameter space as accelerator-based searches for Majorana DM particles [39, 40]. Here the parameter y characterizes both the DM abundance in the early Universe, and the DM-nucleon scattering cross-section. On the x-axis, m_χ is the DM mass. The DM particles χ are assumed to interact with the SM via a vector mediator A'. The "Missing momentum" curve refers to the ultimate projected performance of the LDMX experiment.

These developments have also stimulated significant theoretical efforts. Many models have been proposed that expand the interesting mass range to lower values (GeV and below), while still giving rise to the expected relic DM abundance. More generally, these efforts have led to developments of models of a generic "dark sector", which communicates with the SM particles through a variety of feebly coupled mediators (see e.g. Refs. [30, 35]). These concepts also include feebly coupled particles arising in other beyond SM extensions.

Since current cosmic direct-detection experiments, searching for elastic nuclear recoils, rapidly lose sensitivity to particles with masses below a few GeV [33, 42], accelerator-based experiments at the intensity frontier represent an alternative and appealing route in this quest [36]. In a fixed-target experiment at an accelerator, the candidate dark matter particle is ultra-relativistic and therefore the experimental challenges in its detection are different and less demanding than for experiments searching for dark matter originating in the galaxy. For instance, neutrino oscillation experiments could efficiently search for LDM via signatures of DM scattering with electrons and/or nuclei in their near detectors [43, 44, 45, 46, 47, 48, 49, 50, 51, 52, 53, 54]. More importantly, collisions delivered by accelerators offer a general source of feebly coupled particles. This motivates experiments such as the beam-dump experiment SHiP, which is equipped with a detector for neutrino scattering and a detector to search for decays of FIPs. SHiP has reported substantial sensitivity to light dark matter by using the recoil technique with the neutrino target [55].

SND@LHC is a fixed target neutrino experiment that will also be capable of exploring models with FIPs, including the interpretation of DM scattering. In Section 13 we report the sensitivity of SND@LHC to two different channels: scattering off electrons and scattering off nucleons. While the sensitivity to the benchmark model of a dark photon coupled to light DM through scattering off electrons is not competitive with the missing-energy technique, the direct search still provides an independent and complementary result. The search via the scattering off nucleons provides the world-leading sensitivity to the process in a wide region of the parameter space.

2.3 Detector concept

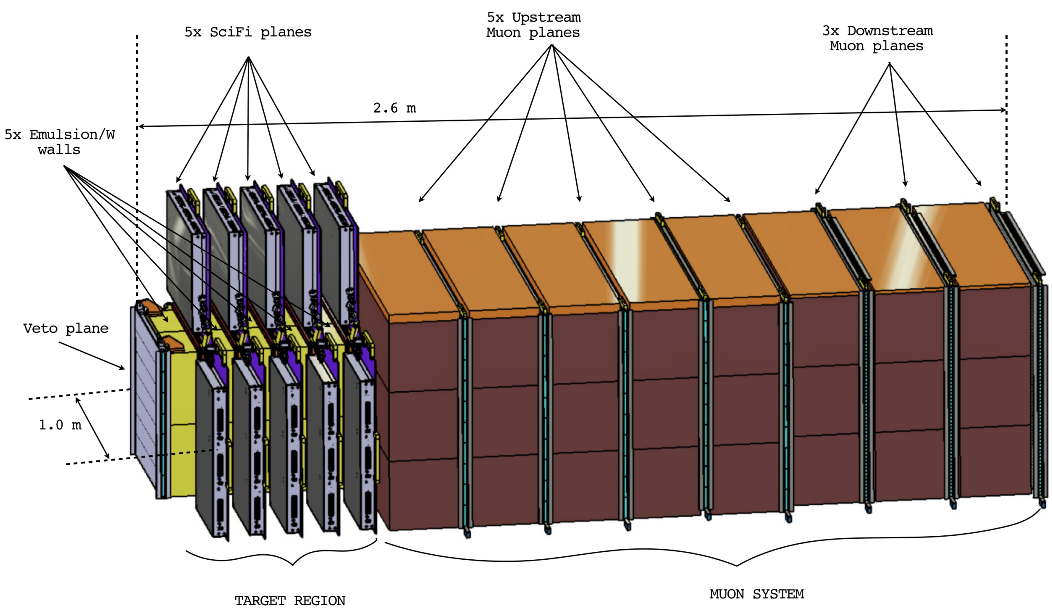

Figure 5: Layout of the proposed SND@LHC detector.

The detector concept was developed to fulfill the challenging task of identifying all three neutrino flavours with high efficiency and of searching for FIPs directly through their scattering off atoms in the neutrino target. This requires three detector elements: a vertex detector with enough resolution to disentangle the neutrino-interaction vertex from the one of the tau-lepton decay; a calorimeter to measure both the electromagnetic and hadronic energy with a good time resolution; a muon system to identify the muon produced in ν_μ CC interactions and in the muonic decay of the tau lepton. The geometrical constraints that will be discussed in

Section 3 prevent adding a magnetised volume that would allow to separate neutrinos from anti-neutrinos.

A good solution for such an apparatus, as demonstrated by the OPERA experiment [56], is a hybrid detector that combines nuclear emulsion technology and electronic detectors. A schematic drawing of the proposed detector to be installed in the TI18 tunnel is shown in Figure 5. The apparatus is made of a target region followed downstream by a muon system. Upstream of the target region two planes of scintillator bars act as a veto for charged particles, mostly muons coming from the ATLAS interaction point. The target region, with a target mass of about 800 kg, is instrumented with five walls of emulsion cloud chambers (ECC), each followed by a Scintillating Fibre (SciFi) plane. The ECC technology alternates emulsion films, acting as tracking devices with micrometric accuracy, with passive material acting as the neutrino target. Tungsten is used as a passive material to maximize the mass within the available volume. The muon identification system is located downstream of the target. It will consist of eight iron slabs, each followed by a plane of scintillating bars. Figure 5 also displays the electronics of the SciFi detector in the target region.

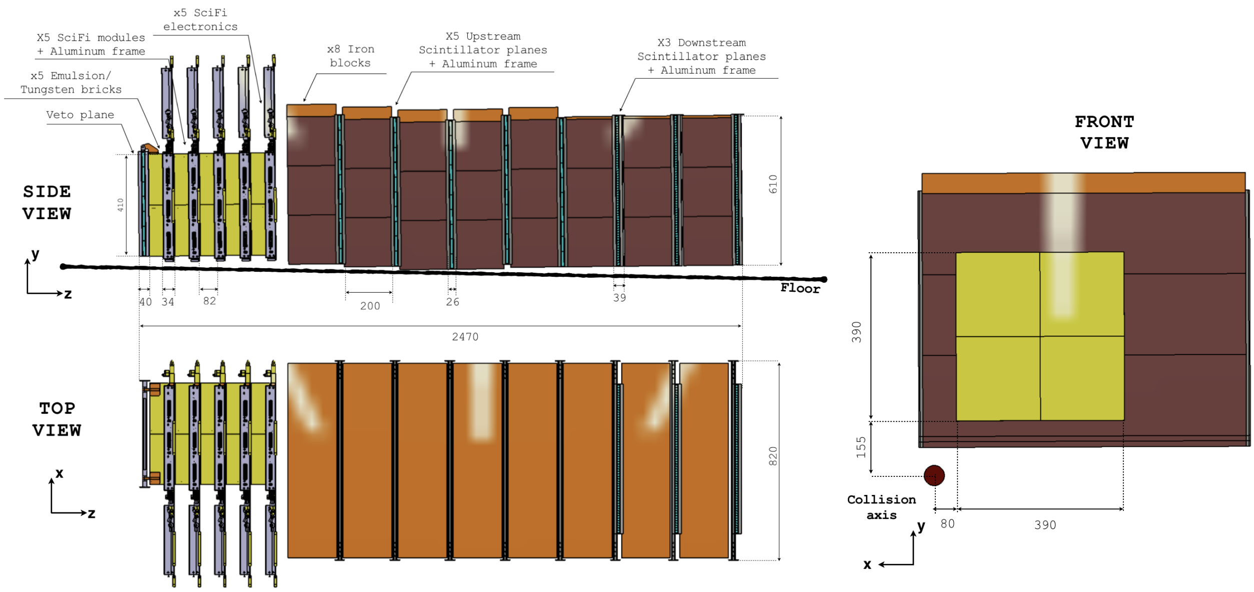

Figure 6: (Left) Schematic drawing of the detector as seen from the top and side views. (Right) The front view is reported with the nominal collision axis.

The emulsion detector, designed according to the ECC technology, acts as a vertex detector with micrometric resolution, measuring the trajectory of all the charged particles produced in a neutrino interaction, including the short-lived charmed hadrons and tau leptons. The target has a hybrid structure, being made of a sequence of 7.8 cm thick emulsion/tungsten walls interleaved with high-precision tracker stations made of planes of SciFi fibres with a diameter of 250 µm. The SciFi detector will predict the location of the neutrino interactions in the emulsion brick, will provide the time stamp to the events reconstructed in the emulsion and will complement the emulsion chamber for the calorimetric measurement of electromagnetic showers. An electron produced at the primary vertex will see on average about $40\,X_0$ in the target. Such a fine sampling of the target region (every 0.6 interaction lengths - λ_{int}) provides high performance in the event matching between emulsion and electronic detectors, being independent of the hadronic shower development, and in the calorimetric measurement of electromagnetic and hadronic showers.

The muon detector will consist of eight iron walls, for a total of $8\,\lambda_{\rm int}$, interleaved with the same number of planes made of scintillator bars. In the five most upstream planes, one layer of horizontal bars is used. In the three most downstream planes, the granularity of the bars is increased and a layer with vertical bars is added, in order to improve the efficiency of the isolation criteria for the identification of muons originating in neutrino interactions. Moreover, the combination of SciFi and scintillating bars of the muon detector will also act as a non-homogeneous hadronic calorimeter with on average $9.5\,\lambda_{\rm int}$, ranging from 8 to $11\,\lambda_{\rm int}$ depending on the position of the neutrino interaction vertex in the target, for the measurement of the energy of the hadronic jet produced in the neutrino interaction and hence for the neutrino energy measurement. The energy resolution will be particularly good for electron neutrinos where both the lepton and the hadronic jet will be directly measured.

The schematic drawing of the detector as seen from the side and top views is shown in the left part of Figure 6. Notice that the floor is inclined, as it can be seen in the side view. The right part of Figure 6 shows the front view where also the nominal collision axis is reported. The target region is highlighted in yellow and its position corresponds to the pseudo-rapidity region $7.2 < \eta < 8.6$.

The identification of the neutrino flavour is done in charged current interactions by identifying the charged lepton produced at the primary vertex. Electrons will be clearly separated from π^0's thanks to the micrometric accuracy, which will enable photon conversions downstream of the neutrino interaction vertex to be identified. The left panel of Figure 7 shows a ν_e interaction in the OPERA emulsion cloud chamber. The electron produced at the primary vertex is clearly separated from the electromagnetic shower induced by the two photons produced by the π^0 decay. Muons will be identified by the electronic detectors as the most penetrating particle, beyond the hadronic shower. Tau leptons will be identified topologically in the emulsion, through the observation of the tau decay vertex, together with the absence of any electron or muon at the primary vertex, according to the technology developed by OPERA [57, 19]. The right panel of Figure 7 shows a ν_τ candidate detected in OPERA [58]. SND@LHC will have the same granularity as in OPERA, alternating emulsion films with 1 mm thick passive material. This is motivated by the need to keep high tracking and vertexing performance in an environment with a high density of tracks, rather than by the τ flight length which is a few cm long at the LHC energies. Figure 8 shows the first OPERA tau neutrino candidate [57] where the decay channel $\tau \to \rho\nu_\tau$ with subsequent $\rho \to \pi^0\pi$ decay was identified.

The planes of scintillator bars will have a timing resolution better than 100 ps for the time-of-flight measurements of particles from the ATLAS interaction point. The resolution in the time-of-flight measurement will thus be determined by the 200 ps temporal spread that is defined by length of the luminous region at IP1. The timing resolution is important for any possible discovery of FIPs. FIPs will be identified through their scattering off atoms of the emulsion target material. In the case of a FIP elastic scattering off atomic electrons, the experimental signature consists of an isolated recoil electron that can be identified through the development of an electromagnetic shower in the target region. For FIPs interacting elastically with a proton, instead, an isolated proton will produce an hadronic shower in the detector. In both cases the background can be reduced down to a negligible level by topological and kinematical selections, as it will be discussed in Section 13. The timing information will be used to confirm any possible excess of events with the expected signature.

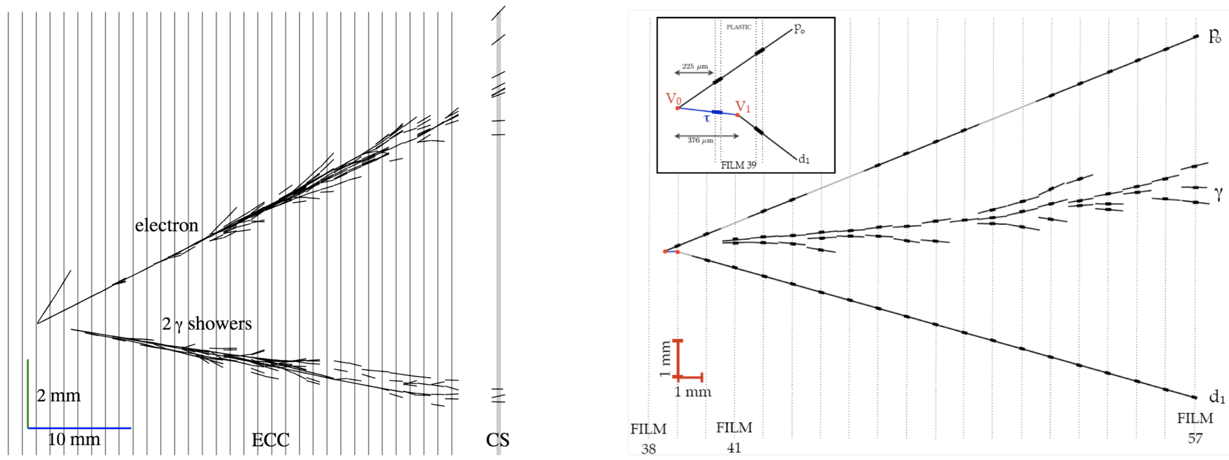

Figure 7: Display of reconstructed tracks in the OPERA emulsion detector for a ν_e (left) [59] and a ν_τ (right) [58] candidate event.

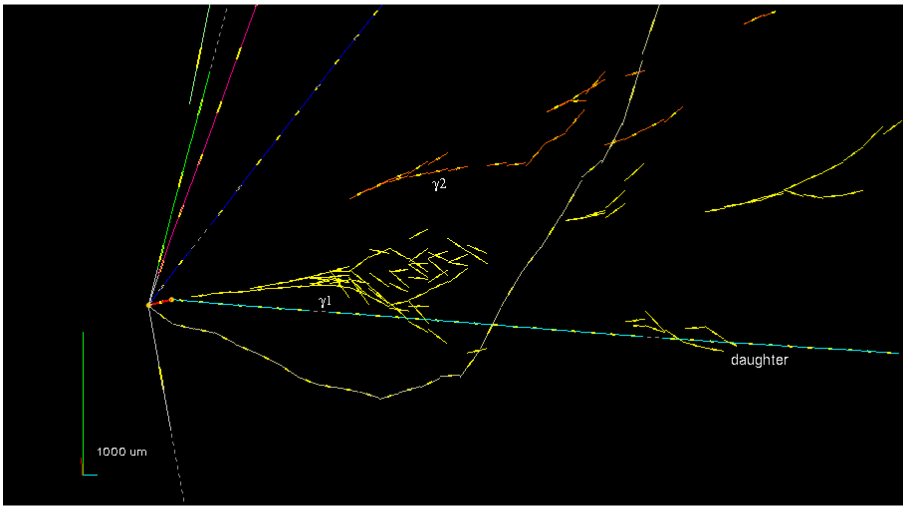

Figure 8: Display of the full reconstruction of the first tau-neutrino candidate detected by the OPERA Collaboration [57]. The tau-lepton track is displayed in red.

3 Detector environment

In this section we report on the environmental conditions expected in the TI18 tunnel that affect the design and operation of the detector. In particular, in the first subsection we describe the geometrical constraints of the tunnel, affecting the detector size and positioning, while in the subsequent subsections we report the expected flux of all particles except neutrinos, i.e. the possible background sources.

3.1 Detector geometry constraints

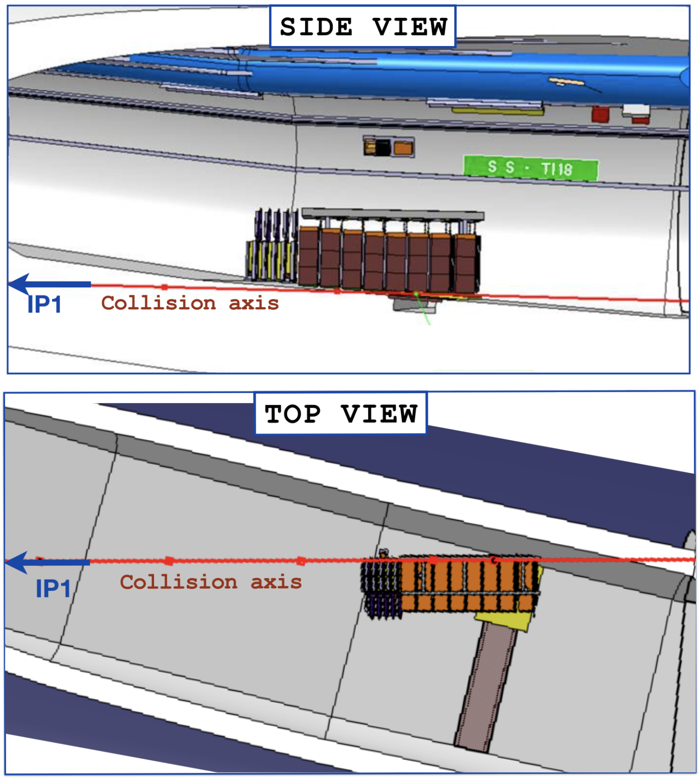

Figure 9: Side and top views of the detector in the TI18 tunnel.

The SND@LHC detector takes full advantage of the space available in the TI18 tunnel to cover the desired range in pseudo-rapidity. Figure 9 shows the side and top views of the detector positioned inside the tunnel. It is worth noting that the tunnel floor is sloped, as can be seen from the side view, with the floor sloping down along the length of the detector. As shown in the top view, the nominal collision axis from IP1 comes out of the floor very close to the wall of the tunnel. The location is ideal to explore the off-axis region. Under the assumption that no civil engineering work can be done in time for the operation in Run 3, the tunnel geometry imposes several constraints. The following guidelines have been adopted for the optimisation of the detector design: a good calorimetric measurement of the energy requires about 10 λ_{int}; a good muon identification efficiency requires enough material to absorb hadrons; for a given transverse size of the target region, the azimuthal angular acceptance decreases with distance from the beam axis. The energy measurement and the muon identification set a constraint on the minimum length of the detector. With the constraints from the tunnel, this requirement competes with the azimuthal angular acceptance that determines the overall flux intercepted and therefore the total number of observed interactions. The combination of position and size of the proposed detector is an optimal compromise between these competing requirements. The geometrical constraints also restrict the detector to the first quadrant only around the nominal collision axis, as shown in Figure 9.

The result is a compact detector, 2.6 m in length. The energy measurement and the muon identification limit the target region to a length of about 80 cm. The transverse size downstream of about $80(\mathrm{H}) \times 60(\mathrm{V})\ \mathrm{cm}^2$ is limited by the constraint of the tunnel side wall. The transverse size of the target region is proportionally smaller in order to match the acceptance of the energy measurement and the muon identification for the vertices identified in the target volume. In order to maximise the number of neutrino interactions, tungsten has been selected as the passive material.

3.1.1 Proton-beam crossing angle

The bottom left corner of the neutrino target region is positioned 155 mm above the nominal IP1 collision axis, and 80 mm to the side, as shown in the right panel of Figure 6. The proton beams cross vertically in IP1 with a half-angle of about 150 microradians, either upwards or downwards. It is foreseen that about half of the luminosity is delivered in either configuration. When upwards, the collision axis in TI18 is 72 mm above the nominal level. During the LHC fills, the angles change from 160 down to 120 microradians, corresponding to 76.8 mm and 57.6 mm respectively. Inversion from upwards to downwards of the beam crossing in IP1 displaces the beam by the same amounts in the opposite direction. The detector acceptance in the horizontal direction is the same in either configuration. Overall, the number of observed neutrino interactions differs, with respect to the nominal acceptance calculated with no crossing angle, by +18% when beams cross upwards, and by −22% when beams cross downwards, and the SND@LHC coverage in η shifts from $7.3 < \eta < 9.0$ to $7.1 < \eta < 8.3$, respectively.

3.2 Backgrounds in TI18

The LHC simulation package developed by the CERN EN-STI team [60, 61] using FLUKA [62, 63] describes the transport of proton beams along the LHC in great detail. The predictions regarding machine induced backgrounds are confirmed by experimental measurements [64, 27]. The package embeds the DPMJET event generator [65, 66], which emulates proton-proton minimum bias events, including charm production.

Particle fluxes in TI18 were already investigated during the preparation of the FASER Technical Proposal [28], using both simulations and measurements performed in situ during LHC Run 2. The analysis was refined in a successive paper [3]. The detecting equipment consisted of an emulsion-tungsten package positioned on the collision axis, and CERN radiation monitors [67], which, placed in various locations in the tunnel, measures low energy charged hadrons and thermal neutrons. The EN-STI team performed simulations of proton-proton interactions at 13 TeV, in which charged pions and kaons from IP1 were transported along the LHC straight section until decay. The simulations included beam loss effects, beam gas interactions and interactions of secondaries. The expectation was that the particle flux in TI18 be essentially composed of muons and neutrinos from the IP, plus a negligible amount of low energy charged and neutral hadrons. This was confirmed by the measurements. The track angular distribution in the emulsion bricks mainly pointed to the IP. With respect to particles coming from the IP, the FASER measurement counted 1.2–1.9 $\times$ 10^4 particles /cm^2/fb^{-1}, in excellent agreement with the expected muon flux from the LHC simulation estimated to be 2×10^4 /cm^2/fb^{-1}.

3.2.1 Muon flux

Since the study done for FASER, the EN-STI team has been increasing the DPMJET/FLUKA event sample by up to about a factor of ten. This allows studying particle fluxes in TI18 in more detail, in particular in the SND@LHC acceptance. Positions and momenta of muons are recorded on a virtual scoring plane with an area of 1×1 m^2, and located 75 m upstream of the TI18 tunnel, in order to decouple the muon interactions in rock and concrete from the primary flux of muons produced at the IP and within the detector and LHC machine elements. Figure 10 shows the spectra of the muons that are travelling in the direction of the SND@LHC acceptance, at the scoring plane. When tracked through the rock to the SND@LHC, muons with E<30 GeV do not reach the detector. The negative muon distribution shows an excess, peaking at about 1.5 TeV. A study of the directions of those muons shows that they originate from the IP. Figure 11 shows muon rates at the SND@LHC location. The integrated rate in the SND@LHC acceptance is estimated to be about 350 Hz, equivalent to about $2{\times}10^4$ /cm^2/fb^{-1}. This value accounts for the effect of multiple scattering in the rock upstream of the detector.

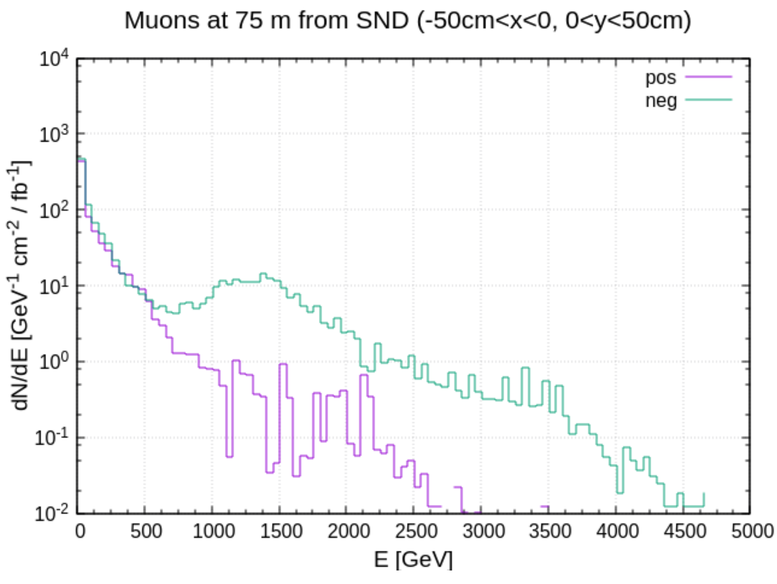

Figure 10: Muon flux in the SND@LHC acceptance as a function of the energy as predicted with the DPMJET/FLUKA simulation of CERN EN-STI. Muon positions and momenta are recorded at a 1×1 m^2 scoring plane, located 75 m upstream of TI18, and tracked to the SND@LHC.

3.2.2 Neutrons and K_Ls from muon DIS

Isolated neutrons and also K_L particles can be generated by deep inelastic scattering of muons from IP1 in the rock upstream of the SND@LHC detector. If these neutrons interact in the detector, they can mimic neutrino neutral current interactions. Only the last few meters of rock are relevant, since the hadrons get otherwise absorbed: 5 meters have been conservatively

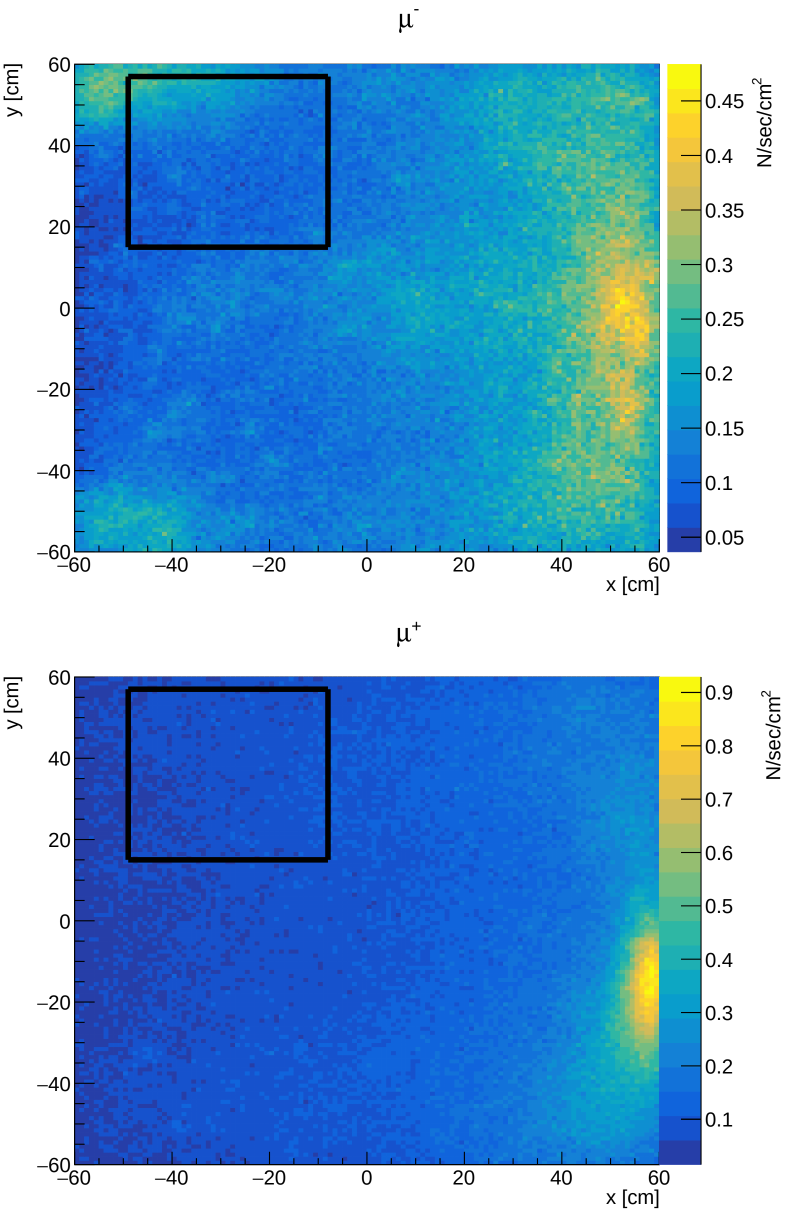

Figure 11: Muon rates at the SND@LHC location as predicted with the DPMJET/FLUKA simulation of CERN EN-STI. The contour of the SND@LHC acceptance is outlined.

assumed. A study was performed using the sample of DPMJET/FLUKA muons recorded 75 m upstream of the SND@LHC, described in Section 3.2.1. The muon deep-inelastic interaction was simulated with Pythia6 event generator. The expected flux of n, $\bar{n}$ and K_Ls in the SND@LHC acceptance for different energy thresholds is shown in Table 1. Events with accompanying charged particles that would fire the veto layer in front of the SND@LHC are rejected, thus defining the "isolated" particles of Table 1. Although a very low flux is predicted, we plan for a follow-up study with the tunnel geometry included in a GEANT4 full simulation to better describe their flux and interactions inside the detector.

particles/fb^{-1}	E>10 GeV	E>100 GeV	E>200 GeV	E>500 GeV
K_L	48	11.7	4.4	0.5
neutron	17	5.4	2.0	0.5
anti-neutron	12	3.3	1.5	0.1

Table 1: Flux of isolated n, $\bar{n}$ and K_Ls entering the target surface, produced by muon DIS in the rock upstream of the SND@LHC detector.

3.2.3 Thermal neutrons

The DPMJET/FLUKA package by the CERN EN-STI team is also used for estimating the low energy neutron flux. Both beams contribute but the flux observed in TI18 is predominantly produced by beam 2 that passes by TI18 while moving towards IP1. Neutrons are generated in the interactions of the protons with the residual gas inside the LHC vacuum pipe. The predicted spectrum is shown in Figure 12. It consists of about 50% of thermal neutrons at $\sim$0.025 eV. The integrated flux amounts to 2.8×10^8 /cm^2/year, of which 4% has an energy larger than 1 MeV and 1.3% is over 20 MeV. This is in good agreement with the radiation monitor measurements of a few 10^6 /cm^2/fb^{-1}. This allows using non-radiation-hard electronic devices. For nuclear emulsion it was observed in [27] that they blackened when exposed to about 10^8 neutrons/cm^2 as a result of neutron capture in Ag-109 silver nuclei. However keeping diffuse hits at the lowest possible level facilitates track reconstruction. The emulsion detector can be protected with a 3–4 cm layer of borated polyethylene (5% B_2O_3) to provide an attenuation factor of 10^{-7}. Alternatively, a similar attenuation can be achieved with a thinner layer of a boron-carbide compound, providing an attenuation of a factor of 12 every 2 mm. Simulations are under way to understand if the concrete of the floor, underneath the SND@LHC, provides sufficient shielding, or whether it must be further improved.

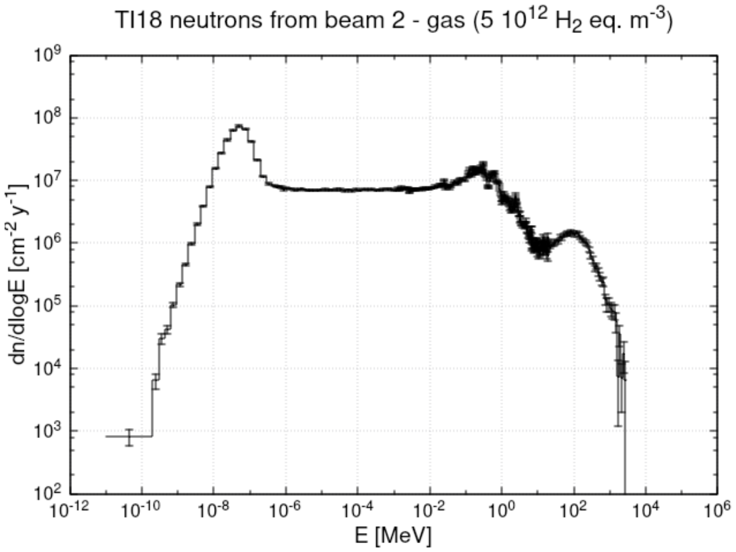

Figure 12: Spectrum of neutrons induced by beam 2 in the volume of the TI18 tunnel, as predicted with the DPMJET/FLUKA simulation of CERN EN-STI. This plot is generated with the expected number of protons circulating during a year of a High Luminosity run.

4 Veto system

4.1 Overview

The Upstream Veto Detector will act as a veto for charged particles and will be located upstream of the emulsion/SciFi detector. The baseline technology for the Upstream Veto Detector is EJ200 scintillating bars read out by silicon photomultipliers (SiPM). It comprises two parallel planes of stacked bars, each bar with dimensions $42 \times 6 \times 1\,\mathrm{cm}^3$ and read out on both ends by eight Hamamatsu S14160-6050HS SiPMs. Each SiPM is placed on a PCB common to each side of a detector plane and subsequently readout by TOFPET2 ASICS. The bars will be wrapped in aluminum foil to ensure opacity and isolate them from light coming from adjacent bars. The wrapping will create a small inefficiency in the region between bars. The duplication of the detector planes, shifted 1 cm vertically with respect to each other, ensures full coverage of the active target region. The veto system, with the two planes and PCB readout is illustrated on the left of Figure 13.

4.2 Mechanics

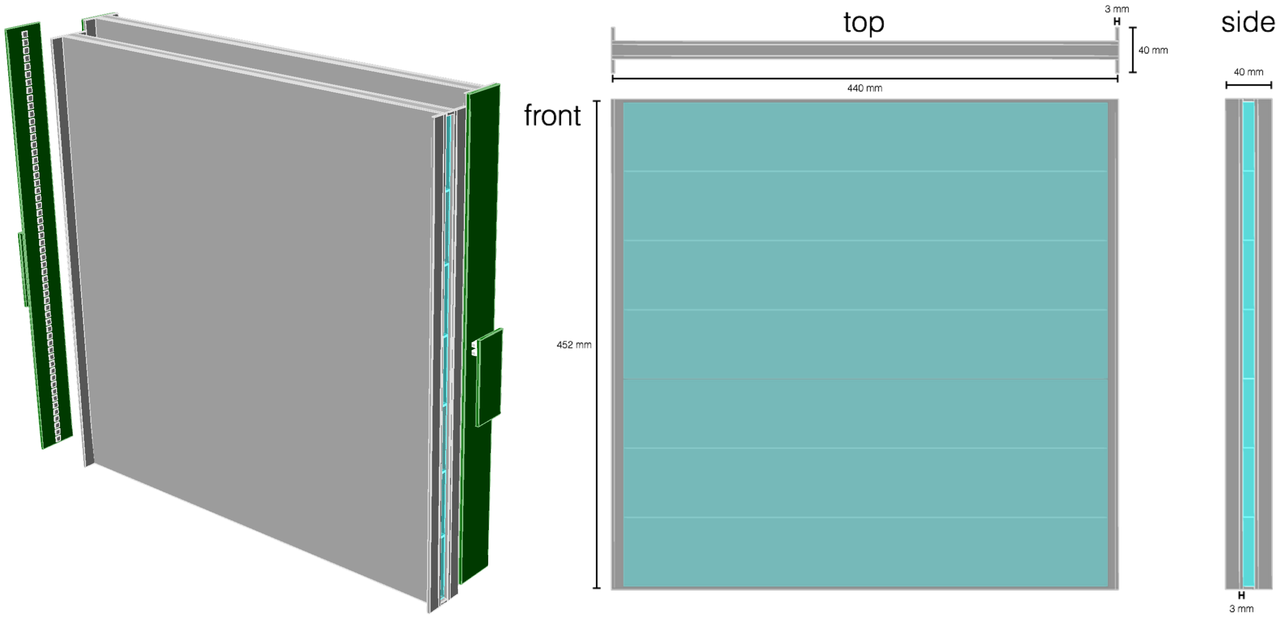

Figure 13: (Left) A view of the veto system illustrating the placement of the SiPMs and PCB end caps and (Right) the schematics of the mechanical frame with the bars overlaid.

The stacked scintillating bars for each plane are housed in an aluminum frame as seen in Figure 13. The thickness of the wall is 3 mm. The sides are flared out to allow for the width of the FE board. The PCB on each side also acts as an end cap for the aluminum frame, which is constrained to be at least as wide as the FE board (32 mm) plus some tolerance.

4.3 Readout and powering

56 SiPMs will be mounted on a PCB end cap, one for each side, totaling 224 SiPMs for the whole system. The individual signals for each SiPM are sent to the FE board, containing two

TOFPET2 ASICS. A DAQ motherboard collects the digitized signals from the four FE boards and also provides bias to the SiPMs. A NIM crate, which is shared with the muon system, will house LV and HV CAEN power supplies. Details of the DAQ system are described in Section 8.

4.4 Calibration

The timing calibration of the veto plane will be performed on the surface before installation. For a given plane, cosmic muons traversing the plane vertically will be used to calibrate the time between bars while the two planes will be calibrated by looking at muons traversing both planes, as seen in Figure 14. Assuming that one cosmic muon per minute per cm^2 reach the surface, this corresponds to about 40 muons per minute hitting the detector for the former configuration and about 1700 per minute for the latter configuration. Background muons from the beam will be used to perform the calibration of the veto system with the target tracker and muon system.

To ensure proper background rejection, the veto system requires an efficiency as close as possible to 100%. The efficiency to detect charged particles in the scintillator is assumed to be near 100% and this will be tested using cosmic muons on single bars before installation of the veto system.

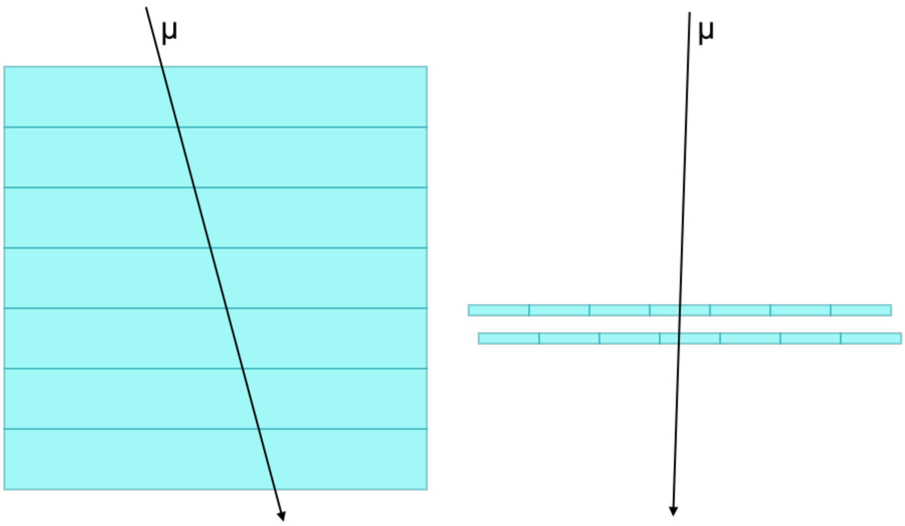

Figure 14: The two different configurations for the timing calibration using cosmic muons.

4.5 Cost and schedule

The estimated cost for the veto system is presented in Table 2. The cost of spare bars, SiPMs and DAQ boards is also included. The values for the DAQ boards and power supplies are effective costs. They are included in the cost of the whole DAQ system, described in Section 8.7.

A schedule is presented in Figure 15. Construction of the mechanical frame will begin in January 2021 in parallel to the development of the PCB end cap. The scintillating bars will arrive in March and followed by the SiPMs in March or April, with the wrapping of bars and mounting of SiPMs commencing after arrival from the manufacturer. Once the frame, bars and end caps are in place, commissioning and integration of the DAQ system can begin. Calibration

	Unit cost [CHF]	Units	Cost [kCHF]
Detector			
Bars	135	16	2.2
SiPMs	25	260	6.5
		Total	8.7
*DAQ Boards**			
PCB, components, assembly	1'189	1	1.2
Enclustra FPGA module	357	1	0.4
TOFPET2 ASIC	352	8	2.8
FE board	100	4	0.4
FE cables	59	1	0.1
		Total	4.8
*Power Supplies**			
CAEN LV module	638	1	0.6
CAEN HV module	1'375	1	1.4
CAEN crate	1'286	1	1.3
		Total	3.3
Mechanics			
Mechanical structure	500	2	1.0
PCB end-cap	100	4	0.4
Transport to CERN	100	2	0.2
		Total	1.6
Grand total			18.4

Table 2: Cost estimates for the different components of the veto system. *These are effective costs for the whole system. They are included in the cost estimates of the DAQ system.

on the surface will follow before installation at the beginning of November. The remaining time before the start of Run 3 will be used for further calibration and integration with the rest of experiment.

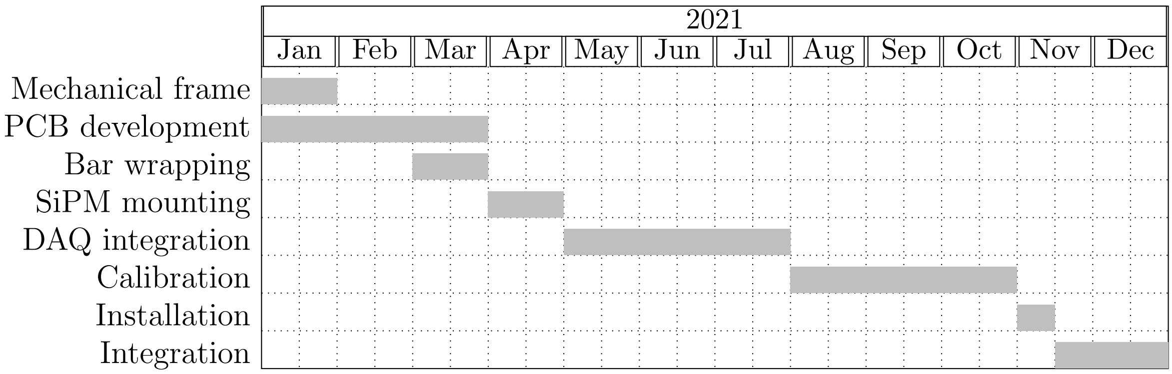

Figure 15: Schedule for construction and installation of the veto system.

5 Target and vertex detector

5.1 Overview

The emulsion target is made of five emulsion brick walls. Each wall has a transverse size of about $390 \times 390\,\mathrm{mm}^2$, consisting of four unitary cells, called *bricks*, built according to the Emulsion Cloud Chamber (ECC) technique, as illustrated in Figure 16.

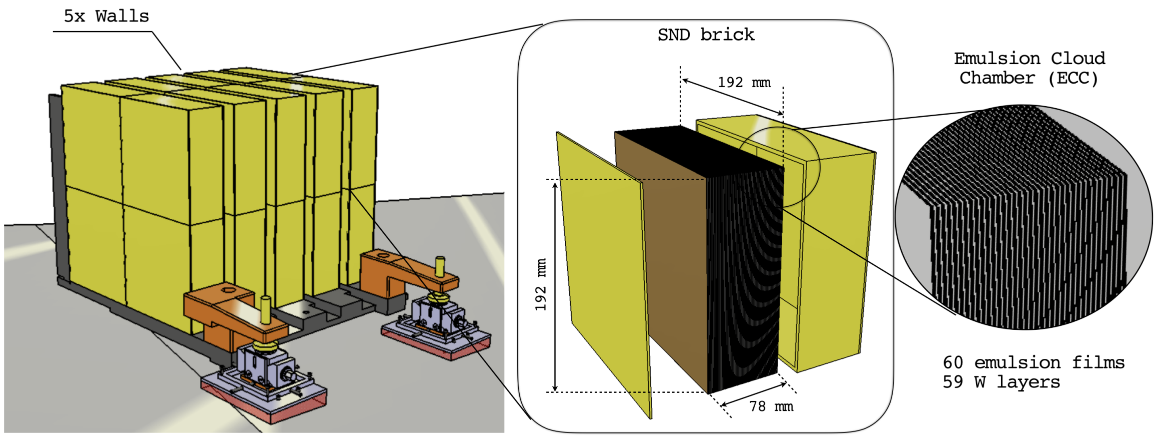

Figure 16: Layout of the emulsion target, consisting of five walls. Each wall is made by four bricks.

Each brick is made of 60 emulsion films with a transverse size of $192 \times 192\,\mathrm{mm}^2$, interleaved with 59 1 mm-thick tungsten layers. The resulting brick has a total thickness of $\sim 78\,\mathrm{mm}$, corresponding to $\sim 17\,X_0$, and a total weight of $\sim 41.5\,\mathrm{kg}$. The overall target weight with five walls of 2×2 bricks amounts to 830 kg.

The layout of the target structure was optimised with respect the Letter of Intent, where a single brick with a $400 \times 400\,\mathrm{mm}^2$ surface was proposed. Such large emulsion films have never been produced so far and their use in SND@LHC would have required dedicated R&D and quality assessment phases before going to large scale production. The Collaboration has therefore opted for the use of emulsions with a $192 \times 192\,\mathrm{mm}^2$ surface, that is a trade-off between conflicting requirements: overall dimensions that maximise the coverage of the SciFi sensitive area, large emulsion surface to maximise the event containment in the brick, reduced number of bricks per wall to minimise the dead area between adjacent cells and a well assessed emulsion production chain.

The ECC technology makes use of nuclear emulsion films interleaved with passive layers to build up a tracking device with sub-micrometric position and milliradian angular resolution, as demonstrated by the OPERA experiment [56]. It is capable of detecting τ leptons [19] and charmed hadrons [68] by disentangling their production and decay vertices. It is also suited for FIP detection through the direct observation of their scattering off electrons or nucleons in the passive plates. The high spatial resolution of nuclear emulsion films allows for identifying electrons by observing electromagnetic showers in the brick [20].

5.2 Target walls

5.2.1 Emulsion films

Nuclear emulsion films are the most compact, thinnest and lightest three dimensional tracking detectors with sub-micrometric position and milliradian angular resolution.

Nuclear emulsions consist of AgBr crystals scattered in a gelatin binder. The AgBr crystals, with a diameter of 0.2 µm, are sensitive to minimum ionizing particles (MIP). The trajectory of a MIP is recorded by a series of sensitised AgBr crystals along its path acting as latent image centres. A chemical process, known as development, enhances latent images inducing the growth of silver clusters (grains) with a diameter of 0.6 µm, visible by an optical microscope.

A nuclear emulsion film has two sensitive layers (70 µm-thick) on both sides of a transparent plastic base (170 µm-thick). By connecting the two hits left by a charged particle on both sides of the base, the slope of the track can be measured with milliradian accuracy. Figure 17 shows the cross-sectional view of an emulsion film and the image of an interaction vertex occurring in the plastic base, as seen at the optical microscope.

Nuclear emulsion films used in SND@LHC will have a transverse size of $192 \times 192\,\mathrm{mm}^2$. The whole detector will contain 1200 emulsion films, for a total of $44\,\mathrm{m}^2$. Emulsion films will be produced by Nagoya University in Japan and by the Slavich Company in Russia. For the long-term stability of the emulsion films, the temperature of the target will be kept at 15°C.

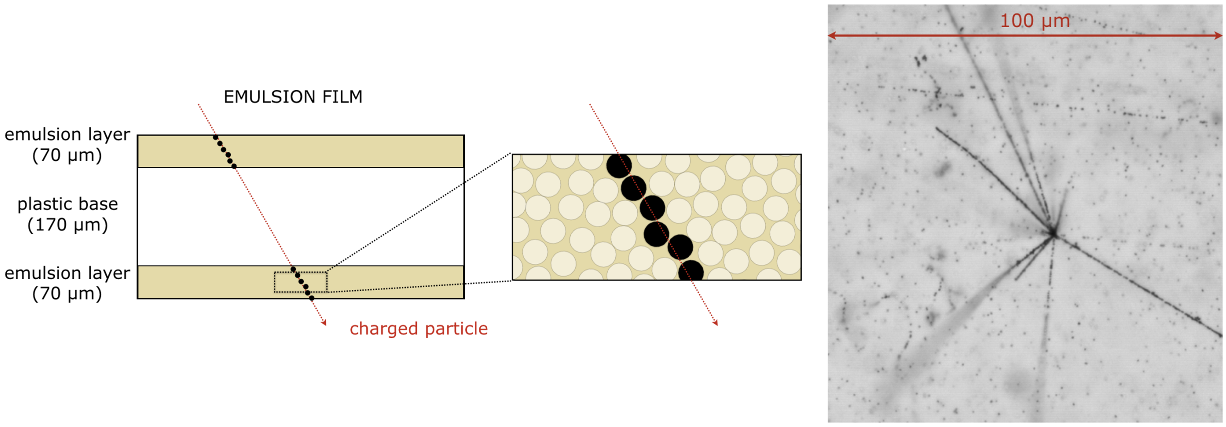

Figure 17: (Left) Structure of a nuclear emulsion film. The red dashed arrow shows the trajectory of a charged particle. After the photographic development process, silver grains are aligned along the trajectory of the charged particle. (Right) Microscope view of an emulsion film. Some nuclear fragments are emitted from the interaction vertex.

5.2.2 Tungsten target

Tungsten was selected as target material in order to maximise the interaction rate per unit volume. Moreover, its small radiation length ($\sim 3.5\,\mathrm{mm}$) allows good performances in the electromagnetic shower reconstruction in the ECC. The low intrinsic radioactivity makes tungsten a suitable material for an emulsion detector. Tungsten plates will have a transverse size of $192 \times 192\,\mathrm{mm}^2$, the whole detector will contain 1180 passive layers.

Two companies have been identified as providers of tungsten plates satisfying the SND@LHC requirements. Table 3 reports the specifications provided by both companies. The main difference between the two specifications is the density, since the second provider deals with pure tungsten while the other one uses an alloy with 95% W. The total target mass is 780 kg and 830 kg for tungsten I and II, respectively. The planarity is less precise from the second provider but might be tolerated. A batch of tungsten plates from each provider was ordered and is expected to be delivered at CERN at the end of January 2021. The plates will undergo a quality check campaign before the final choice is made.

Tungsten plates	type I	type II
Chemical composition	W 95%, Ni 3%, Cu 2%	W 100%
Density	17.8 – 18 g/cm^3	19.2 g/cm^3
Thickness	0.975$\pm$ 0.025	1.000$\pm$ 0.025
Roughness	0.8 μ (Ra)	0.8 μ (Ra)
Planarity	0.025 mm	0.050 mm
Target mass	780 kg	830 kg

Table 3: Specifications of tungsten plates provided by two different companies. The total mass of the SND@LHC target is also reported.

The chemical compatibility with emulsion films was tested on a timescale of one month for tungsten I. Additional tests are in progress with material provided by both companies.

5.2.3 Target assembly

The target assembly will be performed in the dark room at CERN (building 169).

The different assembly phases are sketched in Figure 18[1]. An aluminum box will host four bricks, that will be produced one after the other by piling up 60 emulsion films and 59 tungsten layers (a, b, c, d). The box is then closed (e) using a semi-automatic tool that keeps the necessary pressure to avoid any relative displacement between emulsion films. Once closed, the box will guarantee light-tightness. Each wall will be transported from the dark room to the TI18 tunnel separately by means of a dedicated trolley (f) and, once there, inserted into the mechanical structure of SND@LHC.

5.2.4 Exchange of emulsion films

Given the expected muon rate of 2×10^4 /cm^2/fb^{-1}, we plan to exchange the emulsion target every 25 fb^{-1}. Under the assumption of integrating 150 fb^{-1} in the whole LHC Run 3, we plan to install six sets of emulsion/tungsten bricks in total. The exchange of target walls will be performed during LHC Technical Stops. Since it is not assured that the integration of 25 fb^{-1} will be in coincidence with Technical Stops, the Collaboration is developing a procedure for a fast brick replacement (about 8 hour shift) that could fit within longer inopportune accesses to the LHC tunnel. The installation of a new set of bricks will be performed at the same time as the the extraction of exposed ones. Two sets of tungsten plates will therefore be required.

[1]Design of wall structure and assembly tools performed in collaboration with the GWM Company, Suisio (BG), Italy.

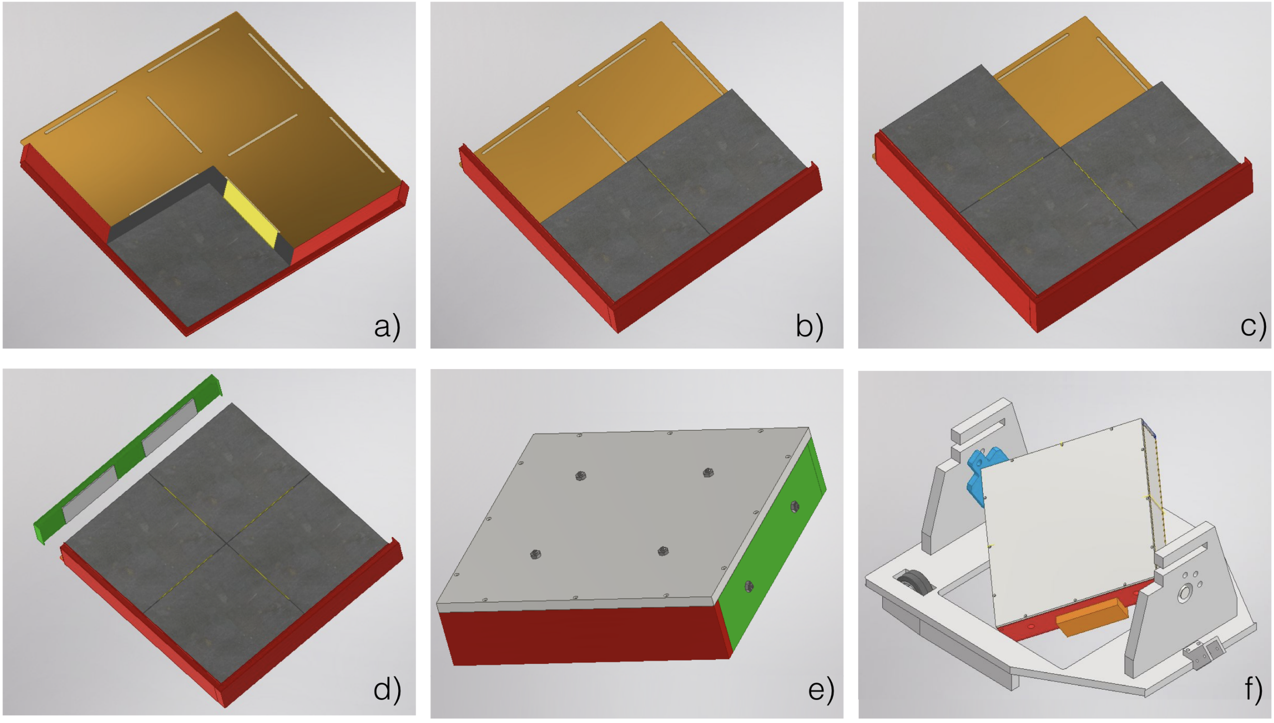

Figure 18: Sequence of the wall assembly procedure.

5.2.5 Chemical development

The development is a process that makes the latent image visible by a chemical amplification process. It is made of five steps:

- *Development* [Fujifilm Developer + Fujifilm Starter]: to turn a cluster made of a few silver atoms into a visible metallic silver grain
- *Stop* [Acetic acid]: to immediately stop the development process
- *Fix* [Fujifilm UR-F1]: to dissolve all residual silver halide crystals, leaving the metallic silver to form the image
- *Wash* [Water]: to remove all the silver thiosulphate complexes in the emulsion
- *Thickening* [Glycerine + Fujifilm Driwell]: to re-inflate the emulsion to their original thickness

About 500 L of raw chemicals will be used for the treatment of emulsion films used in each run, defined by a single set of films ($44\,\mathrm{m}^2$) and corresponding to a luminosity approximately equal to $25\mathrm{fb}^{-1}$.

5.2.6 Requirements for the emulsion facility

The chemical treatment of SND@LHC emulsion films will be performed in the dark room at CERN (see Figure 19), that will be equipped with the necessary tools to process 1200 emulsion films in one week.

Requirements for the emulsion facility are listed in the following:

- Temperature and humidity control
- Air-exchange system
- Two development chains with tanks suited for $192 \times 192\,\mathrm{mm}^2$ films
- Two thermostats for development-solution temperature control
- Racks for emulsion-film storage during and after chemical treatment
- Fridge for emulsion storage before brick production
- Room for chemicals storage
- Chemical-solution (raw chemicals + water) disposal ($\sim 1500\,\mathrm{L/run}$)

Figure 19: Picture of the dark room at CERN in building 169.

5.3 Mechanics

The mechanical structure of the SND@LHC target was designed to have a single support structure for both the five emulsion/tungsten walls and the five SciFi planes. It is made by a horizontal and a vertical rectified aluminum plate, as shown in Figure 20. The corner will act as a reference point for the positioning of the detectors. Each plane will be fixed to the structure by three pins.

The whole structure is supported isostatically on three points. Alignment feet are used to adjust the height of the structure in order to compensate for the inclined floor. Horizontal plates located below each foot are used for fine adjustment of the target position on the tunnel floor.

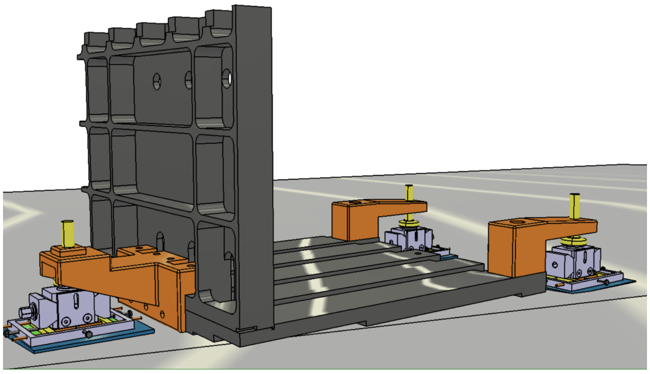

Figure 20: Mechanical support of the target.

5.4 Cooling and neutron shield

For the long-term stability of emulsion films, the temperature of the target will be kept at $15 \pm 1\,^{\circ}$C and the relative humidity in the range 50 to 55%. For this purpose an insulated box will be built around the target region and a cooling system will be installed, as shown in Figure 21.

The walls of the insulated box will be made of 3 cm-thick layers of boron carbide, that will act as shield from the neutron flux.

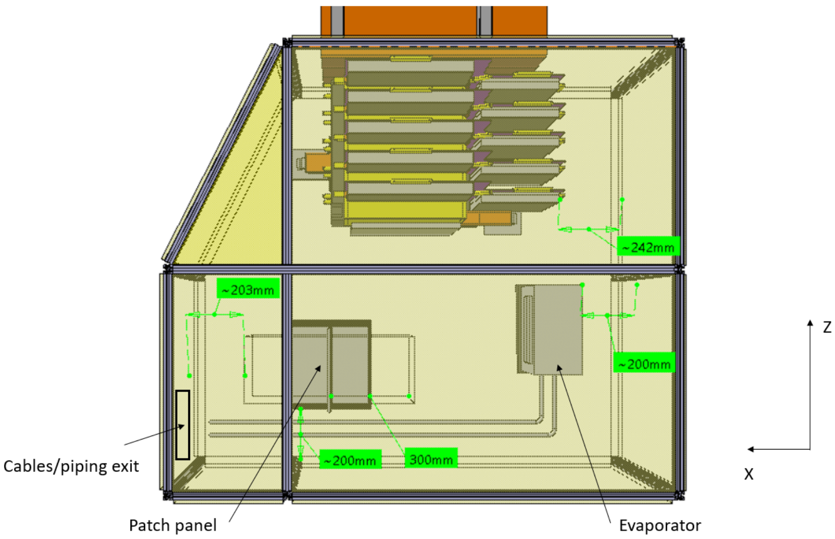

Figure 21: Insulated box made of 3 cm-thick layer of boron carbide surrounding the target region.

5.5 Microscopy

The emulsion readout is performed in dedicated laboratories equipped with automated optical microscopes, as the one shown in the left panel of Figure 22. The system analyses the whole thickness of the emulsion, acquiring tomographic images at equally spaced depths by moving the focal plane along the vertical axis.

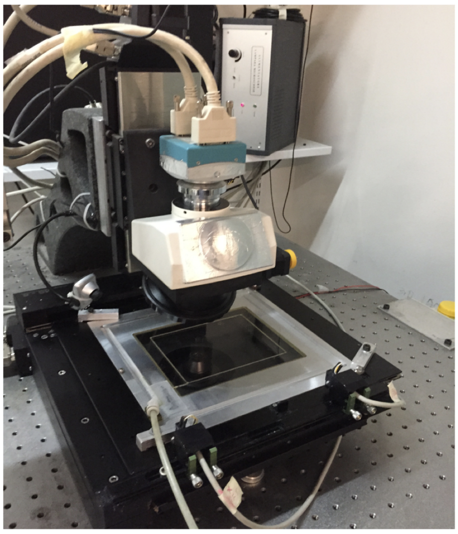

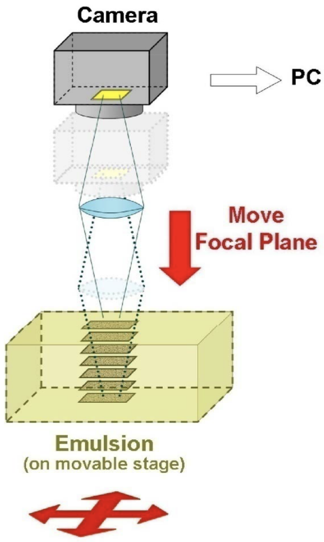

Figure 22: (Left) Optical microscope used for emulsion-film scanning. (Right) Schematic drawing of the scanning procedure.

A recently developed upgrade of the European Scanning System (ESS) [69, 70, 71] combines the use of a faster camera with smaller sensor pixels and a higher number of pixels, a lower-magnification objective lens and a new software LASSO [72, 73], allowing to increase the scanning speed to 180 cm^2/h [74], more than a factor ten faster than before. The lens of the microscope guarantees a sub-micron resolution and, having a working distance in z longer than 300 μm, allows for a scan of both sides of the emulsion film. In order to make the optical path homogeneous in the film, an immersion lens in an oil with the same refraction index of the emulsion is used. A single field of view is $800 \times 600\ \mu\mathrm{m}^2$. Larger areas are scanned by repeating the data acquisition on a grid of adjacent fields of view. The images grabbed by the digital camera are sent to a vision processing board in the control workstation to suppress noise.

The total emulsion-film surface to be scanned in SND@LHC is expected to be about 44 m^2 every six months, thus requiring at least five scanning systems fully devoted to this activity in order for the readout time to be approximately equal to the exposure time. Several groups of the Collaboration already have expertise in using the emulsion technology and the scanning stations previously used for the OPERA experiment. All scanning stations will be upgraded. The Collaboration is also interested in a small lab at CERN for installation of an emulsion scanning station.

5.6 Cost and schedule

The cost estimate for the target is summarised in Table 4. The timeline of construction, installation and operation phases related to the target is shown in Figure 23.

	Unit cost	Units	Cost single run	Cost six runs
Target				
Emulsion films	$2.4/m^2$	44 m^2	106	636
Emulsion transport	$0.02/m^2$	44 m^2	0.9	5.4
Tungsten plates (first set)	0.059/plate	1180 plates	70	70
Tungsten transport (first set)	0.008/plate	1180 plates	9.4	9.4
Tungsten plates (second set)	0.059/plate	1180 plates	70	70
Tungsten transport (second set)	0.008/plate	1180 plates	9.4	9.4
		Total	265.7	800.2
Mechanics				
Mechanical structure	3	1	3	3
Alignment feet	0.3	3	0.9	0.9
Design of mechanics	22	1	22	22
Tools for brick assembly	10	1	10	10
Brick packaging (first set)	0.7	40	28	28
Wall mechanical structure	1.2	10	12	12
Wall trolley	3	6	18	18
Transport to CERN	10	1	10	10
		Total	103.9	103.9
Emulsion facility				
Development chain	2	2	4	4
Tools for development	2	1	2	2
Racks for emulsion storage	0.1	20	2	2
Thermostats	2	2	4	4
Chemicals	0.014/L	500	7	42
Chemicals transport	0.004/L	500	2	12
		Total	21.0	66.0
Microscopy				
Microscope upgrade	20	5	100	100
Microscope maintenance	1	5	5	15
Local computing server	5	3	15	15
		Total	120.0	130.0
Grand total			510.6	1100.1

Table 4: Cost estimates in kCHF for the different components of the target.

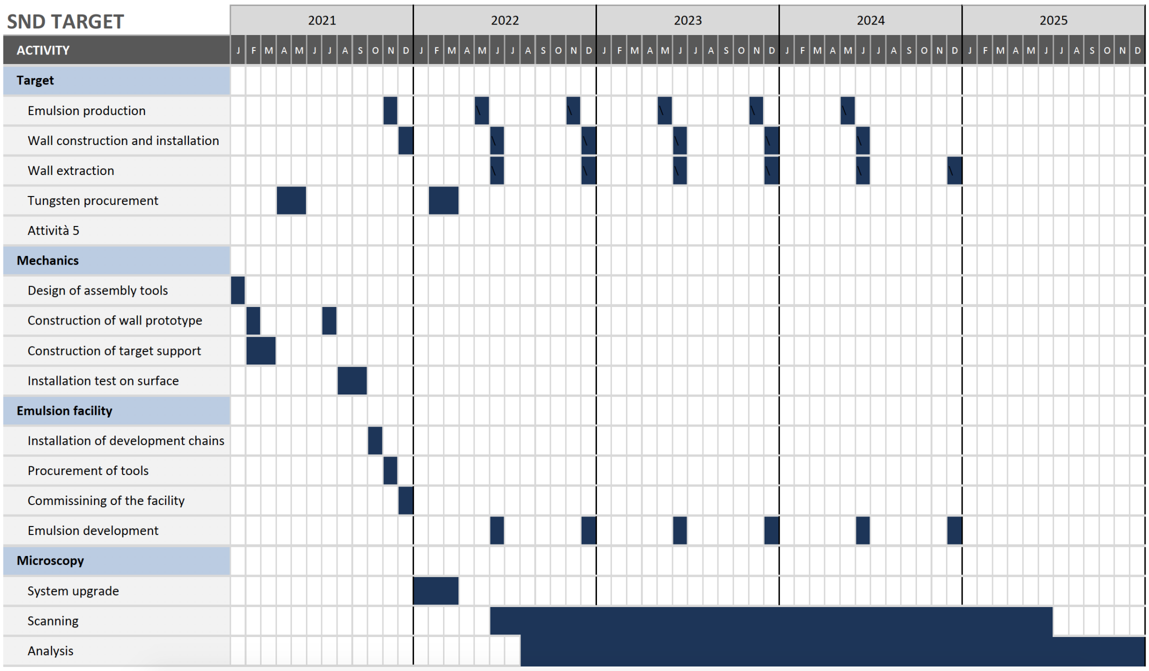

Figure 23: Timeline of the construction, installation and operation of the target.

6 Target trackers and electromagnetic calorimeter

6.1 Overview

The scintillating fibre (SciFi) tracker technology is particularly well suited for large surface tracking with medium spatial resolution and track density requirements. It can withstand low radiation as present in the SND@LHC detector location. It will play a key role to deliver the physics goals of the experiment by adding time and spatial information for particle showers and isolated tracks in order to disentangle piled up events in the emulsion and the reconstruction of events between emulsion walls. In addition, the target tracker allows to obtain energy information for electromagnetic and hadronic showers by measuring the shower profile at each SciFi plane.

The main components employed in the target tracker, fibre mats and photodetectors, were developed by the EPFL group for the LHCb SciFi Tracker [75]. While the LHCb SciFi Tracker and its readout electronics were developed with the goal of providing tracking information for single charged particles, it serves several purposes in the SND@LHC detector.

Connecting particle tracks between emulsion walls: this task requires a link between spatial position and event time information. This measurement is provided by a single x-y SciFi module acting as a seed in space and time for single particle or centre of gravity for particle showers. The expected single hit spatial resolution is of order of 50 μm.

Electromagnetic and hadronic sampling calorimeter: The five emulsion walls each representing about 17 radiation lengths, X_0, followed by the SciFi tracker planes represent a coarse sampled electromagnetic calorimeter with an average thickness of about 40 X_0.

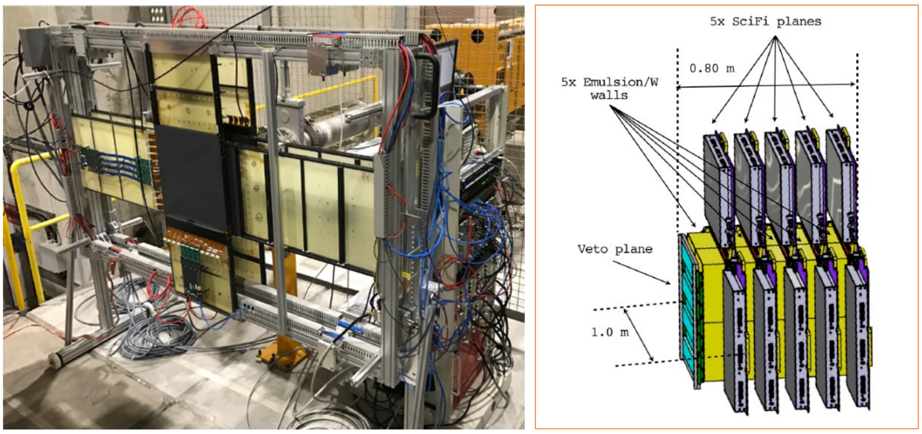

Figure 24: (Left) SHiP-charm SciFi modules equipped with readout. (Right) Target tracker region of the SND@LHC equipped with five SciFi planes and emulsion walls.

Four x-y SciFi planes equipped with the readout electronics, have been produced for the SHiP-charm experiment [76], and will be used for SND@LHC run in 2022 (Figure 24 left). An additional fifth SciFi plane is produced at EPFL specifically for the SND@LHC detector to reach the design target of five SciFi planes interleaved with five emulsion walls (Figure 24 right).

6.2 Mechanics

The detection layers are based on the blue light emitting Kuraray SCSF-78MJ scintillating fibres of 250 µm diameter with a decay time of 2.8 ns. The layers are made of six densely packed staggered fibre layers glued together forming fibre mats of 133 mm width and 390 mm length. Three fibre mats are integrated into a fibre plane with less than 500 µm dead zones between mats (Figure 25 right).

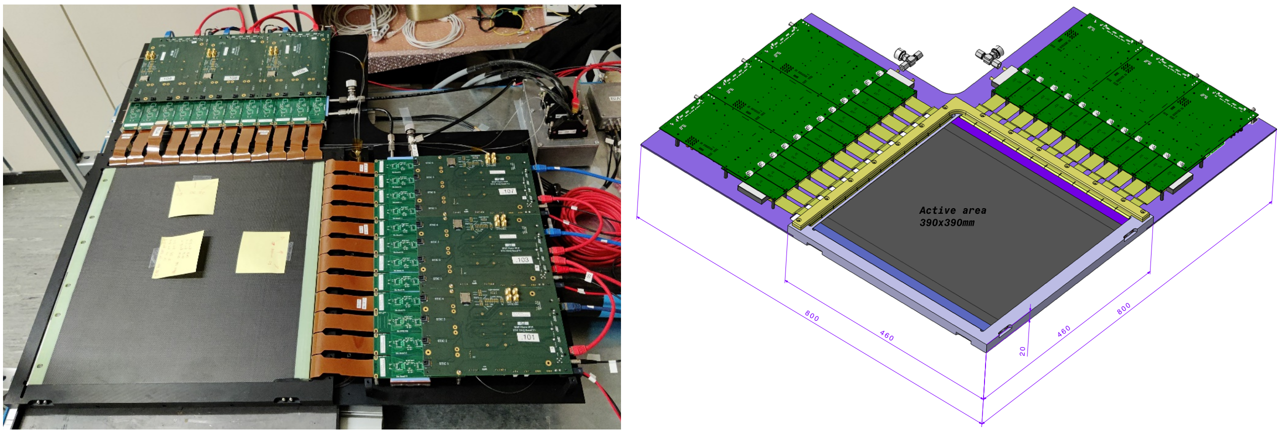

Figure 25: (Left) Aluminium support frame and one assembled SciFi plane. (Right) A SciFi x-y detection module with its corresponding readout electronics and the water cooling system for the front-end ASICs.

An important characteristic of the readout electronics is the power consumption of the front-end readout chip. The latest change to the TOFPET2 ASIC [77, 78, 79] allows to reduce the power consumption considerable to less than 2 W per 128 readout channels. Nonetheless, a water cooling system is required due to the large amount of readout electronics and the limited convection due to the neutron shield in the target region. The second largest power consumption is the DAQ FPGA. A heat sink connected to the large aluminium support of the module will allow to keep the temperature in the required operation range (Figure 26). The heat dissipation of the electronics into the target enclosure is estimated to be about 5 W per board or a total of 150 W for the complete target tracker system.

6.3 Powering

The target tracker requires five CAEN LV modules (8 channels), two CAEN HV modules (32 channels), and two CAEN power crates (6 slots) for operation.

6.4 Readout

The readout channel segmentation with 250 µm wide channels is provided by customised 128-channel SiPM array developed by the EPFL group together with Hamamatsu for the LHCb experiment (Figure 27). A total of about 3000 channels are required for an x-y module in the target tracker.

The readout is situated outside of the acceptance and consists of the photodetector located at the fibre module's edge, a short Kapton flex PCB and the front-end electronics board. Light

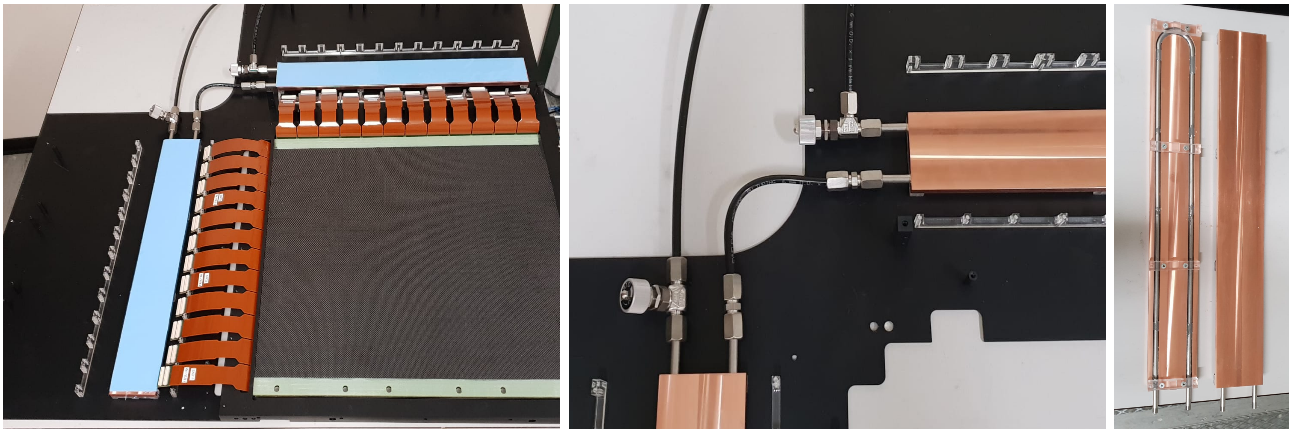

Figure 26: (Left) Cooling system for the readout electronics mounted on the SciFi plane. (Center) Cooling pipes with two valves for each module. (Right) Copper cooling plates.

shielding of the assembly is ensured by a seal implemented at the flat Kapton flex section enclosing the photodetectors and the entire fibre region. This part doesn't require any cooling as the heat dissipation of the SiPMs is sufficiently low.

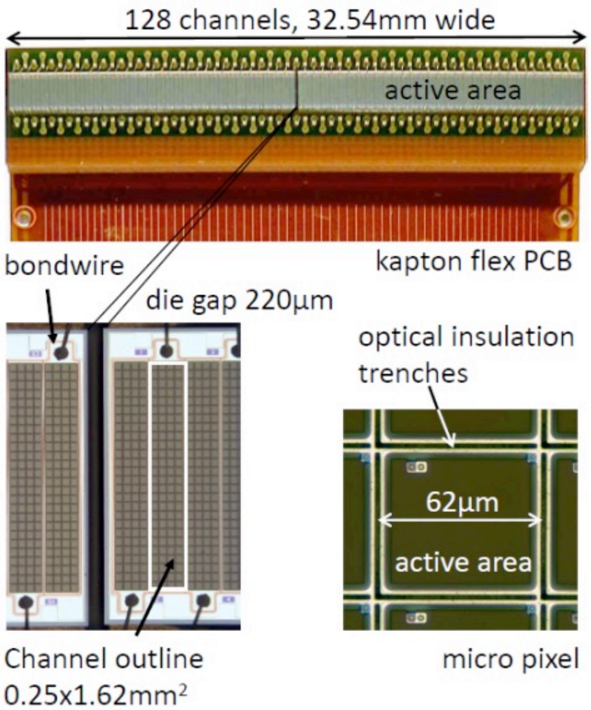

Figure 27: SiPM arrays used for the light detection in the SciFi.

A readout system based on the STiC ASIC [80], which allows to have both energy and the time measurement with the SciFi, has been developed and tested in several test beam campaigns during 2018–2019. A coincidence time resolution (CTR) of 350 ps between two planes of the size 133 mm×133 mm has been demonstrated with minimum ionizing particles. This corresponds to a single plane time resolution of about 250 ps. For multiple tracks or showers, the total number of photons is significantly larger and the time resolution is expected to be considerably better. Further developments led to the choice of an alternative readout ASIC: The TOFPET2 ASIC [77, 78, 79], which is commercially available and is produced and developed by PETsys. It is better suited for this application regarding the dynamic range of the signal amplifier and discriminator thresholds, lower noise and better uniformity of detector response. It allows for more accurate amplitude measurement required for the shower shape information, and to improve energy measurement, electron-hadron separation, and shower centre-of-gravity measurement (effectively, shower tracking) crucial for extrapolation between the emulsion bricks.

6.5 Calibration

The TOFPET2 electronics provide an electrical injection signal, synchronous and without time difference to all TOFPET2 FE chips on one board (signal routing has identical path length). This allows for a first order time calibration between channels on the same board. Subsequently, a fine time calibration based on muon tracks among different boards and layers can be used to correct and verify the time calibration based on the collected data during the runs. The studies from a DESY test beam which took place in October 2019 show that based on the initial time alignment, the time calibration for channels can be improved using single track data producing multiple hits in all ten SciFi layers. This procedure requires propagation time compensation in the SciFi.

The SciFi technology employed for the target tracker has been developed and optimised for the LHCb tracking purposes. Its use for shower detection has two main limitations. A large number of x-y space points produced simultaneously produce a huge number of ghost hits. For large numbers of tracks in a small area, only a projection of the shower profile onto the x-y plane can be obtained. The pixelised silicon photomultiplier (SiPM) suffers from non-linear amplitude response due to the limited number of pixels. With a MIP response of 25 photoelectrons (pe) and a total of 104 pixels per channel, a pixel occupancy of almost 50% is expected for a shower track density of 2 tracks per channel. Beyond this track density, a strong non linear response of the detector signal is expected. The saturation is of statistical nature and can be corrected to make the detector response linear. The energy calibration for the SciFi tracker requires a GEANT4-based Monte Carlo simulation. The DESY test beam data will be used to validate the simulation set up, but it cannot be used for the final detector calibration as the test beam was carried out with a different detector configuration: different electronics, based on STiC3 ASIC; different electromagnetic shower leakage due to shorter modules; different light yield due to 7 layer SciFi and shorter modules. A post measurement test beam can also be envisaged.

6.6 Alignment

The initial mechanical alignment based on photogrammetric survey measurements is done with the aid of the precisely positioned targets on the each SciFi plane frame (Figure 28). Sufficient high energy muon tracks over the full acceptance are present during all runs. The muon track data will also be used for relative alignment between emulsion and target tracker.

6.7 Cost and schedule

Expected cost of the target tracker is summarised in Table 5. The listed cost does not include power supply and DAQ which are described in detail in Section 8.7. The construction and

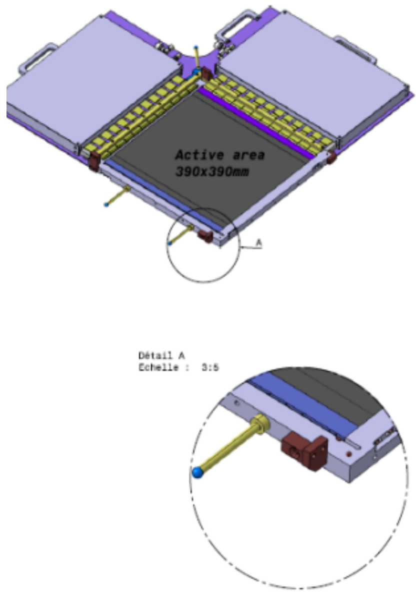

Figure 28: Target pins for the precise assembly of the detector and initial plane alignment.

installation schedule is shown in Figure 29.

Item	**Needed**	**Spares**	**Quantity**	**Unit price [CHF]**	**Cost [kCHF]**
Fibre mat	5	0	5	1500	7.5
Mechanics	5	0	5	5000	25.0
SiPM (24 per module)	5	0	5	7200	36.0
Total					**68.5**

Table 5: Target tracker cost estimate.

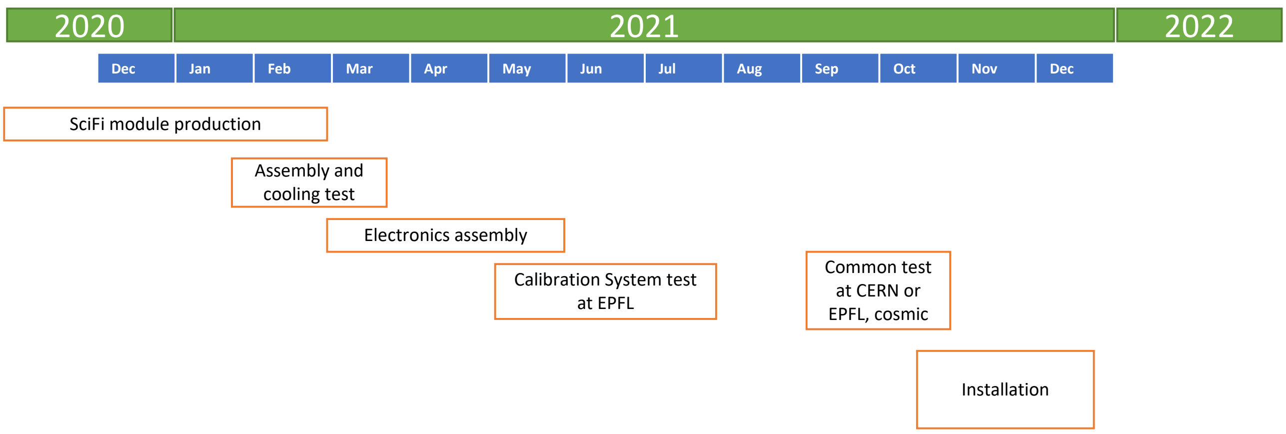

Figure 29: Schedule for the target tracker assembly, testing and installation. The production started in Fall 2020.

7 Muon system and hadronic calorimeter

7.1 Overview

The muon detector is located downstream of the ECC/SciFi target detector. It will identify muons, crucial to identifying muon neutrino charged-current interactions. In combination with the SciFi, it will serve as a non-homogeneous hadronic calorimeter, enabling measurement of the energy of hadronic jets. Eight scintillating planes will be interleaved between layers of iron slabs 20 cm thick, which will act as passive material. Muons will be identified as being the most penetrating particles through all eight planes.

The iron blocks available at CERN are 24× FT822 ($80 \times 20 \times 20\,\text{cm}^3$). Three stacked blocks comprise one passive layer covering an area $80 \times 60\,\text{cm}^2$. Each layer is followed by a scintillating detector plane.

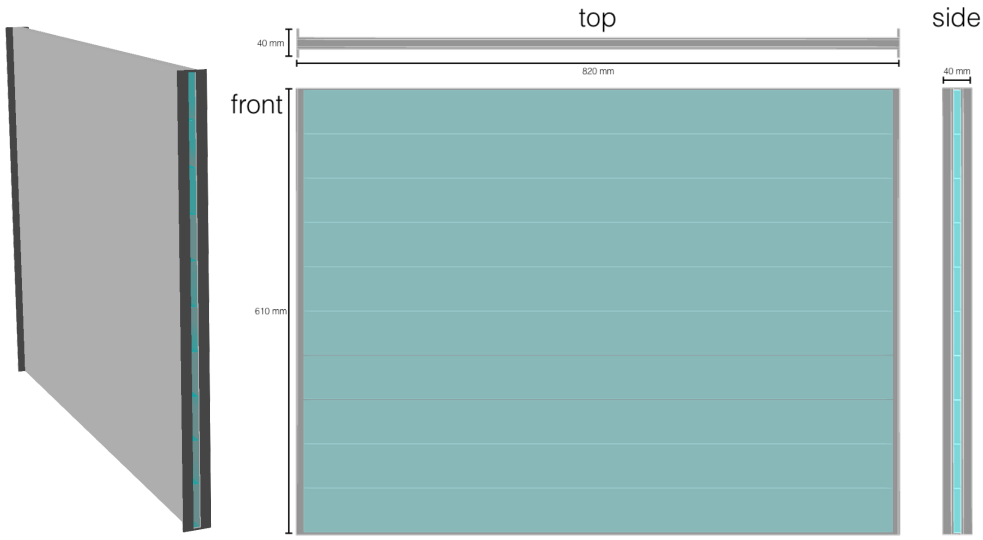

Figure 30: (Left) View of an upstream layer. (Right) Drawing of the mechanical frame with the bars overlaid.

The first five upstream planes are similar to the upstream veto detector, albeit with different dimensions, and will be used as a timing detector for traversing particles. One layer comprises ten bars, each with dimensions $81 \times 6 \times 1\,\text{cm}^3$, that have been tested in two test beam campaigns at the CERN PS in 2017 and 2018 [81, 82].

Each layer covers an active area of $81 \times 60\,\text{cm}^2$. As with the veto system, each bar is read out on both ends by eight Hamamatsu S14160-6050HS SiPMs. An example of an upstream plane can be seen in Figure 30.

The last three downstream planes consist of two layers of thin bars, one arranged horizontally and one arranged vertically, allowing for a spatial resolution of less than 1 cm. A downstream plane can be seen in Figure 31. The horizontal planes comprise 60 bars, each measuring $81 \times 1 \times 1\,\text{cm}^3$, and read out by a single Hamamatsu S14160-6050HS SiPM on both side. The vertical planes have 60 bars of $60 \times 6 \times 1\,\text{cm}^3$, each bar read out by a single SiPM from the top.

The space between bars represents a small inefficient area. For this reason the use of bars with a rhomboidal cross section, as shown in Figure 32, is being investigated. This will allows to reduce inefficiencies between bars while maintaining the number of bars. A small prototype

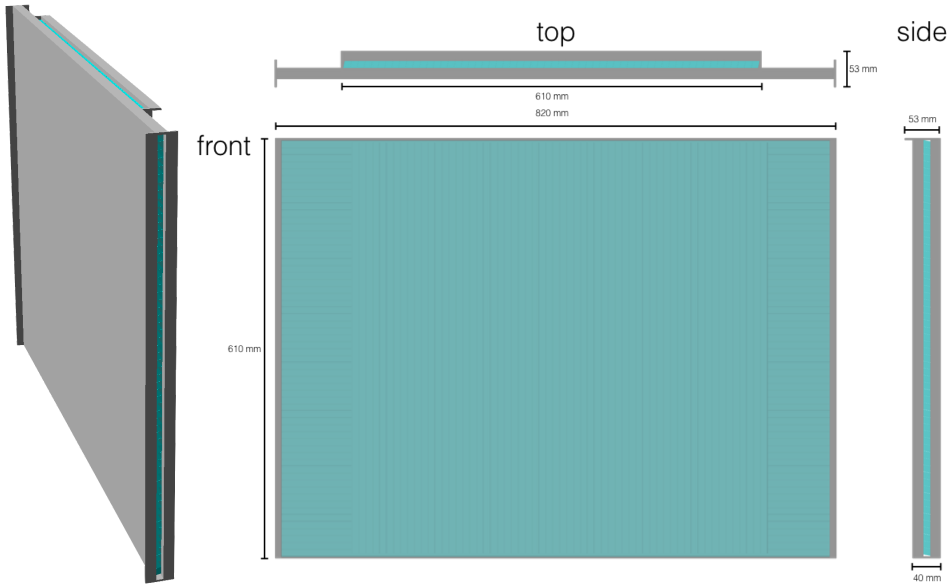

Figure 31: (Left) View of a downstream layer. (Right) Drawing of the mechanical frame with the bars overlaid.

is being constructed and tested to investigate how such a shape would affect the light yield and the effect of charge sharing between bars when a particle passes through the overlap region.

7.2 Mechanics

The mechanical structure of the upstream layers is similar to that of the veto system. The sides are flared out at the end to allow for the size of the PCB. The width is fixed to be as wide as the iron blocks of 80 cm, plus some tolerance. This moves the PCB end cap to outside the iron blocks and allows to minimize the thickness of the detector plane in between the iron walls to that of the bar thickness plus the thickness of the aluminum wall of the frame. The space between the iron blocks where the detector plane fits totals 26 mm, comprising 16 mm for the detector and a 5 mm gap on each end to compensate for uncertainties in the thickness of iron walls, as is illustrated in Figure 33.

The structure of the downstream planes is shown in Figure 31. The space between the iron for the downstream planes totals 34 mm; 29 mm for the bars and aluminum, plus a 5 mm gap on either end between the iron walls. As the corner of the most downstream layer is in conflict with the tunnel wall, it will be laterally shifted by 22 mm, without changing its dimensions.

Both the upstream and downstream layers will be supported by aluminum rails from the top. The planes will be hung from the rails by adjustable hinges. The frame is supported by three adjustable feet sitting on top of the iron blocks, as seen in Figure 34.

7.3 Readout and powering

The upstream layers will be read out on both ends by 80 SiPMs mounted on a PCB which is attached the end of the mechanical frame in a similar fashion to the veto detector. The downstream layers will be readout out by a PCB with 60 SiPMs on each end for the horizontal plane, and 60 SiPMs from the top for the vertical plane. The total number of channels for the

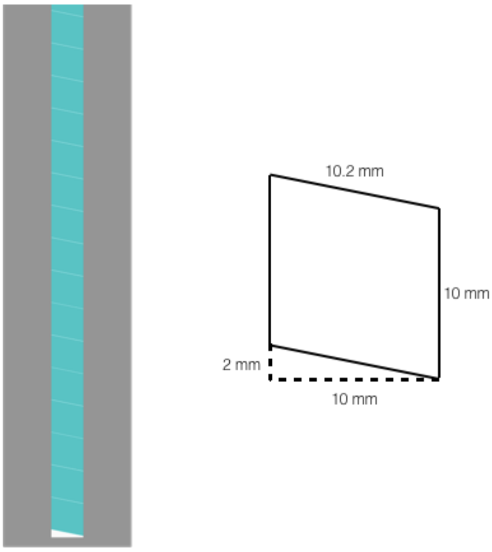

Figure 32: (Left) Side view of a downstream plane showing the stacking of the rhomboidal shaped bars. (Right) Cross sectional view of a bar showing the rhomboidal shape of the bars.

whole muon system is thus 1340. The DAQ is similar to that of the veto system, where 19 FE boards will be read out by five DAQ boards. The bias voltage of the SiPMs is again provided through the DAQ boards and the CAEN LV and HV power in the NIM crates will be shared with the veto system.

7.4 Calibration

The timing calibration for a given layer will be performed with cosmic muons on the surface before installation, similar to the calibration of the veto system. Calibration between different layers will be carried out after installation by using background muons from the beam. The calibration can then be retroactively applied after the initial data taking.

In order to accurately reconstruct the deposited energy in the bars, the response of the bars to different particle numbers has to be known. The response to $2.5\,\mathrm{GeV}/c^2$ muons from the CERN PS on bars with the same cross section but different length was measured in a 2018 testbeam, where roughly 60 p.e. over eight SiPMs were collected at a distance of 60 cm along the bar, as seen in Figure 35. The response to low energy particles will be measured with single bars on the surface while the response to larger number of incoming particles can be studied in testbeams on single bars after installation and applied to the data retroactively.

7.5 Alignment

After installation, each individual detector plane will be horizontally aligned with respect to the nominal collision axis by survey. The length of the aluminum bar at the bottom of each layer will be extended by 50 mm to align each plane with a tool as shown in Figure 36. The placement of the planes along the line of site will be fixed by the hanging frame from above. The alignment tolerance should be on the mm level to avoid degradation of the spatial resolution of the three downstream planes.

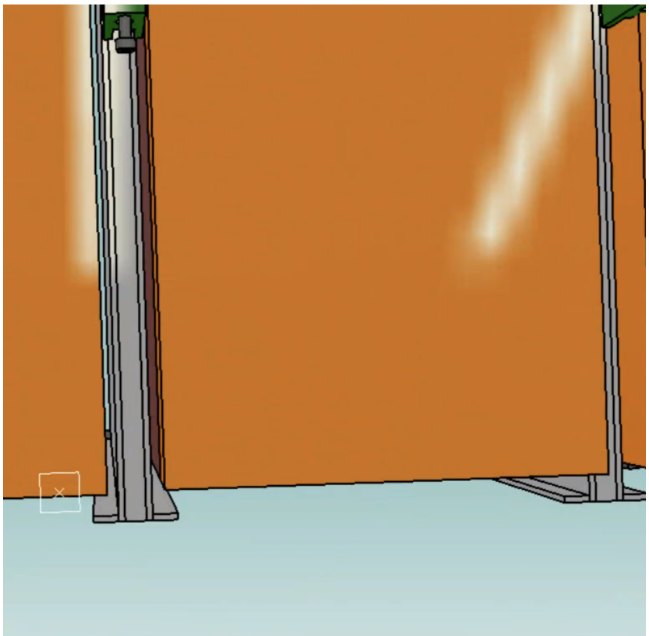

Figure 33: Top view of an upstream plane illustrating its placement between the iron slabs.

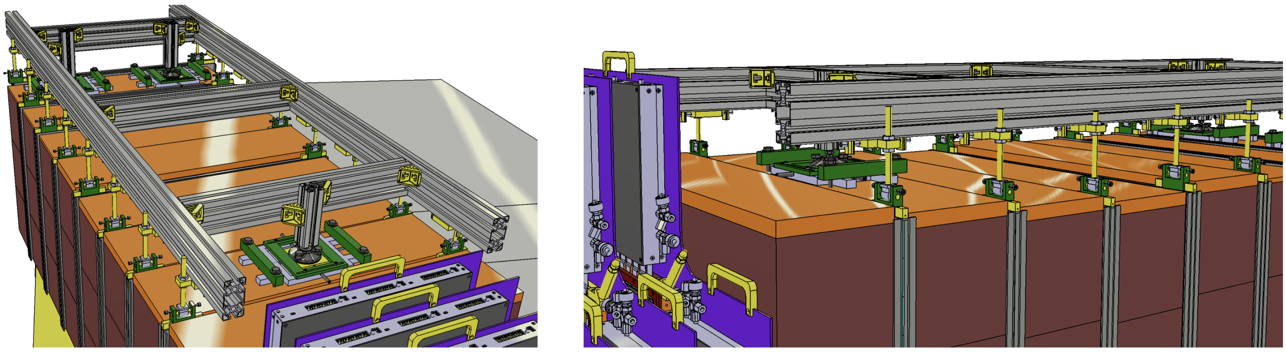

Figure 34: The aluminum support structure showing the support of the planes from the top.

7.6 Cost and schedule

The cost estimate of the muon system is presented in Table 6. The cost includes spares, as with the veto system. The cost of the DAQ and power supplies is also an effective cost and included in Section 8.

The schedule through installation of the muon system is presented in Figure 37. The construction of the mechanical frames for each layer will last through March. The PCB development should finish by the end of April. Due to the much larger number of bars and SiPMs, the wrapping of bars and mounting of the SiPMs will take longer than the veto system, and will last through April, May and June. Integration of the DAQ will take place from June through July. Installation of the mechanical support and iron blocks will be performed in October. The timing calibration for individual planes on the surface will last until installation of the scintillating planes, and between planes in the cavern after installation. The installation of the muon planes will take place in the second half of November. The energy calibration and efficiency

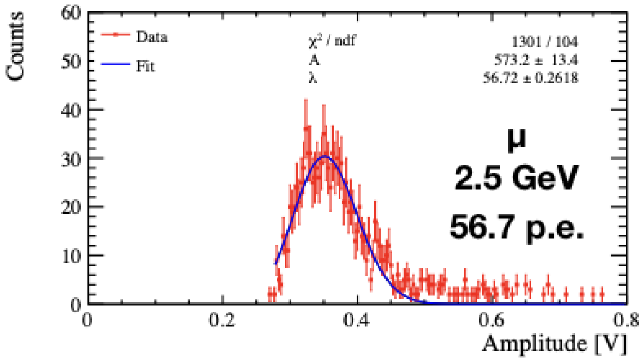

Figure 35: Amplitude of the signal of an EJ200 bar with the same cross section as the upstream planes measured with 2.5 GeV/c^2 muons. Roughly 60 p.e. were collected with eight SiPMs at the end of the bar.

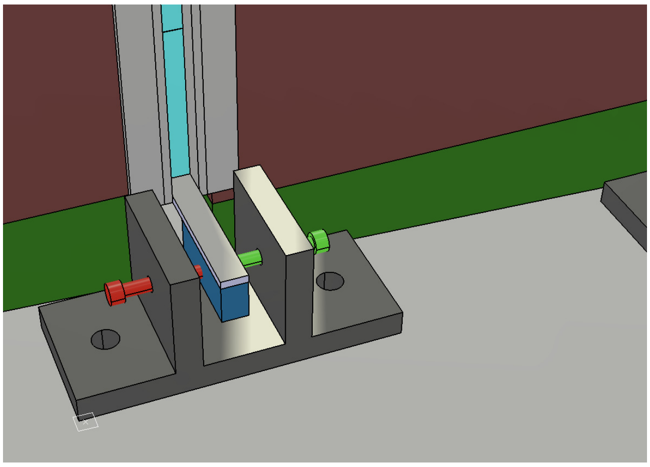

Figure 36: View of the tool used for horizontal alignment of the individual planes.

measurements will be carried out on the surface with individual bars and will take place before and after commencement of data taking. Alignment of the detector and integration with the rest of the experiment will take place in December until the start of data taking.

	Unit cost [CHF]	Units	Cost [kCHF]
Detector			
Upstream Bars	200	55	11.0
Downstream Horz. Bars	105	183	19.2
Downstream Vert. Bars	90	183	16.5
SiPMs	25	1'400	35.0
		Total	81.7
*DAQ Boards**			
PCB, components, assembly	1'189	6	7.1
Enclustra FPGA module	357	6	2.1
TOFPET2 ASIC	352	48	16.9
FE board	100	24	2.4
FE cables	59	6	0.4
		Total	28.9
*Power Supplies**			
CAEN LV module	638	6	3.8
CAEN HV module	1'375	6	8.3
CAEN crate	1'286	6	7.7
		Total	19.8
Mechanics			
Mechanical structure	500	8	4.0
PCB end-cap	100	19	1.9
Transport to CERN	0100	8	0.8
		Total	6.7
Grand total			137.2

Table 6: Cost estimates for different components of the muon system. *These are effective costs for the whole system. They are included in the cost estimates of the DAQ system.

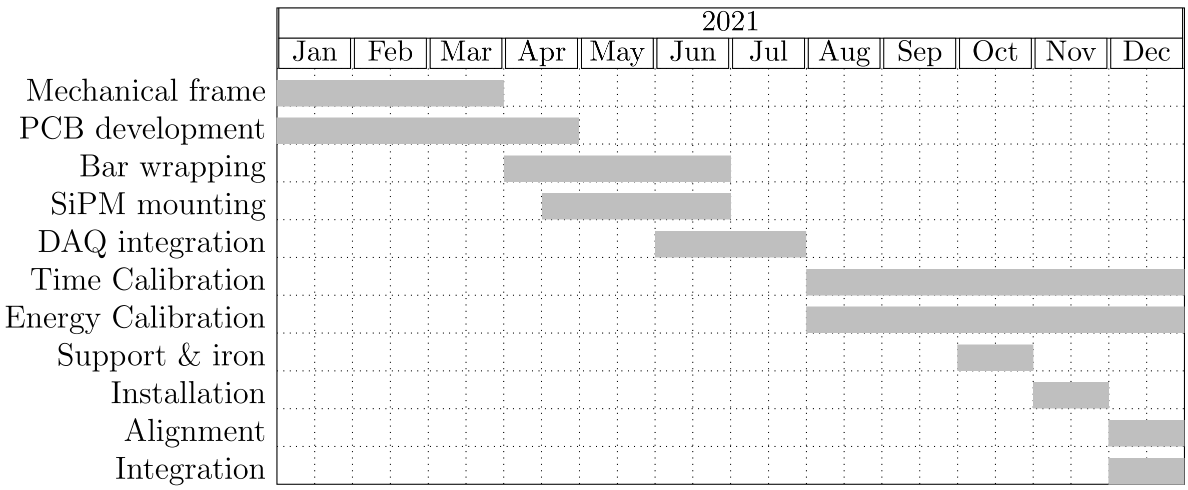

Figure 37: Schedule for construction and installation of the muon system.

8 Data acquisition

The SND@LHC detector features two types of active sub-systems:

- Scintillator bars read out by SiPMs, used for the veto and the muon systems;
- Scintillating fibres read out by SiPMs, used for the SciFi tracker.

These sub-systems will be read out with the same DAQ electronics, based on a main DAQ board, featuring a Cyclone V FPGA, and up to four front-end (FE) boards, based on the TOFPET2 ASIC, by PETsys [77].

The detector will utilise a total of 36 DAQ boards, which will run synchronously with the LHC bunch crossing clock. It will be operated in a trigger-less fashion, i.e. all hits recorded by each board will be transmitted to the DAQ server and stored. Noise reduction is performed at the front-end level by setting an appropriate threshold for each channel or disabling noisy channels.

8.1 DAQ architecture

The DAQ system of the active sub-systems of SND@LHC (veto, tracker and muon system) is composed of:

- 36 DAQ boards, described in Section 8.2. They read out the signals from the SiPMs, digitize them and send the recorded data to a server.
- One Trigger Timing Control (TTC) crate, described in Section 8.3, to receive the LHC clock and orbit signals from the Beam Synchronous Timing (BST) system and transmit them to the DAQ boards, allowing them to run synchronously.
- One server, located in the service building SR1[2], which receives data from the DAQ boards and combines it into events, as described in Section 8.4, and saves them to disk.
- One control PC, located in TI18, which controls the TTC crate and the environmental sensors.

Details about each component are given in the following sections. A schematic representation of the DAQ system is shown in Figure 38.

8.2 DAQ electronics

The DAQ board, shown in Figure 39, is based on the Mercury SA1 module from Enclustra [83], featuring an Altera Cyclone V FPGA. The main characteristics of this board are:

- four high-speed connectors for the FE boards;
- TTCrx ASIC [84] with an optical fibre receiver, used to receive the clock and synchronous signals from the TTC system;
- 1 Gb Ethernet port, used for data and command transmission;

[2]Building 2175 at CERN, where the server rack will be located.

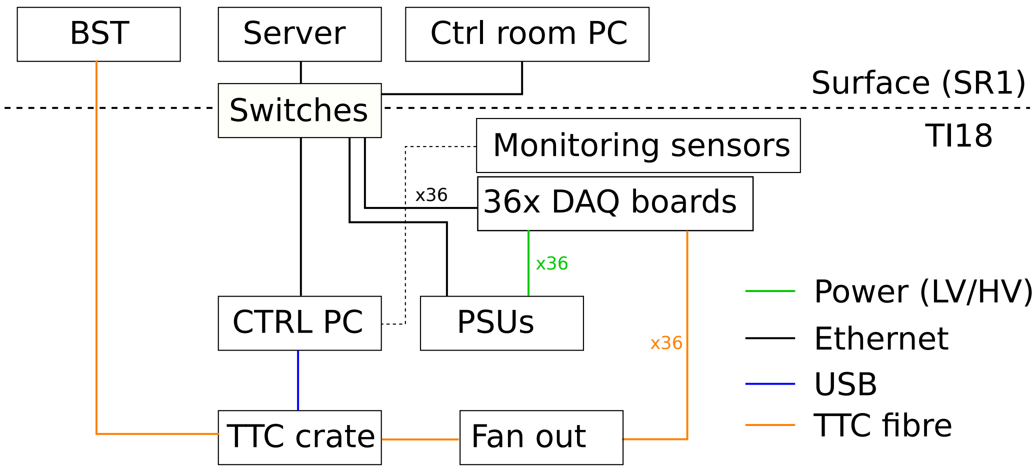

Figure 38: Simplified scheme of the SND@LHC DAQ system.

- LEMO connector to deliver the bias voltage to the SiPMs.

Each DAQ board collects the data digitized by the FE boards and transmits it to the DAQ server, running on a PC in SR1. If the connection to the server is lost, data will be stored locally on the DAQ boards until the connection to the DAQ server is re-established and data can be transmitted. The amount of data that can be buffered on each DAQ board will depend on the size of the installed MicroSD card (even 1GB is enough for several hours of missing connection).

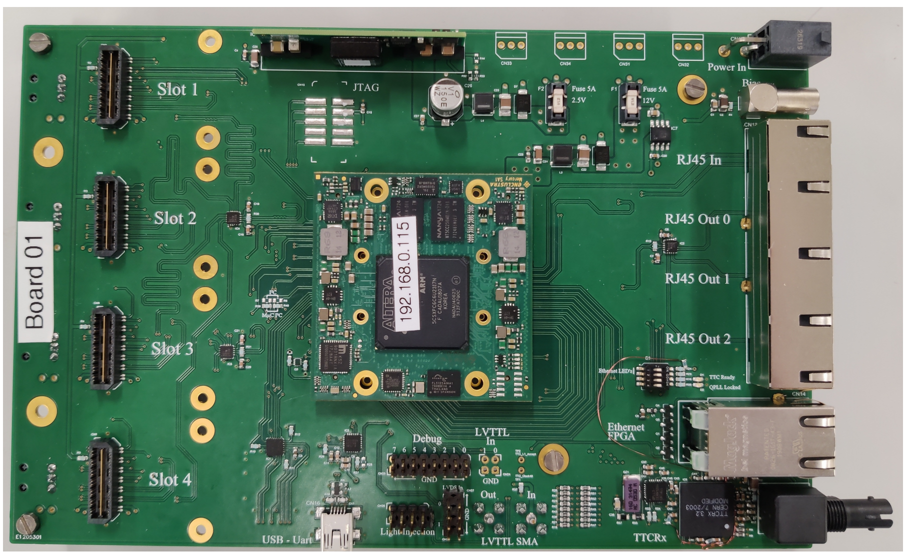

Figure 39: The DAQ board. The four FE board connectors are visible on the left, the TTCrx and optical receiver on the bottom-right, the Enclustra Mercury SA 1 module in the centre.

The FE board, shown in Figure 40, contains two TOFPET2 ASICs, used to read out the SiPMs, and temperature monitoring capabilities. Each TOFPET2 ASIC can read out 64 channels, for a total of 128 channels per FE board and 512 per DAQ board. The TOFPET2 records all the hits that exceed a predefined threshold and provides energy and timestamp information. Other significant characteristics are:

- per-channel energy and time threshold configuration,
- possibility to disable channels (e.g. due to noise),
- 30 ps timestamp binning,
- time and energy calibration through pulse injection.

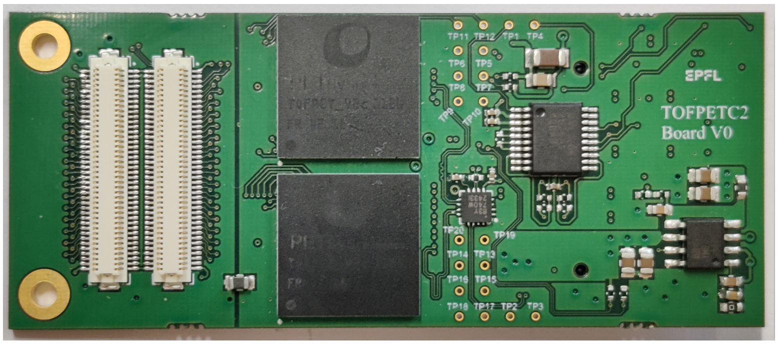

Figure 40: The FE board. The two TOFPET2 ASICS (centre) and the SiPM connectors (left) are visible.

A preliminary characterization shows that a noise rate of 10 Hz can be achieved with a threshold of 5 pe, and can be further reduced to 1 Hz at a threshold of 6 pe. Furthermore, when coupled to a SciFi mat, a coincidence time resolution of 320 ps can be achieved, which corresponds to a channel time resolution of $320\,\text{ps}/\sqrt{2} = 226\,\text{ps}$.

Given the number of read-out channels per plane reported in Table 7, a total of 36 DAQ boards and 143 FE boards will be used, distributed as per Table 8.

Subsystem	Planes	Channels per plane	Channels total
Veto	2	112	224
SciFi	5	3072	15 360
Upstream muon	5	160	800
Downstream muon	3	180	540
Total			16 924

Table 7: Detector read-out channels.

8.3 LHC signals and TTC system

The LHC clock (40.08 MHz, the bunch crossing frequency) and orbit (11.245 kHz, the revolution frequency of the LHC) signals are obtained from the Beam Synchronous Timing (BST) system, transmitted over an optical fibre using the TTC system, along with other information such as the machine mode, the beam type and energy, the GPS absolute time, etc.

The BST signal will be received by a dedicated board, BST-TTC, that will extract the clock and orbit signals, clean the clock using a PLL, and distribute them to the detector using

Subsystem	Planes	DAQ boards total	FE boards total
Veto	2	1	4
SciFi	5	30	120
U/D muon	8	5	19
Total		36	143

Table 8: Number of electronics boards per sub-system.

the TTC system. The board will be based on the same type of board as used for the read-out of the detector, described in Section 8.2) In case of absence of the BST signal, the board will provide a substitute clock to the system. In addition, it will recover the beam information and transmit it to the DAQ server over Ethernet, where it will be merged with the data from the detector.

Variations of several nanoseconds in the phase of the clock are to be expected due to temperature changes. For this reason the absolute timing offset will be calibrated with the timestamps of the muons generated by the collisions in the ATLAS interaction point.

The clock and synchronous commands are distributed to the DAQ boards using the TTC system, consisting of a TTCvi and a TTCex modules [84]. The TTCvi receives the clock and orbit signals, and generates the A-channel (trigger) and B-channel (synchronous and asynchronous commands) signals, which are encoded and transmitted by the TTCex.

The TTCvi module can be programmed and controlled using the VME bus. A USB-to-VME converter allows it to be programmed from the control PC.

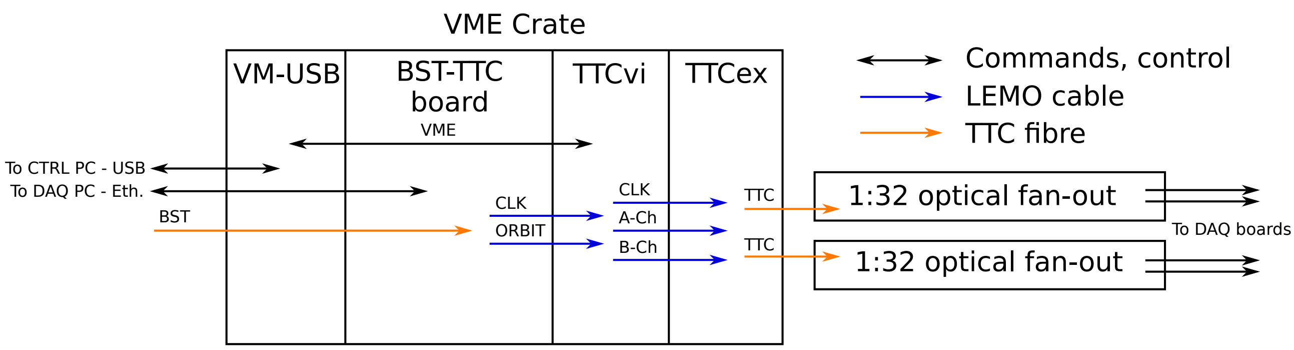

Figure 41: Simplified scheme of the SND@LHC TTC system.

8.4 Event building, data-quality and storage

Each DAQ board transmits all the recorded hits to the DAQ server, where event building is performed. The hits are grouped into events, based on their timestamp, and saved to disk as a ROOT file. The DAQ boards will also transmit periodic triggers received from the TTC system, and the DAQ server will verify that all the boards are running synchronously, requesting a re-synchronization if this is not the case.

The data is saved to disk without any further processing, to prevent loss of information and keep the disk utilisation to a minimum. Still, a preliminary online processing (such as clusterisation, preliminary track reconstruction, etc.) is performed by the DAQ server for data quality monitoring purposes.

The DAQ server will write the recorded data to a local disk. It will then be periodically transferred to EOS, from where it can be used for offline reconstruction and data analysis.

8.5 Detector Control System (DCS)

The DCS will monitor the temperature and humidity in the cold box, the functionality of the chiller, and the current drawn by the DAQ boards and the SiPMs.

The temperature inside the cold will be constantly monitored and logged and an alarm will be raised if it rises over 17 °C. The power to the DAQ boards inside the cold box will be removed if the temperature rises over 18 °C to protect the emulsion films. Alarms will be also raised if a failure is detected in the chiller, or in the LV or HV power supplies.

The possibility to use the JCOP Framework (Joint COntrols Project) [85] for the DCS will be investigated.

8.6 DAQ software

The DAQ software is composed of several parts and their relations are shown in Figure 42. The tasks of each component are summarized below.

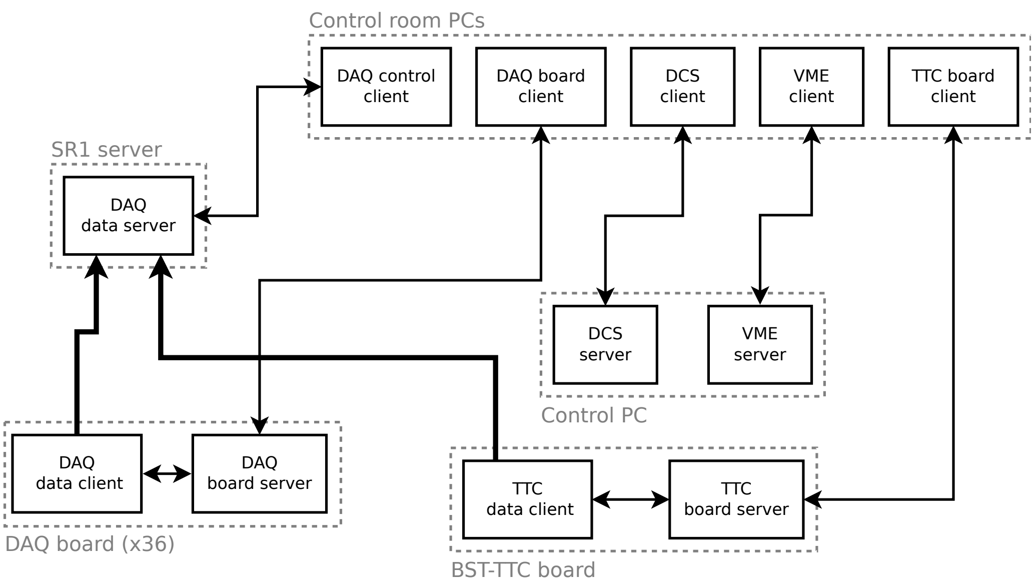

Figure 42: Relations between software components in SND@LHC. A thick arrow denotes data, a thin arrow denotes control and commands.

DAQ data server Running on the server in SR1, collects the data packets from the DAQ boards, builds the events and saves the data to disk.

DAQ data client Running on each DAQ board, reads the data from the FPGA, builds packets and transmits them to the DAQ server.

DAQ board server Running on each DAQ board, performs the setup and monitoring of the data acquisition and the calibration of the front-ends.

TTC data client Running on the BST-TTC board, retrieves the data received from the BST system (such as beam status, beam energy, etc.) and sends it to the DAQ server, where it will be merged with the data from the other subsystems.

TTC board server Running on the BST-TTC board, performs the control and monitoring of the signals received from the BST system, raises an alert if the BST clock is lost or if any other issue occurs.

VME server Running on the Control PC in TI18, configures and issues commands to the TTCvi module through the VM-USB module (e.g. to send synchronization triggers or B-channel commands).

DCS server Running on the Control PC in TI18, reads the temperature and humidity sensors, controls and monitors the power supplies and the chiller. Raises alerts if any issue occurs.

DAQ control client Running on a PC in the control room, sets up the DAQ data server and monitors its activity, showing data-quality control information.

DAQ board client Running on a PC in the control room, issues commands to and monitors the status of the DAQ boards.

DCS client Running on a PC in the control room, controls the DCS and monitors its status.

VME client Running on a PC in the control room, can be used to send commands and triggers using the TTC system.

TTC board client Running on a PC in the control room, monitors the BST and TTC systems.

The various clients on the control room PCs can be merged into a single application, to ease the communication between the various components.

8.7 Cost and schedule

The estimation of the DAQ cost is reported in Table 9. The schedule for the preparation of the DAQ is expected to proceed as follows:

- present–03/21: debugging of the DAQ and FE boards, development of DAQ and control software;
- 03–04/21: production of the necessary boards, debugging, software development;
- 04–07/21: procurement of the necessary parts for commissioning, assembly of the boards in the different planes, test of the final assembly before commissioning (Section 10).

Item	Needed	Spares	Quantity	Unit price [CHF]	Cost [kCHF]
Power supplies					
CAEN LV module (8 CH)	5	2	7	2233	15.6
CAEN HV module (32 CH)	2	1	3	6417	19.3
CAEN crate (6 slots)	2	1	3	6000	18.0
CAEN booster	1	0	1	968	1.0
				Subtotal	**53.8**
DAQ boards					
DAQ board	36	7	43	1000	43.0
Enclustra FPGA module	36	7	43	300	12.9
TOFPET2 ASIC (64 channels)	282	60	342	290	99.2
FE board	141	30	171	100	17.1
Cables, fibres, patch panels	36	0	36	300	10.8
FE cables	21	5	26	50	1.3
				Subtotal	**184.3**
Clock/sync distribution					
BST-TTC board	1	1	2	1000	2.0
Enclustra module	1	1	2	300	0.6
VME crate (VME8004B)	1	0	1	4000	4.0
TTC modules	1	0	1	1400	1.4
USB to VME module	1	1	2	2343	4.7
Optical fan-out	2	0	2	500	1.0
				Subtotal	**13.7**
Computers					
Server (SR1)	2	0	2	4000	8.0
Disk module (SR1)	1	0	1	1500	1.5
Control PC (TI18)	1	0	1	2000	2.0
				Subtotal	**11.5**
Control room					
Control room PC	4	0	4	500	2.0
Monitor	8	0	8	200	1.6
Keyboard, mouse	4	0	4	50	0.2
				Subtotal	**3.8**
Total					**267.1**

Table 9: DAQ cost estimation.

9 Installation and integration

Particular effort has been invested in studying the integration of SND@LHC, to guarantee the feasibility of the implementation in the TI18 tunnel, a cost efficient integration, and an optimal installation strategy. The study has collected the detector requirements [86] and analysed the various aspects of survey, electrical engineering, cooling and ventilation, transport, radiation to electronics, networking infrastructure, safety and radiation protection together with the corresponding CERN equipment and service groups. The groups include EN-SMM, HSE-OHS, HSE-RP, EN-HE, EN-EL-EIC, EN-EL-FC, IT-CS-DO, EN-CV, IT-CS-CS, EN-STI-BMI, EN-EA-AS, BE-OP-LHC, TE-CRG-OP, TE-CRG-CI, EN-SMB, IT-CS, TE-MPE-EP and EN-ACE-OSS. The proposed plan has been presented at the "Intégration Cellule LHC" meeting, which is in charge of the integration studies of the LHC. No showstoppers or issues have been identified.

9.1 Component transport

The services and the sub-components required to operate the detector will be transported on a trolley from the surface level to the LHC tunnel through the PM15 elevator (3 tonne load capacity) and, then, transported along the LSS1R section of the LHC tunnel to UJ18.

In order to reach the experimental area in the TI18 tunnel, the components must be either passed over or under the LHC machine in UJ18. Small components will be passed below the machine with a low-profile trolley about 11 cm high (see Figure 43). A passage of about 80 cm width and 37 cm height under the LHC machine has been cleared from cables. The height of the trolley plus reserving 2 cm for clearance below the QRL cryostat, leaves 24 cm in height for the component to be transported. The maximum footprint that can be transported is 76 cm in width and 1 m in length. The components will be transported in protective boxes on the trolley. The dimensions are sufficient to allow passing the iron blocks and the target emulsions bricks, and all other smaller components. A dedicated trolley will be used for the emulsion bricks, as shown in Figure 43. It has been optimised to pass below the LHC machine.

A few larger components will need to be passed above the LHC machine. A hoist with 500 kg capacity is foreseen to be fixed to the existing top platform present in UJ18. The available space below the hoist for the transport channel is H:2.0 $\times$ W:1.0 $\times$ L:3.0 m^3. The volume of the largest item to be passed above the machine is $75 \times 90 \times 150\,\mathrm{cm}^3$. A protective structure dimensioned for a 2 tonne falling object [87] will be installed for the protection of the LHC machine and the cryogenic line. The QRL protection for SND@LHC, together with the hoist and the maximum transport volume, integrated in UJ18 is shown in Figure 44.

A transportable jib crane with a total capacity of 1 tonne (see Figure 43) is foreseen for the final installation of the heaviest detector components, such as the iron blocks and the emulsion bricks, in TI18. A manual winch will be installed in order to climb the slope of the TI18 tunnel. All components that will need handling assisted by mechanical lifting equipment will be fitted with dedicated lifting points.

A list of the most demanding components to be handled is shown in Table 10, together with their weight and overall dimensions.

A detailed plan for the exchange of the emulsion bricks in the LHC Technical Stops will be established between transport, radiation protection and the detector teams. The length of the stops is typically one week. Effort is put on making sure that the actual replacement

Figure 43: The various tools that will be used to transport the SND@LHC detector components.

procedure can be done in one eight-hour shift. Time for access and transport should be added to this. It should be noted that the passage through UJ17 at the level of the LHC machine is constrained by a shielding chicane. As a result, transport devices and components to be shipped underground, or evacuated from TI18 to the surface, must not exceed a width of about 1 m. It is not considered, but the central part of the shielding can be dismounted, should it be needed, to get direct access for trailers and trucks during YETS. The overhead amounts to two days.

9.2 Detector services

As described in Section 5, the temperature of the emulsion target must stay at about 15 °C in order to prevent possible fading effects. In addition, the SciFi electronics of the target tracker needs demineralised water cooling. A dual system of one operating and on spare chiller will be installed for redundancy, together with an insulated box around the SND@LHC target system, and an evaporator. The operating chiller will provide cooled water to the electronics and to the evaporator. The latter will maintain the temperature at (15 ± 1) °C, and control the humidity in the range between 50 and 55%, in the refrigerated insulated box. The expected power consumption of the water cooling is about 2.5 kW. Figure 45 shows the conceptual scheme of the cooling system. The structure of the insulated box will be made from aluminium profiles. Mineral wool or a fire barrier duct wrap will be used as insulator. The walls will also include a 3 cm layer of boron carbide, or alternatively a layer of borated polyethylene, to provide shielding against thermal neutrons. A 20 cm separation between the walls and the extreme edges of the SciFi is required to accommodate the bending radius of the SciFi cables, which is about 10 cm. This also ensures a good air circulation within the box. A cable feed through (about $30 \times 30\,\mathrm{cm}^2$) will be located in the corner of the wall for the routing of the detector cables to the patch panel (30 cm wide and 50 cm high). The SciFi planes will be connected to the cooling circulation in parallel with an inlet water temperature per plane of 15 °C. The total

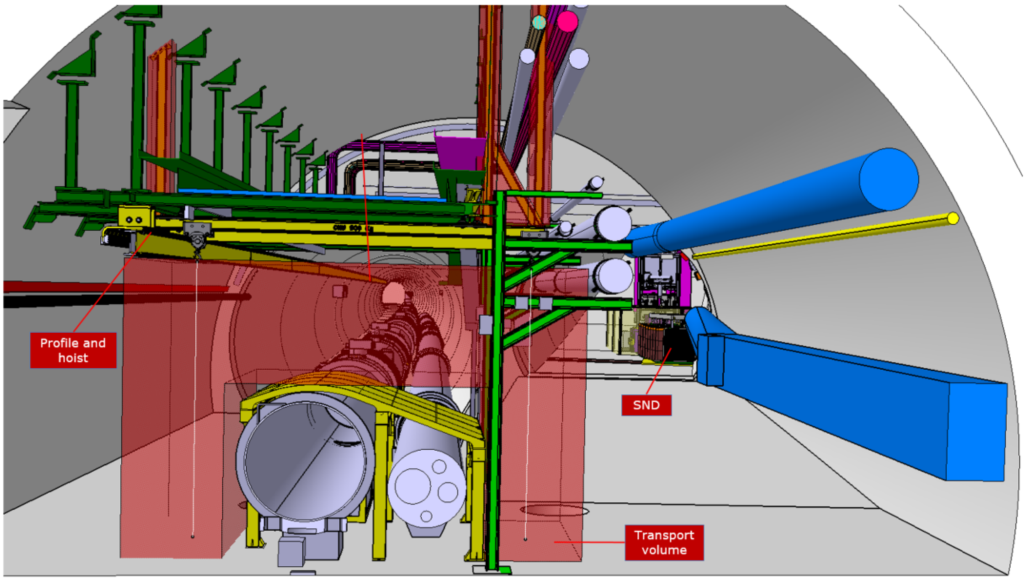

Figure 44: Integration of the hoist and transport volume in UJ18.

heat load to be extracted is about 0.35 kW. A total water flow of 6 l/min is expected to be sufficient, that is, 1.2 l/min per SciFi plane. One manifold for inlet and one for outlet per plane is required plus one spare, thus, seven pairs of connections in total. The PLC of the cooling plant will be connected to the network switch in TI18 in a scheme which is similar to what was set up for FASER.

The design of the cooling plant will take into account the maximum transport dimensions. Potentially it will be composed of two modules to be passed above the LHC machine and then assembled in-situ. It will be connected to the compressed air of the LHC for the internal valve control and for the air supply to maintain the required humidity in the insulated box.

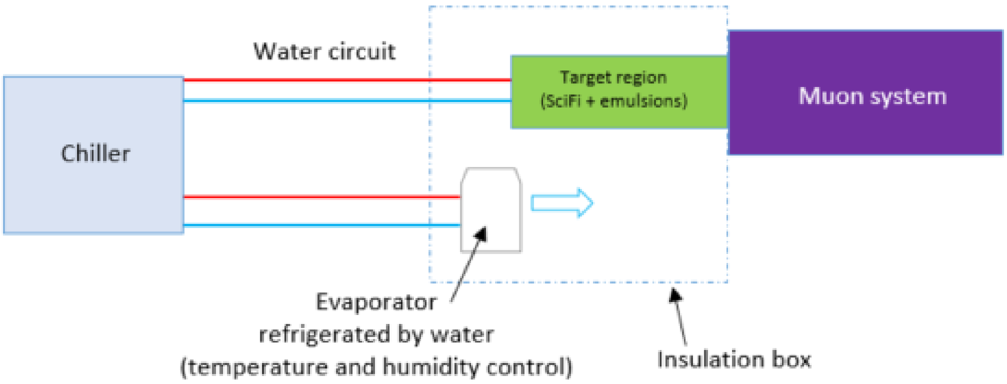

Figure 45: Proposed cooling scheme for the SND@LHC detector.

Under normal circumstances the redundancy of the cooling system should protect against a cooling unit failure and maintain a satisfactory environment in the insulated box until the next opportunity for access. Nevertheless, interlocks on the environment will be implemented to guarantee the integrity of the emulsion films with the help of remote monitoring of the temperature and humidity, and of the status of the cooling pump. In addition to raising an

Part	Units	Dimensions [cm^3]	Unit weight [kg]
Target region			
Emulsion plane	5	$42 \times 42 \times 10$	160
SciFi modules	5	$100 \times 90 \times 25$	15
Target support horizontal plate	1	$55 \times 70 \times 40$	62
Target support vertical plate	1	$65 \times 40 \times 50$	9
Clamps for alignment feet	3	$20 \times 10 \times 5$	5
Muon system			
VETO plane	1	$60 \times 60 \times 20$	4
Muon timing plane	5	$80 \times 80 \times 20$	6
Muon xy plane	6	$80 \times 80 \times 20$	8
DAQ boards	1	$60 \times 40 \times 20$	2
Cables and fibres	2	$60 \times 40 \times 40$	10
Long bars for muon system	2	$200 \times 10 \times 5$	5
Short bars for muon system	3	$40 \times 10 \times 5$	1
DAQ			
Power supplies	2	$60 \times 40 \times 40$	10
Crates	2	$50 \times 30 \times 80$	20
Patch panel	1	$40 \times 60 \times 20$	5
Cables and fibres	2	$60 \times 40 \times 40$	10
FT822 iron block	24	$80 \times 20 \times 20$	230
Small iron blocks	8	$80 \times 20 \times 5$	63
*Electronics rack**	2	$50 \times 50 \times 170$	25
*Cooling rack**	1	$170 \times 95 \times 120$	250
Chiller	2	$100 \times 60 \times 40$	80
Horizontal plate for grid covering	1	$100 \times 100 \times 4$	200

*Can be divided in smaller pieces to reduce weight and dimensions

Table 10: The most demanding sub-components, in terms of volume and weight, to be transported.

alarm, the SciFi electronics will be powered down automatically if the temperature in the insulated box rises above 18 °C, or the water temperature of the SciFi rises above 25 °C.

The electrical services required to supply the detector have been identified. The maximum electrical power supply currently available in TI18 is 11 kW. This is sufficient to supply the chillers, SciFi, timing detector, muon system, and the electronics racks. The integration of the electrical services include:

- An electrical distribution box located at the entrance of the TI18 cavern.
- Two AUGs connected to the existing network.
- Permanent lighting consisting of three normal lamps and two emergency lamps connected to the existing UJ18 network.
- Two 220 W sockets.

The integration of the electrical infrastructure is shown in Figure 48. Empty and reusable cable trays are already present in TI18. If needed, a new tray can be installed for local cable routing on the wall next to the detector.

SND@LHC requires six optical fibres between TI18 and the surface rack located in SR1, which include:

- Data and control of the detector, including monitoring of the cooling system, on two pairs of fibres (one active and one spare) for 1GB/s Ethernet.
- Beam Synchronous Timing (BST) signal.
- One additional spare fibre.

A set of twelve optical fibres will be installed. Figure 46 shows a sketch of the routing of the fibres. Even if the chosen route is longer, an installation along the Long Straight Section was excluded since the fibres would have to be removed for the installation of the HL-LHC during LS3.

Two 19-inch fibre patch panels will be installed in the TI18 electronics rack. From there to RE18, the optical fibres will be blown through the 600 m tube to be installed and connected to the already existing patch panels in RE18. The fibre infrastructure is already in place from RE18 to the rack with the SND@LHC computer servers in SR1.

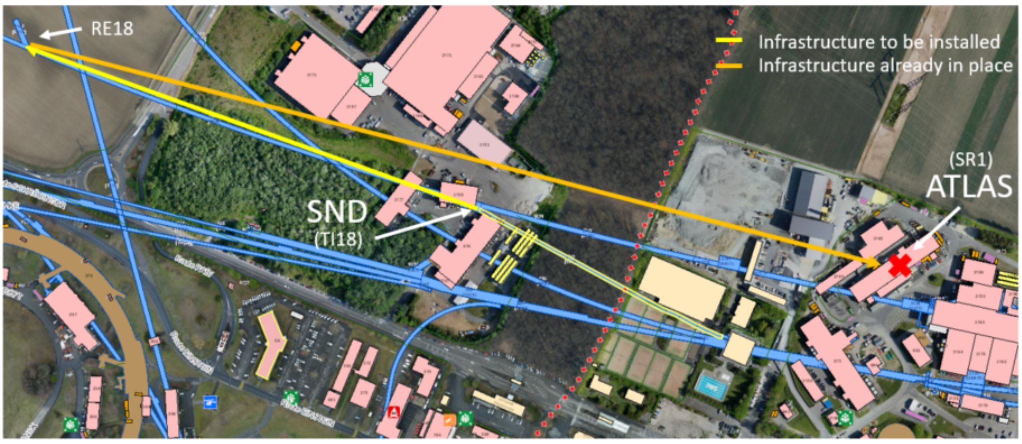

Figure 46: Sketch of the routing of the optical fibres.

It has been agreed that the SND@LHC equipment can be installed in the already defined rack for FASER in SR1. The rack will be accessible during beam operation and the servers only require normal air cooling. The power supply of the reference PowerEdge R440 server consumes about 0.7 kW. The weight per server is about 18 kg and the dimensions are standard W:19in × H:1.7in × L:28.7in. In addition, a redundant 10 TB of intermediate local storage is foreseen although the data will be automatically transferred to EOS, or similar, on file closure. To include future extensions, 4 kW of power in the SR1 rack has been requested to support a maximum of four servers. Ethernet switches will also be located both in the SR1 and the TI18 rack. Figure 47 shows the SND@LHC network infrastructure.

The detector will have an online control room located in an ordinary office on the CERN site. The actual scheme of shifts will be defined later. For more details about the DAQ and controls, see Section 8.

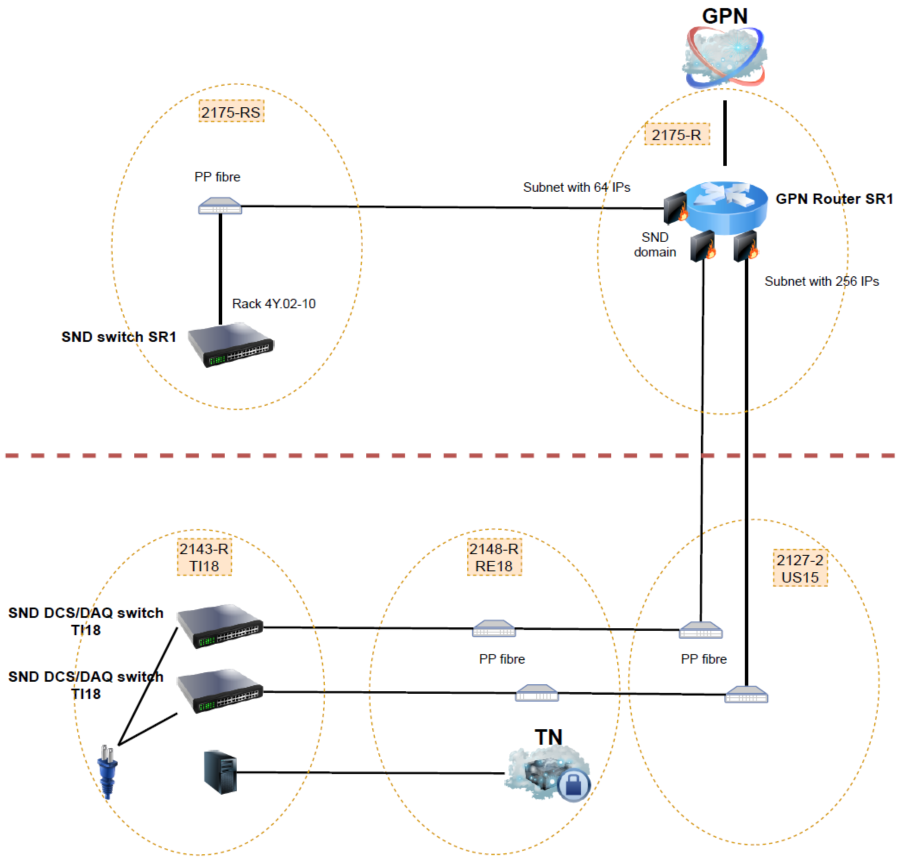

Figure 47: Scheme for SND@LHC network infrastructure. Courtesy of IT-CS.

9.3 Detector alignment during installation

Studies show that an absolute alignment and measurement accuracy of about 5 mm is sufficient for SND@LHC. An accuracy of about 0.2 mm is required for the internal alignment of the detector sub-components (i.e. SciFi plane, emulsion brick walls etc.). The design of the alignment system has been developed together with EN-SMM.

There is a clear line of sight (LoS) between the location of the detector and the LHC machine. Survey fiducial supports will be mounted on the walls in TI18 in order to setup a geodetic control network. To link the detector position with respect to the machine coordinate system, every detector component requiring alignment will be equipped with three survey fiducial markers. The ATLAS collision axis has already been marked on the TI18 tunnel floor during the FASER studies. 3D scanning of the area after the installation is foreseen for integration purposes and to update the survey database.

The design of the alignment strategy divides the detector into two independent assemblies:

- The target region will be supported by a single support structure and will be aligned by means of three feet, as shown in Figure 20. The platform feet will be fixed to the floor by a horizontal grout base. Each emulsion brick wall is made of a single $40 \times 40\,\mathrm{cm}^2$ brick to be aligned mechanically by their own assembly frame. A kinematic system mechanically fixed by three points to the support structure and positioned by three pins has been designed for the emulsion bricks and the SciFi planes. Each wall will have a surface on the corner to place the survey fiducials. They can be fiducialised by a Romer arm on the surface if clear references (fiducial and/or surfaces) are included on the bricks.

- The iron blocks are piled up and positioned by space holders to guarantee the required space for the insertion of the planes of scintillator bars. A floating structure, fixed to the top of the iron walls and supported by three points fixed to two neighbouring walls, will support the planes of scintillator bars (see Figure 34). Each plane of scintillator bars will be supported at three points (two on top and one on the side), leaving free a surface for the installation of fiducials.

The iron walls will have base plates attached to the floor and aligned with the help of three screws. The plate will be rigidly fixed to the floor by filling the space between the plate and the floor with grout. This operation will be done for the first four iron walls. However, the last four walls will be on a single plate passing over the existing drain. In the same way, grouting on both sides of the drain will be cast.

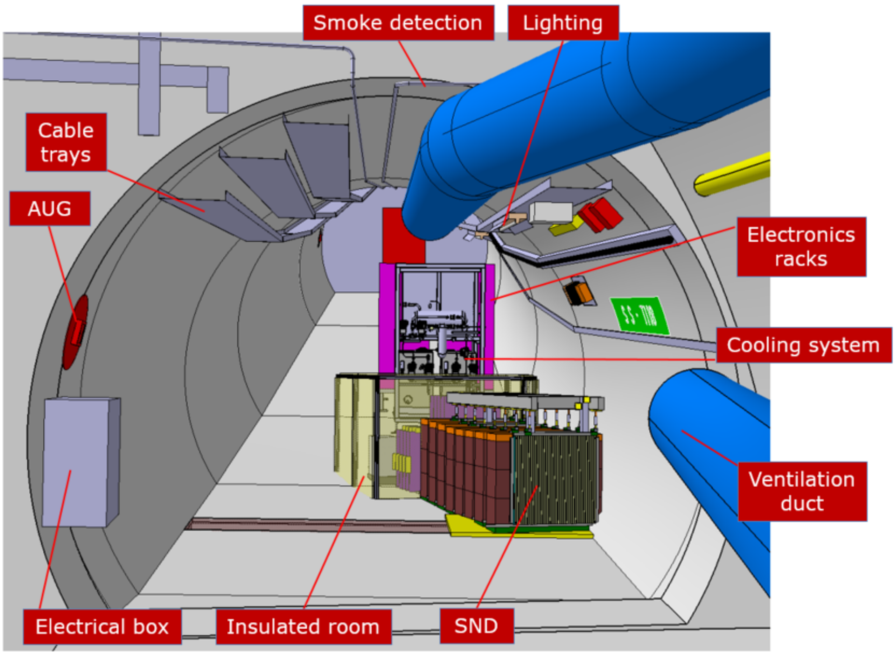

Figure 48: Integration of the SND@LHC in TI18.

9.4 Integration

The SND@LHC detector will be located at the downstream end of TI18. Figure 5 shows the different sub-systems of the detector. The integration of the detector in TI18 is shown in Figure 48. The works to prepare the experimental area, the infrastructure, and the services required for the installation and operation of the detector, are specified in Refs. [88] and [89] and include:

1. UJ18:

    - Raising a section of the cable tray (EN-EA-AS) together with rerouting of cables.

- Installation of the QRL protection, including drilling fixations in the floor (EN-HE-PO).
- Displacement of a light (EN-EL-EWS) to make space for the installation of a rail and manual hoist (EN-HE-PO) above the LHC machine.
- Connect and route a power cable for the SND@LHC from the distribution box within UJ18 to a connection box to be installed in TI18 (EN-EL-EWS).
- Displace current electrical box above footbridge by EN-EL-EWS.
- Pull cables for AUG and lights to be installed in TI18 (EN-EL-EWS).

2. TI18:
   - Removal of the unused ventilation duct within TI18 (EN-CV).
   - Installation of a closed circuit cooling system (EN-CV).
   - Installation of an electrical distribution box for the experiment together with normal lighting, emergency lighting, power sockets and AUGs (EN-EL-EWS).
   - Installation of racks for the detector electronics (group to be determined).
3. SR1 to TI18:
   - Installation of optical fibre tubes from RE18 to TI18 (EN-EL-FC).
   - Pulling of optical fibres (EN-EL-FC).
4. From the compressed-air LHC network (location to be determined) to TI18:
   - Compressed air pipe routing.
5. SR1:
   - Installation of detector electronics for control and readout inside the SND@LHC rack.
   - Connection of the optical fibres between the patch panel and the SND@LHC rack (EN-EL-FC).

9.5 Radiation effects to electronics (R2E)

In order to assess the risk of radiation-induced failures of the SND electronics it is necessary to estimate the key quantities of interest in the TI18 gallery, focusing on the fluences of thermal neutrons and High Energy Hadrons (HEHs) that quantify the risk of Single Event Effects (SEEs). It is to be noted that the radiation levels are low enough to disregard possible cumulative damage.

As already shown in Section 3.2, hadronic radiation in TI18 is mostly originating from beam-gas interactions from the incoming beam. The measured values during 2018 [90], scaled to a nominal Run 3 operation year, yield expected annual levels of 2×10^7 and 1×10^8 cm^{-2}yr^{-1} HEHs and thermal neutrons, respectively. Coherent predictions can be obtained from the DPMJET/FLUKA calculations used in Section 3.2 to derive the physics backgrounds, e.g. through further analysis of the neutron energy spectrum in TI18, shown in Figure 12.

The above annual values of HEH and thermal neutron fluence are almost an order of magnitude larger than the limits that the Monitoring and Calculation Working Group (MCWG) of the R2E project considers to declare an area as radiation safe for pure commercial electronics systems performing critical functions. However, it is to be noted that these R2E limits consider distributed systems, whereas for a single unit system, they can be regarded as pessimistic. Also, the measured levels correspond to the intersection between TI18 and UJ18, and the equipment will clearly benefit from being positioned inside the TI18 tunnel. Hence, it is expected that commercial electronics will operate in R2E-safe conditions in TI18.

9.6 Radiation Protection

A detailed study of the radiation protection aspects has been launched to evaluate the residual radiation levels during the LHC technical stops and the possible level of activation of the detector components in the TI18 tunnel. The study assume the LHC operational conditions of Run 3. The preliminary considerations are based on the radiological assessment performed for the FASER experiment in the TI12 tunnel [90], for which no showstoppers have been identified. Since similar residual radiation levels are expected in TI18, it is realistic to assume that access of personnel is possible for one or two days during the technical stops to replace the emulsion bricks.

9.7 Personnel access

Personnel access will follow the LHC standard procedures. The SND@LHC experimental area is reached from UJ18 via the bridge already installed above the magnet MBB13.R1 to pass over the LHC machine. The dedicated procedure for the personnel access during the installation is being defined together with the Departmental Safety Officer and the concerned CERN groups for a safe work performance with the LHC machine at 2 K and at 20 K. For further details about safety see Section 11.

9.8 Schedule and cost

The work plan to prepare the experimental area, the infrastructure and the services has been defined in collaboration with the CERN equipment and service groups. Windows for the preparatory works and the detector installation have been identified (LHC schedule version 3.1):

- 2021, mid-July and August: limited access possible for works to prepare the experimental area and infrastructure. LHC will be at operating conditions with helium and temperature at 2 K.
- 2021, October to December: Completion of works for the experimental area and services, followed by the installation of SND@LHC. LHC will be floating at temperature of 20 K.
- 2022, first week of January: installation of the emulsion bricks during the cryo recovery after the YETS.

Taking these periods into account, and minimising the amount of access underground in the first period, the groups have provided the amount of time required for each activity and their preliminary availability. A preliminary schedule for the works has been drawn up, shown in Figure 76. A preliminary schedule for the installation of the detector is also shown. More details are given in Section 14.2.

The CERN equipment and service groups have provided detailed cost estimates for each of the interventions to prepare the experimental area, the infrastructure and the services, shown in Table 11.

10 Commissioning

The commissioning of the active parts of the SND@LHC detector will be done in several steps:

1. Individual detector plane assembly and testing, present to August 2021. The SciFi, veto and muon detector planes will be assembled and tested by the respective institutes. This phase includes the verification that each component is fully functional and a calibration of the energy response. A prototype of the target wall will be built to test the installation on the supporting structure and the replacement of the emulsion bricks.

2. Commissioning on the surface, August–October 2021. The active components of the detector will be assembled on the surface, either at EPFL or CERN, and the full DAQ system will be operated with cosmic rays.

3. Installation and commissioning in the tunnel, October–December 2021. The system will be transferred to the tunnel and a verification that no component has been damaged will be performed. A second test of the full DAQ system will be performed to ensure that no data loss happens.

4. Emulsion installation, January 2022. This will happen right before the closure of the LHC machine.

11 Safety

The SND@LHC project is followed by the Project and Experiment Safety Support (PESS) of the HSE-OHS group. An HSE correspondent has been appointed to assess the environmental impact and safety related to mechanical, HVAC, fire, chemical and electrical aspects. The preliminary assessment has not identified any major safety implication aspects. Hence, no official safety clearance/authorization will need to be released by the HSE unit head before starting the works (see Ref. [91]). A first version of the Launch Safety Discussion form has been prepared. This will allow HSE to specify the project safety requirements based on the regulatory framework, concerning the list the applicable rules and standards to be followed for the mentioned safety domains. This will be followed by the preparation of the Safety File in time for the approval, together with the HSE correspondent and the appointed representative from the EP DSO office.

Item		Sub-total (kCHF)
Scaffolding		3.5
Cooling		30.5
Chillers	7.7	
Control and electrical	7.5	
Piping & accessories	7.5	
Insulated box	3.8	
Manpower	4.0	
Removal of ventilation duct		1.9
Power and lights		21.0
Emergency lights	0.0	
Distribution cabling	8.5	
220V sockets	0.0	
AUG	1.0	
Electrical box	1.5	
Normal lamps	1.5	
Power cable for 10kW	0.5	
Cable tray rerouting for the rail-hoist installation	3.0	
Electrical box over the foot bridge displacement	3.0	
Powering within SR1	2.0	
Cable tray raising		2.5
Optical fibres		28.1
Optical fibers installation (TI18-RE18)	14.0	
Blowing tube + its installation	8.5	
Fibre optics and blowing	5.5	
Pro rata per fibre RE18 to TI18	9.6	
Pro rata per fibre within SR1	1.8	
Possible hole in the wall in RE18	1.2	
Patch cord	1.0	
Cable within the surface building	0.5	
Transport and handling		25.1
QRL protection, short construction	4.0	
Tooling installation (QRL protection and rail)	5.0	
Rail eepos 3.5m	1.5	
Consumable (lifting rings and slings)	0.5	
Low trolley	0.5	
Manual hoist 250kg	0.4	
Manpower for de-installation and installation	8.2	
Handling studies	5.0	
Survey		20.0
CERN manpower	0.1 FTE	
Contactor manpower	10.0	
Budget for material	10.0	
Network infrastructure		9.0
Switches and routers	9.0	
Total		141.6

Table 11: Cost breakdown for the works to prepare the experimental area, infrastructure, and services.

12 Offline software and computing

The offline software framework, `sndsw`, is based on the FairRoot framework [92], and makes use of the experience gained with the FairShip software suite, developed within the SHiP collaboration. FairShip has been successfully used for determining signal yields and background rates for the SHiP experiment proposal, as well as in two advanced test-beam setups that measured the muon flux emerging from a thick, high-density target, and aimed at measuring the associated charm production induced by 400 GeV/c SPS protons [93, 76]. The reconstruction and analysis tools developed by the SHiP collaboration can be applied for the track reconstruction and analysis of emulsion data in the SND@LHC.

12.1 FLUKA simulation framework

The multipurpose Monte Carlo code FLUKA [94, 95, 96] is the reference tool at CERN to address machine protection aspects as well as the complementary radiation protection scope. It is regularly and extensively used to assist the operation and the upgrade of the whole accelerator chain, in particular the LHC (see for instance [97, 98, 99]). For these purposes, notable technical developments were made to automatise the construction of consistent geometry models of several hundred metres of accelerator portions [100, 101]. As a relevant example, Figure 49 shows a view of the right side of the ATLAS insertion, as implemented in FLUKA, from the experimental cavern up to the TI18 gallery, whose slope rises from the LHC level towards the SPS.

To simulate LHC proton–proton collisions, FLUKA uses the DPMJET code [66, 102] as event generator. The latter has been bench-marked against Run 1 physics data [66], including those of the forward detectors [103]. Moreover, an independent validation is provided by the Beam Loss Monitor (BLM) system, consisting of a few thousand ionisation chambers all along the 27 km LHC beam line. They provide online measurements of the energy released by the particle showers originating from beam losses and, in particular, as far as the experimental insertions are concerned, the regular collision debris.

Depending on the machine segment, BLMs are sensitive to different components of the pp collision products. Only a few high energy and forward angle particles, out of more than hundred generated on average in one inelastic collision (4 out of 150 at 13 TeV centre-of-mass energy[3]), do not impact the detector, managing to travel inside the beam vacuum chamber and reach the accelerator elements beyond the absorber at the interface between the cavern and the LHC tunnel, at about 20 m from the IP. They are mostly photons (from neutral pion decay), charged pions, protons and neutrons, together with a lower amount of kaons and antinucleons, and carry (on each side) about 70% of the projectile energy, while the energy fraction on the detector is less than $< 5\%$. As shown in Figure 50, the majority of the energetic charged pions (and kaons) are then captured by the magnetic field of the following 30 m long string of superconducting quadrupoles, which perform the beam squeezing, and deposit there 15% of the projectile energy. This is reflected by the local BLM pattern observed during physics fills, as remarkably well predicted by the FLUKA simulation [104].

At about 140 m from the centre of the ATLAS detector, a massive absorber, called TAN, incorporates the transition between one single central aperture, containing both circulating beams, and two separate symmetrical apertures, one per beam, such as to intercept in between

[3]Neutrinos are not included in the count.

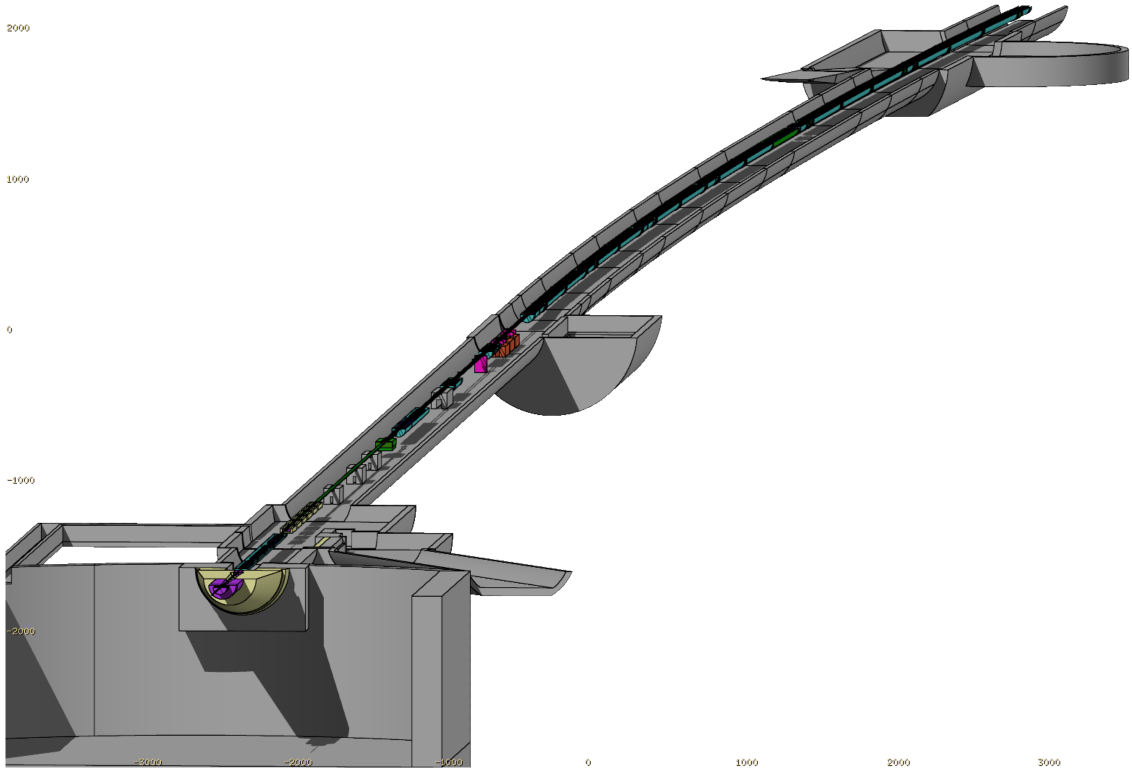

Figure 49: 3D view of the right side of the LHC Point 1 insertion, as modeled in FLUKA by the CERN FLUKA team. One can recognise the ATLAS detector forward shielding (bottom left), followed by the accelerator string along the straight section and the curved section, which starts with the Dispersion Suppressor at the location of the RR alcove (middle) and extends up to the first cell of the arc near the location of the TI18 gallery (top right). The geometry covers a length of about 500 m and includes, among others, detailed models of vacuum chambers, absorbents and magnets, provided with the respective field maps, such as to reproduce the beam trajectory with a micron accuracy.

the line of sight of neutral particles coming from the IP. Behind, a 9.5 m long superconducting twin bore recombination dipole opens to the so called Matching Section, which features four main superconducting quadrupole assemblies (numbered as Q4 to Q7) and ends at 270 m from the IP. Thanks to the TAN protection, only a few percents of the debris energy are absorbed in this region, concentrated in the three metallic horizontal collimators (TCLs) installed on the outgoing beam aperture to further shield the cold magnet coils. These collimators, depending on their operational gaps, become an important source of secondary particles locally increasing the radiation levels around the beam lines, as apparent in Figure 51, where the BLM pattern is reported, including this further machine segment. Here, it is ruled by neutral products and low rigidity protons from the original *pp* collisions, rather than charged pions as above. Once more, the simulation describes the effects with a quite good accuracy over more than four orders of magnitude, with a local overestimation in the region of the cell 5 collimator and after the Q7, where the signals become challengingly small.

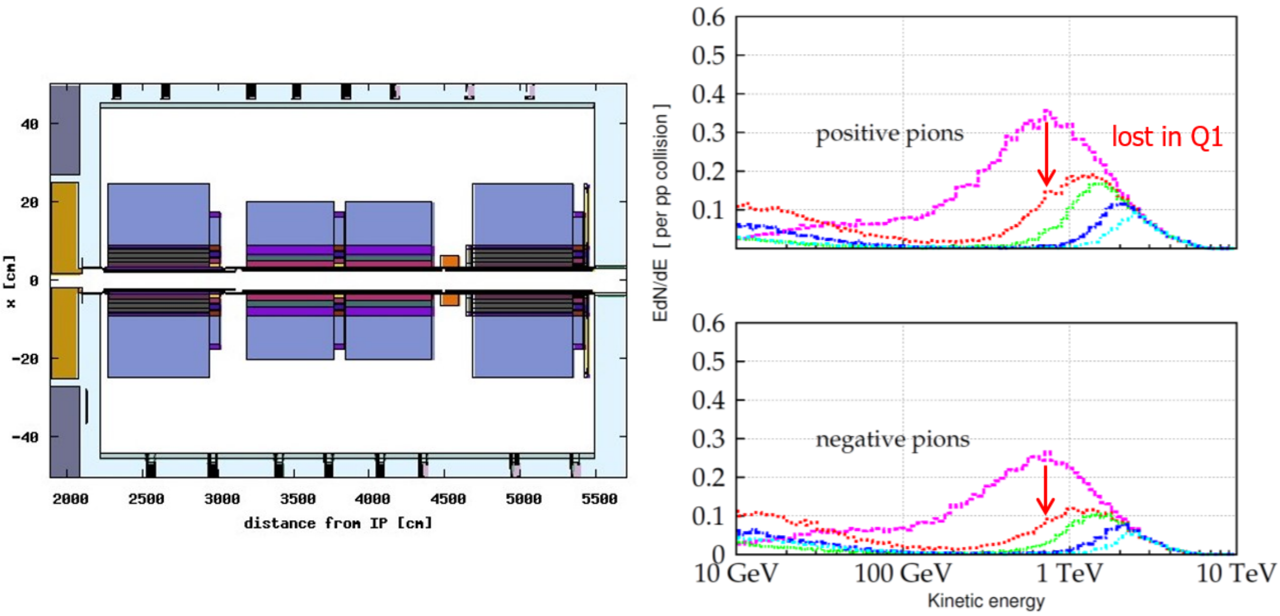

Figure 50: (Left) Final focus quadrupole string, including - from left to right - the main cold magnets Q1, Q2A, Q2B and Q3. Note the different axis scales. (Right) Charged pion spectra from 14 TeV centre-of-mass *pp* collisions at the entrance of Q1 (pink), Q2A (red), Q2B (green), Q3 (blue) and at the exit of Q3 (light blue). The progressive decrease in the 200 GeV to 2 TeV range indicates the pion loss due to the magnetic field capture, while the repopulation of the low energy tail is due to reinteraction products.

A third complementary region, where the simulation was probed by means of BLM measurements along a few hundred metres [105], is the so called Dispersion Suppressor, consisting of the half cells 8 to 11 that start bending the beam lines before reaching the arc. There, losses are induced by diffractive protons of energy slightly lower than the beam, representing another portion of the collision debris phase space.

The simulation framework outlined in this section was used to calculate the neutrino yields and spectra in TI18, as well as the muon population in the upstream rock at 75 m from SND@LHC. Moreover, it allowed estimating the local radiation levels due to the interactions of the counterclockwise beam with the residual gas in the vacuum chamber, expected to constitute the dominant term.

12.2 Detector simulation

Neutrino production in proton-proton collisions at the LHC is simulated with the FLUKA setup described above. DPMJET3 (Dual Parton Model, including charm) [106] is used for the event generation, and FLUKA performs the particle propagation towards the SND@LHC detector with the help of the FLUKA model of the LHC accelerator [97]. FLUKA also takes care of simulating the production of neutrinos from decays of long-lived products of the *pp* collisions and of particles produced in re-interactions with the surrounding material.

Genie [107] is then used to simulate neutrino interactions with the SND@LHC detector material. The output of Genie is given to Geant4 [108] for particle propagation in the detector.

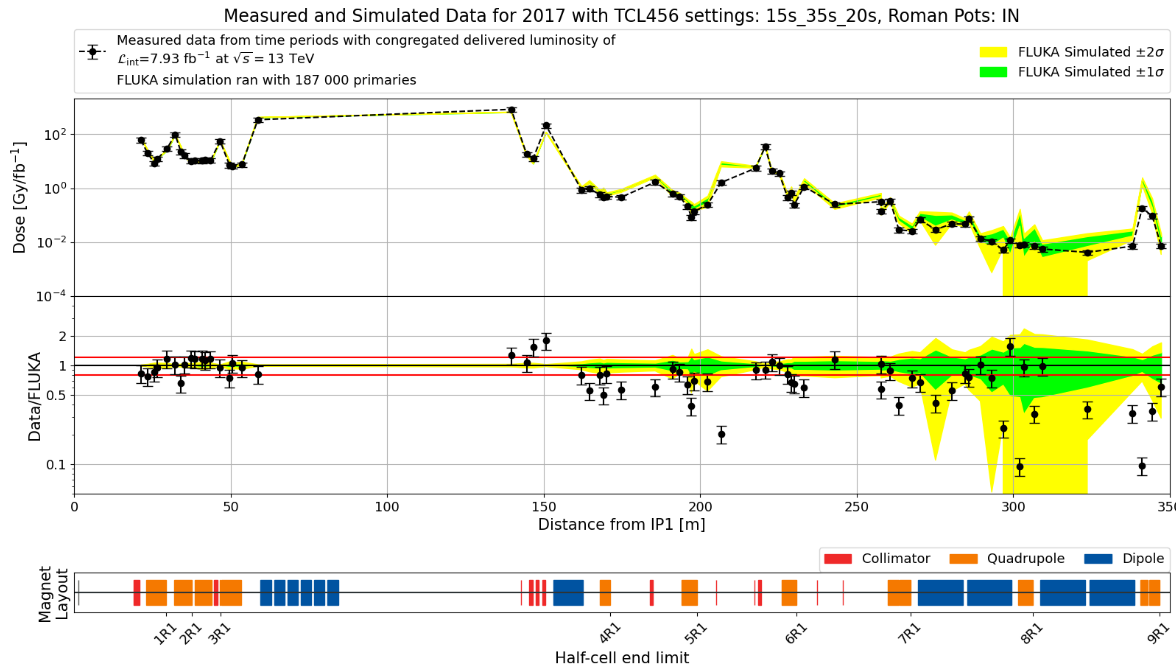

Figure 51: Top: BLM pattern on the right of ATLAS for *pp* collisions at 13 TeV center-of-mass energy, normalized to 1 fb^{-1}. For each monitor in the considered 330 m long region, black points give the dose as measured during 2017 LHC operation, while green and yellow bands are the $\pm 1\sigma$ and $\pm 2\sigma$ statistical uncertainty intervals, respectively, centered on the FLUKA simulation result. The three highest peaks between 100 m and 250 m correspond to the TAN, cell 4 and cell 6 collimator locations, respectively. Middle: Ratio between measurements and simulation, with the associated error bar. Red lines display the 20% discrepancy range. Bottom: Corresponding machine layout.

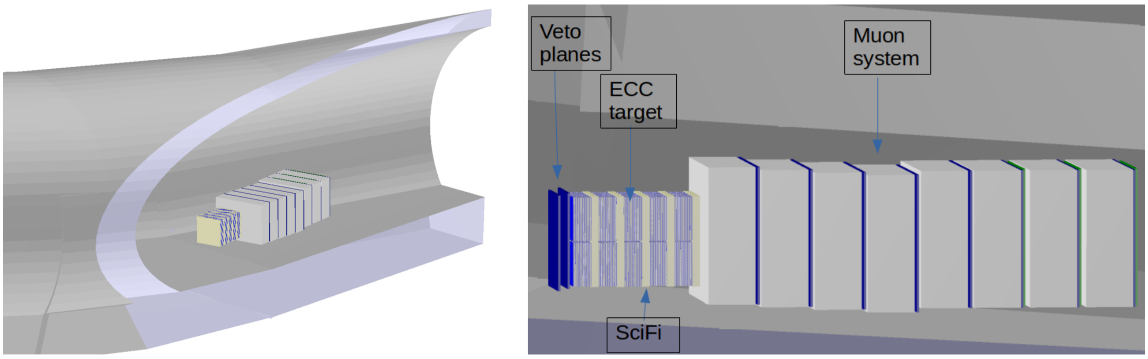

Figure 52: The SND@LHC detector implemented in the GEANT4 simulation with the tunnel geometry (Left) and standalone (Right).

A model of the detector and the surrounding tunnel has been implemented in GEANT4, as seen in Figure 52. The electronic detectors are implemented as sensitive volumes, with digitisation performed before the reconstruction to capture the physics of detector technologies. No mechanical supports besides the tunnel floor are included at this point.

A more accurate implementation in GEANT4 with finer segmentation—in particular for the SciFi detectors—is in development.

In addition to the simulation of neutrino interactions, the SND@LHC software framework provides interfaces to use particle guns, event generators including PYTHIA8 [109] and PYTHIA6 [110], as well as dedicated generators for specific backgrounds, in order to perform studies of various signals and backgrounds.

12.3 Data reconstruction

The event reconstruction is performed in two phases: the first one is performed during the data taking using the response of the electronic detectors. The second phase incorporates the emulsion data, that will be available about six months after the exposure.

The upstream veto planes will tag incoming muons that will be used for fine alignment between detector planes. The occurrence of a neutrino interaction or a FIP scattering will be first detected by the target tracker and the muon system. Electromagnetic showers are expected to be absorbed within the target region and will therefore be identified by the target tracker, while muons in the final state will be reconstructed by the muon system. In addition, the detector as a whole acts as a sampling calorimeter. The combination of data taken from both systems will be used to measure the hadronic and the electromagnetic energy of the event. A schematic representation of a ν_e and a ν_μ charged-current interaction in the SND@LHC detector is shown in Figure 53.

The reconstruction of the emulsion data begins during the scanning procedure. Optical microscopes (see Section 5.5) analyse the whole thickness of the emulsion, acquiring tomographic images at equally spaced depths. The acquired images are digitized, after which an image processor recognizes the grains as *clusters*, i.e. groups of pixels of a given size and shape. Thus, the track in the emulsion layer (usually referred to as *micro-track*) is obtained by connecting clusters belonging to different levels. Since an emulsion film is formed by two emulsion layers, the connection of the two micro-tracks through the plastic base provides a reconstruction of the particle's trajectory in the emulsion film, called *base-track*. The reconstruction of particle

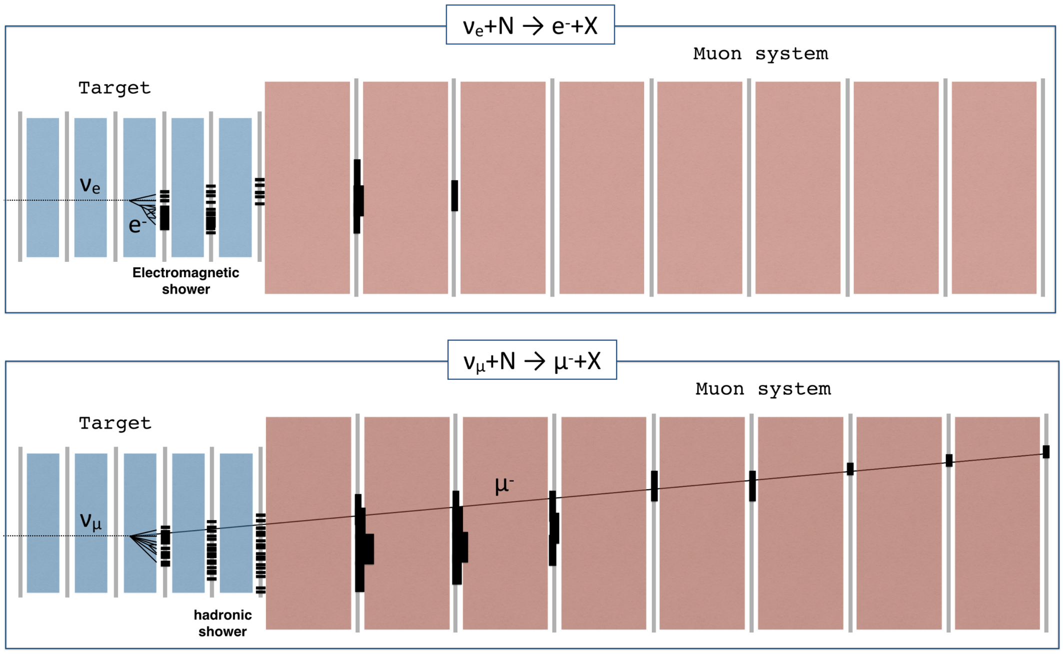

Figure 53: Schematic drawing of the reconstruction of a ν_e (top) and a ν_μ (bottom) charged-current interaction in the SND@LHC detector.

tracks in the full volume requires connecting base-tracks in consecutive films. In order to define a global reference system, a set of affine transformations has to be computed to account for the different reference frames used for data taken in different films. Muons coming from the IP will be used for fine film-to-film alignment. Once all emulsion films are aligned, *volume-tracks* (i.e., charged tracks which crossed several emulsion films) can be reconstructed. The off-line reconstruction tools currently used for track finding and vertex identification are based on the Kalman Filter algorithm and are developed in FEDRA (Frame-work for Emulsion Data Reconstruction and Analysis) [111], an object-oriented tool based on C++ and developed in the ROOT [112] framework.

12.3.1 Analysis tools

The SND@LHC Collaboration will use analysis tools that were recently developed for the SHiP-charm experiment [76], which aims at measuring the associated charm production induced by 400 GeV/c SPS protons. Although the signal and backgrounds expected at SND@LHC are different from those of the SHiP-charm measurement, the two projects share the same challenging task of identifying interactions in an unprecedented flux of charged particles.

Similar to the proposed SND@LHC detector, the SHiP-charm setup for the test run at the H4 beamline at the CERN SPS in July 2018 also included a hybrid system, combining the Emulsion Cloud Chamber technique with electronically read out detectors. The test run collected data from about 1.5×10^6 protons on target. The large number of hadronic re-interactions and electromagnetic showers in the emulsion brick resulted in an unprecedented number of reconstructed vertices in the target volume. The track density in a single emulsion film reached up to $5{\times}10^4\,/\mathrm{cm}^2$. The successful use of the newly developed analysis tools demonstrated that it is possible to reconstruct the proton interaction vertices in an environment in which the signal is largely dominated by secondary particles. A good agreement between data and the expectation from Monte Carlo was found for the number of charged tracks defining the interaction vertex and the distribution of vertices along the beam axis [113]. The development of a Monte Carlo simulation that accurately described the reconstructed data and the application of multivariate analysis techniques allowed to extract the primary proton interaction component in a ∼365 mm long emulsion/lead target and to evaluate the effective interaction length, which is in good agreement with expectations. The results prove that the emulsion analysis tools are mature enough to be applied in the analysis of the SND@LHC data. In addition, a new approach for event reconstruction in emulsion detectors based on machine learning techniques is being developed. The topologies of some signal events that can be reconstructed in the SND@LHC brick are illustrated in Figure 54.

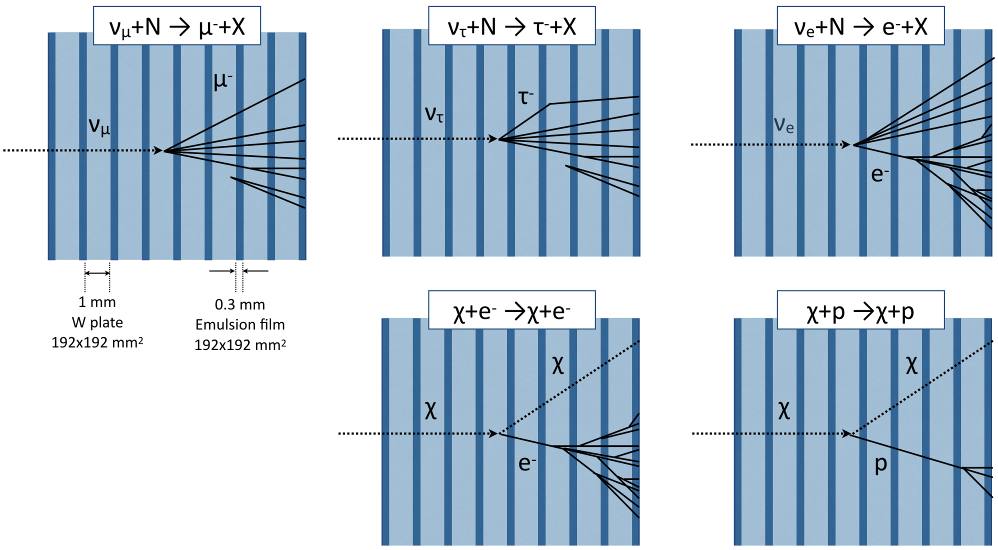

Figure 54: Illustration of some of the signal topologies that can be reconstructed in the SND@LHC brick.

We expect on average twelve neutrino interactions in each brick per run. The matching with the adjacent target tracker plane will be performed by aligning the centre-of-gravity of events reconstructed in the two detectors, thus giving timing information to interactions reconstructed in the brick. The emulsion data will be also used to complement the target tracker system for the energy measurement of electromagnetic showers.

12.4 Performance studies

12.4.1 Neutrino detection

For the data analysis, a fiducial volume inside the brick is defined, excluding the regions within 5 mm of the downstream edge and 1 mm from the lateral side. This results in a geometrical efficiency ϵ_{geom} of approximately 89.3%. The identification of a neutrino interaction requires two visible tracks in emulsion, one of which must have a momentum larger than 1 GeV/c, to form a primary vertex. The visibility criteria are listed in Table 12. Monte Carlo simulation studies, fully validated with data from the SHiP-charm measurement, have shown that the efficiency of finding the vertices for the different neutrino flavours is above 90%.

Particle	Visibility cut p [MeV/c]
charged	> 100
p	> 170
π^0	> 400
γ	> 200

Table 12: Visibility cuts on the momentum of primary tracks at the neutrino interaction vertex.

Muon identification Muon identification is relevant for both identifying ν_μ and ν_τ interactions. Charmed hadrons produced in ν_μ CC interactions constitute a background for the ν_τ search, if the primary muon is not identified.

Monte Carlo studies have shown that $\sim 98.4\%$ of the muons produced in ν_μ CC interactions enter the muon system. Out of them, $\sim 91.5\%$ leave a hit in the last three planes of the muon identification system and can thus be identified. The current algorithm is based on the tracks reconstructed in the emulsions at the neutrino interaction. Each emulsion track is projected onto the last three muon detector planes, comprising both horizontal and vertical bars to provide x-y coordinates. The corresponding x-y bars hit by the projected track on each of the three planes are identified. The primary track is considered found on a given plane if there is a corresponding hit in the bars matching the projected track, or in the adjacent bars. Isolation of the track is determined by requiring no hits in the bars adjacent to the search window.

A muon candidate is selected according to the following criteria:

- A corresponding track is found on all of the three most downstream muon detector planes.
- The track is isolated in at least two of the three planes.

The above selection results in a muon identification efficiency of about 77% for charged current ν_μ interactions. Accounting also for the geometrical acceptance described above, the overall muon identification efficiency is $\sim$69% for ν_μ CC. The probability of misidentifying a primary hadron track as a muon was studied using neutral current (NC) ν_μ interactions, and is found to be less than 0.36%. Having on average five charged hadron tracks per event, implies a purity in muon identification of almost 99%.

Table 13 shows the event classification for CC and NC muon neutrino interactions. 0μ events are those without any muon reconstructed in the final state. Events with one or more muons reconstructed are labelled as 1μ or $n\mu$ events. As it can be seen, 69% of the CC interactions show at least one reconstructed muon while the probability for a NC interaction to be properly classified as 0μ is above 99%.

Electron identification Electrons produced by neutrino scattering are identified by the observation of an electromagnetic shower induced inside the interaction brick.

Electromagnetic showers originating from photons are distinguished from those initiated by electrons thanks to the micrometric accuracy of the nuclear emulsion that is capable of observing the displaced vertex associated with the photon conversion. This procedure is characterized by an efficiency larger than 95%.

The target tracker will complement the emulsion detector in the identification of electromagnetic showers and in the electron/π^0 separation, thus achieving an efficiency of about 99%.

	% evts CC-DIS	% evts NC-DIS
0μ	31.1	99.6
1μ	67.6	0.27
2μ	1.13	0.06
3μ	0.1	0.03
$> 3\mu$	0.01	0

Table 13: Event classification for CC and NC interactions.

decay channel	$\epsilon_{\rm ds}$ (%)	$\epsilon_{\rm tot}$ (%)
$\tau \to \mu$	82.5 ± 1.6	49.6 ± 1.8
$\tau \to e$	80.8 ± 1.7	48.4 ± 1.8
$\tau \to h$	80.3 ± 1.0	48.4 ± 1.1
$\tau \to 3h$	89.4 ± 1.5	54.0 ± 1.9

Table 14: Decay search and overall efficiencies for the different τ decay channels.

Tau identification The identification of τ lepton candidates is based on purely topological criteria. Once the primary neutrino interaction vertex has been identified, secondary vertices, signs of possible short lived particle decays, are searched for. This is done by a dedicated decay search procedure. Tracks are defined as belonging to a secondary vertex if the impact parameter of the daughter track with respect to the primary vertex is larger than 10 µm. The fraction of events in which the tau lepton decays before the last five emulsion plates is: $\epsilon_{\tau \rm length} = 74.8 \pm 0.7\%$.

The decay search efficiency $\epsilon_{\rm ds}$ ranges from 80% to 89% for the different channels, as summarised in Table 14. The total efficiency $\epsilon_{\rm tot}$, also reported in Table 14, is the combination of the geometrical, primary vertex identification, and decay search efficiencies: $\epsilon_{\rm tot} = \epsilon_{\rm geom} \cdot \epsilon_{\rm loc} \cdot \epsilon_{\tau \rm length} \cdot \epsilon_{\rm ds}$ and ranges from 48.4% in the $\tau \to h$ decay channel up to 54% in the $\tau \to 3h$ decay channel.

12.4.2 Neutrino energy measurement

We exploit the information of the electronic detectors in both the target region and in the muon identification system. Indeed, the whole detector can be considered as a non-homogeneous calorimeter. The energy of the particle shower can be reconstructed using the hits on the SciFi planes either by simple counting or via a more refined algorithm using machine learning, currently under development. With the counting method, the energy of the electromagnetic and the hadronic component of the neutrino interaction can be reconstructed as:

$$E^{\rm rec}_{\rm had} = A + B \times N_{\rm SciFi} + C \times N_{\rm MuFilter} \tag{1}$$

The values of parameters A, B and C, in units of GeV, are obtained by a gradient descent minimisation algorithm applied to simulated events, with the following cost function:

$$J(A,B,C) = \frac{1}{2m}\sum_{i=1}^{m}\left(E_{\mathrm{had}}^{\mathrm{rec}\,(i)} - E_{\mathrm{had}}^{\mathrm{true}\,(i)}\right)^2 \tag{2}$$

where m is the number of events. The best-fit parameter values are: $A = 1.0\,\mathrm{GeV}$, $B = 0.22\,\mathrm{GeV}$, $C = 0.44\,\mathrm{GeV}$. The resolution on the reconstructed energy is reported in Figure 55. The overall fractional resolution is $(22.3 \pm 0.6)\%$.

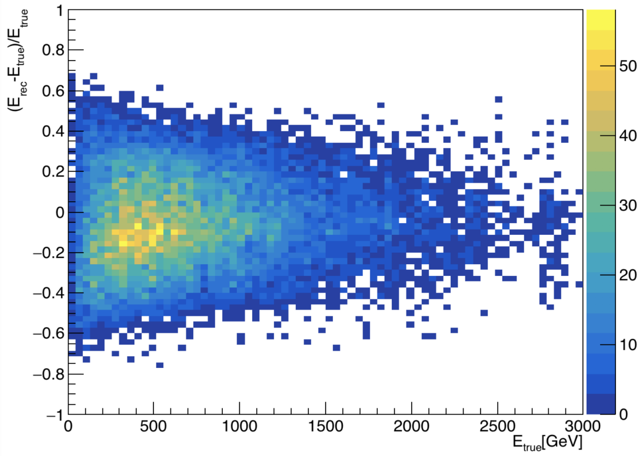

Figure 55: $\Delta E/E$ distribution of the reconstructed energy as a function of the neutrino energy, using the counting method.

As far as ν_e and ν_τ are concerned, the reconstructed energy corresponds to the neutrino energy (except for $\nu_\tau \to \mu$ decay channel). For ν_μ ($\bar{\nu}_\mu$) charged-current interactions, the momentum of the outgoing muon can be estimated by balancing the transverse momentum of the hadronic system. Dedicated algorithms based on multivariate techniques will be used to extract the neutrino energy.

Another energy reconstruction technique using convolutional neural networks (CNN) is being developed. Very encouraging preliminary results have already been achieved [114, 115, 116]. A CNN had previously been trained on (x, y) simulated hit coordinates from the target tracker detector planes of the SND detector in two configurations: a smaller 6-layers detector of 12 cm transverse dimensions as a simplified case study, and a full-size 4-layers tracker corresponding to a possible SND pilot run configuration. For the second dataset, a preprocessing routine has been developed, aimed at extrapolating the shower position and direction from the centre of gravity of the layers containing the most hits, and at reducing the CNN input to a window containing 99.9% of the hits[114]. In both cases, the CNN exhibits a fractional resolution of about 5% at $E = 100\,\mathrm{GeV}$, and a first analysis of the detector response demonstrates that the target tracker planes behave as a sampling calorimeter, as seen in Figure 56, according to the usual formula

$$\frac{\sigma_E}{E} = \sqrt{\left(\frac{a}{\sqrt{E}}\right)^2 + \left(\frac{b}{E}\right)^2 + c^2}$$

with stochastic term $a = 0.665 \pm 0.002\,\mathrm{GeV}^{1/2}$ and calibration term $c = 0.014 \pm 0.004$, where the noise term is absent in simulation [114]. Further work and a larger data set with higher energy neutrinos will refine this result. A thorough study proved that the energy predicted by the CNN is unbiased [115].

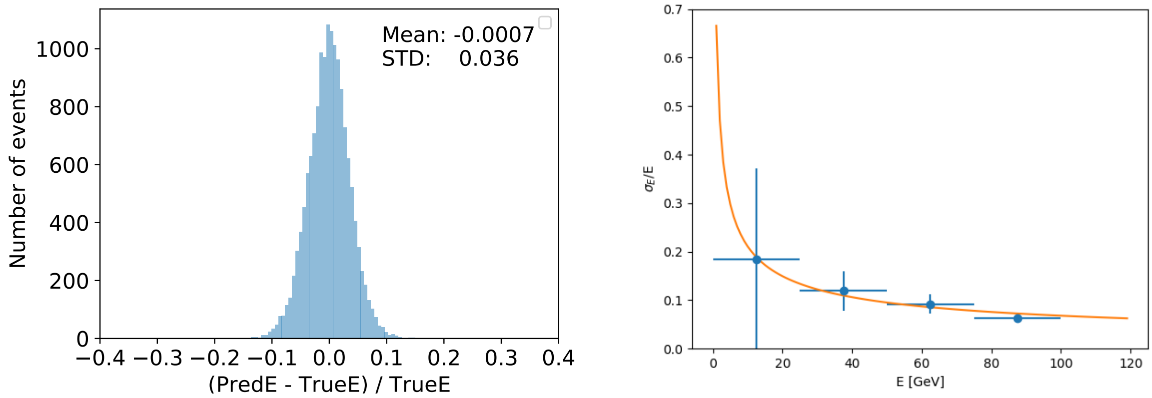

Figure 56: Electron energy reconstruction using a CNN trained on (x, y) simulated hit coordinates on the target tracker planes [114, 116]. (Left) Fractional energy difference as obtained from a CNN trained on $200 - 400\,\mathrm{GeV}$ particle showers [116]. (Right) Performance of the target tracker as sampling calorimeter on a $0.3 - 100\,\mathrm{GeV}$ subset of the data sample (studies are ongoing on higher energy neutrinos) [114].

A new CNN was developed in order to take into account the presence of ghost hits. This time, the architecture of the CNN was changed in order to use only the (x, z) and (y, z) projections of the simulated hits on the target tracker induced by the particle shower. This totally eliminates the problem of the ghost hits, which are generated by incorrect random combinations of x and y target tracker channels. This new architecture exhibits an average fractional energy resolution of 5.7% [115], as shown in Figure 57.

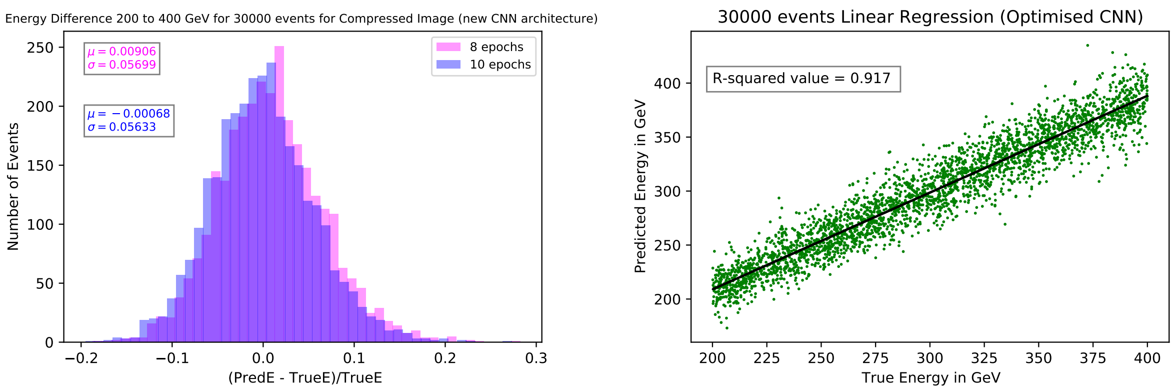

Figure 57: Electron energy reconstruction using a modified CNN trained on (x, z) and (y, z) simulated TT hit coordinates, for $200 - 400\,\mathrm{GeV}$ electrons [115]. (Left) Fractional energy difference. (Right) Predicted energy versus true energy.

Finally, the spatial distribution of hits on the target tracker planes can be used as a simple way of discriminating between elastic and inelastic scattering events. Two datasets have been produced with Genie, using the NuEElastic and CCDIS setting, respectively. The CNN used for the first study was modified to provide output label probabilities rather than a predicted energy value, and it was trained on the two datasets. The prediction accuracy was found to be 94.5% [116], as shown in Figure 58.

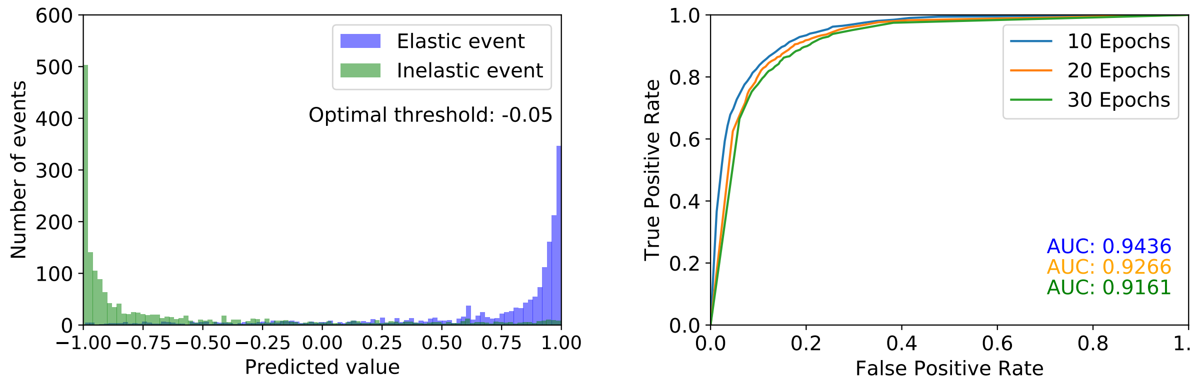

Figure 58: Classification of elastic versus inelastic scattering events using a CNN trained on the true simulated (x, y) hit coordinates for $100 - 5000\,\mathrm{GeV}$ neutrinos [115]. (Left) Predicted labels (-1 for inelastic scattering and +1 for elastic scattering) for events in the test dataset. (Right) True positive rate versus false positive rate.

12.5 Software and computing infrastructure

SND@LHC requires only a very modest computing infrastructure.

The offline software is developed, maintained, and distributed on Github. `sndsw` and its dependencies are built from source and are configured using the AliBuild tool, developed by ALICE for their upgrade software. The recipes for the dependencies are shared with ALICE and SHiP, where possible, to reduce the maintenance of the framework. Specific patches and recipes for software uniquely used by SND@LHC are added, where required.

Container images with the dependencies as well as an installation on the CVMFS are provided for various use cases.

Raw data will be archived on tape. Raw and reconstructed data will be made available on EOS for analysis.

12.6 Cost and schedule

The offline software development has started with a prototype implementation of the detector layout. Work to add more details is ongoing. The raw data format, channel numbering and matching to coordinates is under development. This will allow to generate realistic data for exercising the reconstruction tools. A Track Fitter will be implemented using the GENFIT package [117], which has been successfully used by SHiP. The integration with the emulsion data will follow the procedure developed for the SHiP-charm measurement.

Conditions data and associated tools for calibration, alignment, and data monitoring will be developed during 2021. The detector commissioning on the surface will be the first milestone.

The requirements in terms of data storage and computing are moderate and comparable with the requirements for FASER:

- 70 terabyte (TB) of real data per year on tape media;
- 0.6 PB of disk space for raw data, from electronic detectors (100 TB), reconstructed segments from the emulsion scanning (200 TB) and Monte Carlo (300 TB);
- 1 TB of disk space on CVMFS for software deployment;
- Home directories for users and project space for central datasets (ntuples);
- On-demand databases for bookkeeping and metadata;
- 1000 CPU cores for processing, simulation and analysis (equivalent to 1000 concurrent running jobs);

The corresponding computing operations cost is estimated to 60 kCHF over the lifetime of the experiment (2021-2026).

13 Physics performances

13.1 Neutrino physics

The SND@LHC detector target covers a pseudo-rapidity range between $7.2 < \eta < 8.6$. The neutrino yield in the SND@LHC acceptance for the three different neutrino flavours is reported in Table 15, assuming 150 fb^{-1} integrated luminosity for p–p collisions at 13 TeV, together with the expected number of charged-current and neutral-current neutrino interactions occurring in the detector target. Energy spectra for CC DIS interactions are shown in Figure 59. Tungsten plates of type II (see Table 3) are assumed as passive material, for a total target mass of 830 kg. A 150 μrad upward crossing angle is assumed. In the opposite configuration the expected number of interactions will be reduced by about 40%: an overall 20% reduction is thus expected if they are run with equal weights. This does not change any of the conclusions reached in this Chapter.

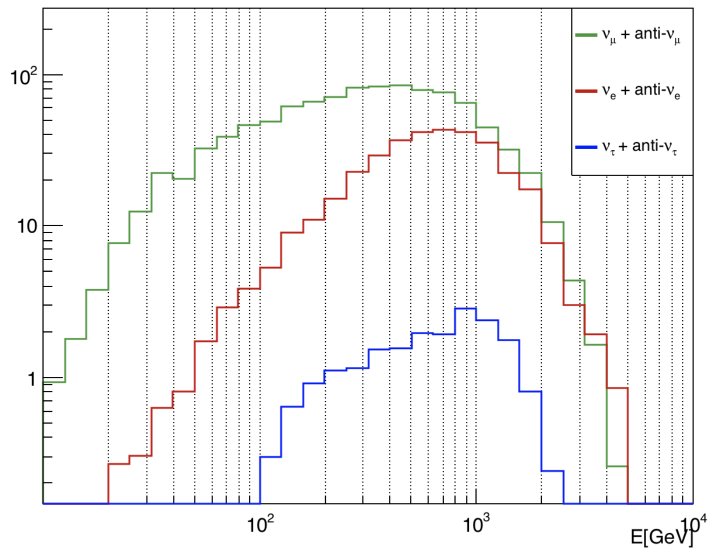

Figure 59: Energy spectra of the different types of CC DIS interacting neutrinos. The normalisation corresponds to 150 fb^{-1}.

13.1.1 Charmed-hadron production in *pp* collisions

Electron neutrinos and anti-neutrinos interacting in SND@LHC mainly come from the decay of charmed hadrons produced in the LHC *pp* collisions. The measurement of their flux in the acceptance of the experiment can therefore provide insight into the heavy-quark production in an unexplored domain.

The yield of charmed hadrons producing neutrinos in the SND@LHC pseudo-rapidity range is estimated in a two-step analysis: (*i*) measurement of the $pp \to \nu_e X$ cross-section, (*ii*) derivation of the charmed-hadron yield from the ν_e flux.

The first step relies on the response matrix estimated with the `sndsw` simulation, as described in Section 12. The correlation between measured and true energy is shown in the left panel of Figure 60. It includes resolution effects that depend on the neutrino energy and on the

Flavour	Neutrinos in acceptance ⟨E⟩ [GeV]	Yield	CC neutrino interactions ⟨E⟩ [GeV]	Yield	NC neutrino interactions ⟨E⟩ [GeV]	Yield
ν_μ	145	2.1×10^{12}	450	730	480	220
$\bar{\nu}_\mu$	145	1.8×10^{12}	485	290	480	110
ν_e	395	2.6×10^{11}	760	235	720	70
$\bar{\nu}_e$	405	2.8×10^{11}	680	120	720	44
ν_τ	415	1.5×10^{10}	740	14	740	4
$\bar{\nu}_\tau$	380	1.7×10^{10}	740	6	740	2
TOT		4.5×10^{12}		1395		450

Table 15: Number of neutrinos in the SND@LHC acceptance, charged-current and neutral-current neutrino interactions in the detector target, assuming 150 fb^{-1}. Average energies are also reported.

primary electron identification efficiency. After having generated the outcome of a pseudo-experiment that observes the expected number of ν_e and $\overline{\nu}_e$, an unfolding procedure is applied in order to extract the reconstructed energy spectrum, free from resolution and reconstruction efficiency effects. The `RooUnfold` class based on the Iterative Bayes Theorem [118] is used for this purpose. The result is shown in the right panel of Figure 60, where the reconstructed energy spectrum after the application of the unfolding procedure is compared with the true energy spectrum.

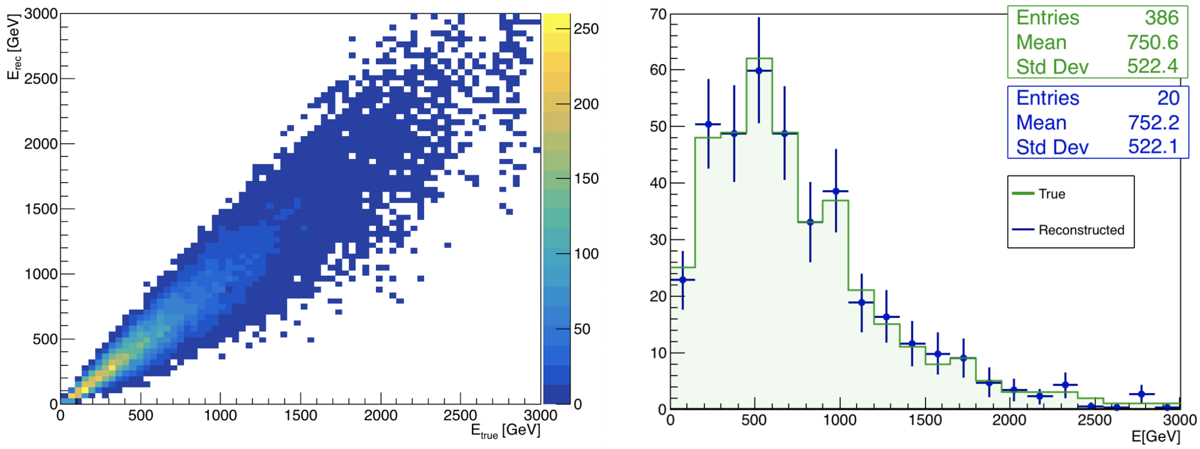

Figure 60: (Left) Response matrix for the reconstructed ν_e energy. (Right) Reconstructed energy spectrum after the application of the unfolding procedure (blue points) compared with the true energy spectrum (green histogram).

The error bars include both the statistical errors and the systematic uncertainties related to the unfolding procedure. Assuming the SM predictions for ν_e and $\overline{\nu}_e$ charged-current cross-sections, it is therefore possible to extract the energy spectrum and the total yield of electron neutrinos produced in the LHC pp interactions in the pseudo-rapidity range of $7.2 < \eta < 8.6$, as shown in the left panel of Figure 61. At this stage, the overall uncertainty on the inclusive measurement of the $pp \to \nu_e X$ cross-section amounts to 15%, dominated by the systematic

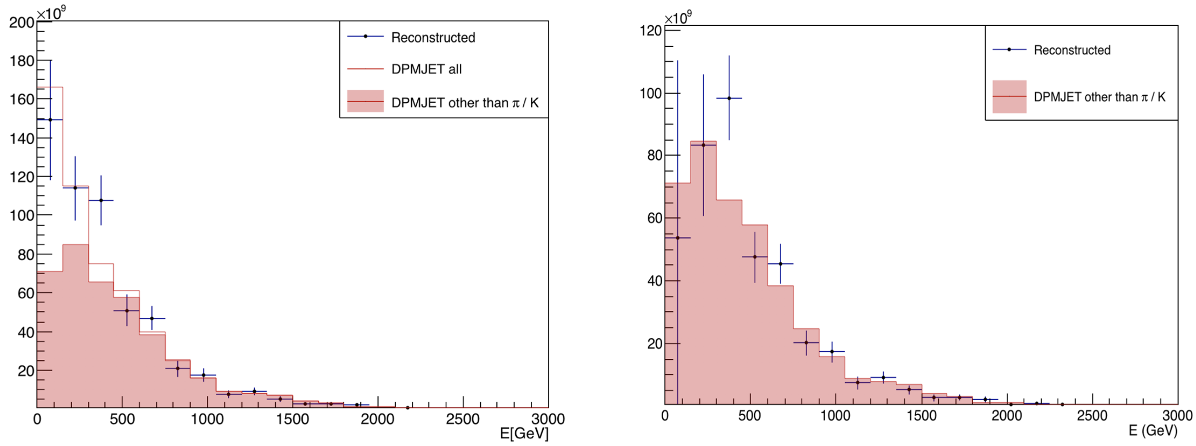

Figure 61: Reconstructed energy spectrum of ν_e and $\overline{\nu}_e$ in the SND@LHC acceptance (blue points) compared with expectations from simulation (red histogram), before (left) and after (right) the subtraction of the K component. The component from heavy-quark decay is reported as dark filled histogram.

error introduced by the unfolding procedure, given the 5% statistical accuracy.

In order to estimate the number of electron neutrinos and anti-neutrinos from charmed-hadron decay $N(\nu_e + \overline{\nu}_e)^{\mathrm{charm}}$, a statistical subtraction of the kaon component has to be performed. The predictions from different generators show large differences in the yield of ν_e and $\overline{\nu}_e$ produced in kaon decays [3]. However, this component is restricted to the low energy part of the spectrum ($E < 200$ GeV), where the number of observed neutrino interactions is lower due to the lower interaction cross-section. Therefore, the subtraction of the kaon component only has an effect in the first energy bins of the spectrum and introduces an additional 20% uncertainty to $N(\nu_e + \overline{\nu}_e)^{\mathrm{charm}}$, as shown in the right panel of Figure 61. Note that in the current classification neutrinos from the sequential decay $D \to K \to \nu_e$ are counted as from K. However, this contribution was estimated to be about 1.5% of the total kaon component, therefore its effect is negligible.

The second step takes into account the geometrical acceptance of the SND@LHC detector for the different charmed hadron species decaying into $\nu_e/\overline{\nu}_e$. A simulation with POWHEG [119, 120, 121] and PYTHIA8 [109] was performed in order to study the correlation between the electron neutrino and the parent charmed hadron. Figure 62 shows the correlation in energy and pseudo-rapidity between the two particles. Here we focus on the angular correlation. Later, energy information will also be exploited to further improve the analysis.

As it can be inferred from the right figure, neutrinos in the SND@LHC acceptance come from charmed hadrons either laying in the same pseudo-rapidity or having smaller/larger η. The migration was studied in three cases, by defining regions in the pseudo-rapidity correlation plot, as reported in Figure 63, and evaluating the following quantities:

CASE I ($7.2 < \eta_{\mathrm{hadron}} < 8.6$)

- $f_{AB} = N_A/N_{A+B}$
  fraction of electron neutrinos in the pseudo-rapidity range $7.2 < \eta < 8.6$ that come from charmed hadrons in the same range

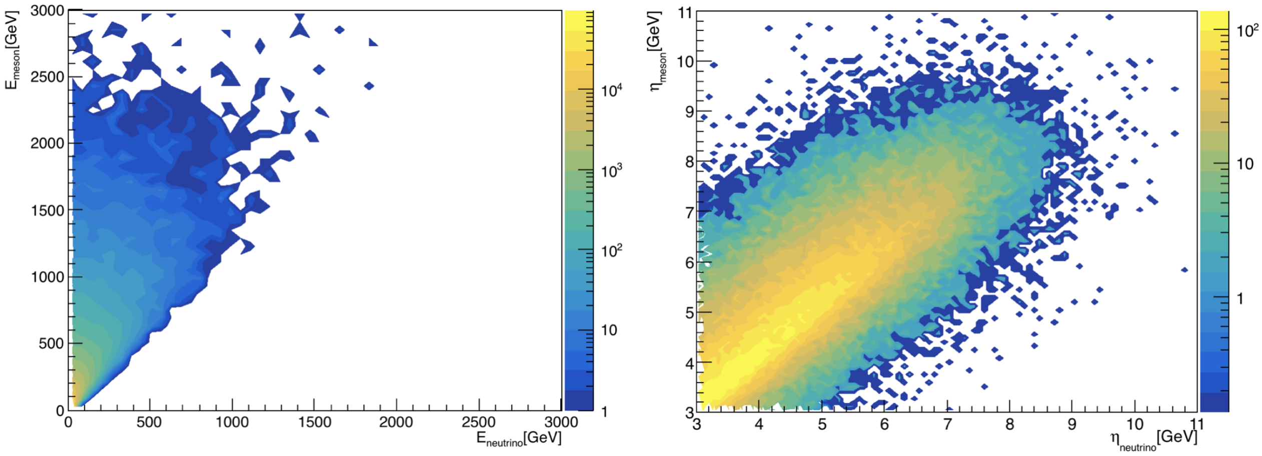

Figure 62: Correlation in energy (left) and pseudo-rapidity (right) between the electron neutrino and the charmed hadron.

- $f_{AC} = N_A/N_{A+C}$
  fraction of charmed hadrons in the pseudo-rapidity range $7.2 < \eta < 8.6$ that produce neutrinos in the same range

CASE II ($\eta_{\text{hadron}} > 7.2$)

- $f_{AB} = N_A/N_{A+B}$
  fraction of electron neutrinos in the pseudo-rapidity range $7.2 < \eta < 8.6$ that come from charmed hadrons with $\eta > 7.2$

- $f_{AC} = N_A/N_{A+C}$
  fraction of charmed hadrons with $\eta > 7.2$ that produce neutrinos in the pseudo-rapidity range $7.2 < \eta < 8.6$

CASE III ($\eta_{\text{hadron}} > 5$)

- $f_{AC} = N_A/N_{A+C}$
  fraction of charmed hadrons with $\eta > 5$ that produce neutrinos in the pseudo-rapidity range $7.2 < \eta < 8.6$

The default event generation has been performed with POWHEG+PYTHIA8.2 using the HVQ generator at leading order and the NNPDF30_NLO_AS_118 [122] PDF set. The error was evaluated by studying the fluctuations when the parameters that describe charm production are varied. Furthermore, we estimated the impact of non-perturbative corrections by varying the value of the primordial kT in PYTHIA6. In particular, the following parameters were changed:

- charm quark mass:
  $m_c = 1.25,\ 1.5$ (default) and $1.65\,\text{GeV}/c^2$

- scale factor $\hat{\mu}$:
  Factorisation and renormalisation scales are set equal to each other according to $\mu_F = \mu_R = \hat{\mu}\mu_0$. The reference scale is chosen to be $\mu_0 = \sqrt{m_c^2 + p_T^2}$ and the variations correspond to $\hat{\mu} = 0.5, 1\,(\text{default}), 2$

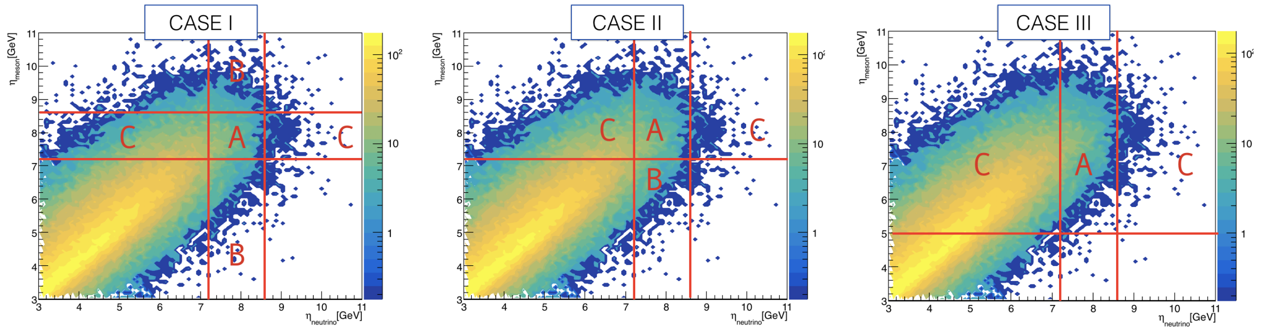

Figure 63: Correlation between the pseudo-rapidities of the electron neutrino and the charmed hadron. Horizontal and vertical bands define regions used in the three analysis cases.

- primordial kT (in PYTHIA6):
  Intrinsic transverse momenta of the incoming partons modelled as a gaussian smearing with width equal to 0.5, 1.0, 1.5, 2.0 and 2.5 GeV.

To study the impact of shower and hadronisation modelling we computed the same quantities also using HERWIG7. As last variation, we performed the computation also using a different set of PDFs, MMHT2014NLO68CLAS118 [123], in order to test possible dependencies.

Values of f_{AB} and f_{AC} for each variation are reported in Table 16. Results show that the migration in pseudo-rapidity between charmed hadrons and electron neutrinos is stable within 25-30% in the three cases, even if there are significant changes in the total rates of charm production and in the subsequent hadronisation.

The number of charmed hadrons $N(c\text{−hadron})$ can be estimated as

$$\text{CASE I,II} \quad N(c\text{−hadron}) = N(\nu_e + \overline{\nu}_e)^{\text{charm}} \times \frac{f_{AB}}{f_{AC}} \times \frac{1}{Br(c \to \nu_e)}$$

$$\text{CASE III} \quad N(c\text{−hadron}) = N(\nu_e + \overline{\nu}_e)^{\text{charm}} \times \frac{1}{f_{AC}} \times \frac{1}{Br(c \to \nu_e)}$$

where $Br(c \to \nu_e X)$ is the branching ratio of charmed hadrons to electron neutrino.

The relative uncertainty on the charmed-hadron yield has therefore two contributions: the first one on the number of ν_e and $\overline{\nu}_e$ in acceptance coming from charmed-hadron decays, amounting to 25%, given by the squared sum of the 15% and 20% uncertainties mentioned above, and the second one on the migration ratio (f_{AB}/f_{AC} or $1/f_{AC}$), as reported in Table 17.

Furthermore, the measurement of the charmed hadrons can be translated into a measurement of the corresponding open charm production in the same rapidity window given the straight correlation between the parent charm quark and the hadron, as shown in Figure 64. The dominant partonic process for associated charm production at the LHC is gluon-gluon scattering. The preliminary plot, shown in Figure 65, of the correlation between the x_1 and x_2 momentum fractions of the interacting gluons probed by SND@LHC indicates that the average lowest momentum fraction is around 10^{-6}. At such low values of x the gluon PDF is totally unknown. Moreover, it is well known that the prediction of the observables that are sensitive to very low x could receive relevant contributions from resummation. Unfortunately not all theoretical ingredients to compute resummed cross-sections for heavy-quark production are

		CASE I		CASE II		CASE III
Parameter	value	f_{AB}	f_{AC}	f_{AB}	f_{AC}	f_{AC}
all	default	0.51	0.21	0.66	0.21	0.058
m_c [GeV/c^2]	$(1.25, 1.65)$	$(0.54, 0.50)$	$(0.22, 0.21)$	$(0.74, 0.62)$	$(0.25, 0.23)$	$(0.074, 0.052)$
$\hat{\mu}$	$(0.5, 2.0)$	$(0.54, 0.50)$	$(0.23, 0.25)$	$(0.73, 0.61)$	$(0.25, 0.21)$	$(0.081, 0.048)$
`primordialKT`	$(0.5 - 2.5)$	$(0.54, 0.51)$	$(0.21, 0.25)$	$(0.72, 0.63)$	$(0.24, 0.26)$	$(0.067, 0.060)$
HERWIG7	default	0.45	0.23	0.74	0.28	0.076
MMHT2014	default	0.54	0.22	0.70	0.24	0.072
		f_{AB}/f_{AC}=$2.4^{+0.1}_{-0.5}$		f_{AB}/f_{AC}=$3.1^{+0.0}_{-0.7}$		$1/f_{AC}$=17^{+4}_{-5}

Table 16: Values of f_{AB} and f_{AC} fractions for different values of the parameters that describe charm production and hadronisation in the three analysis cases.

	CASE I	CASE II	CASE III
Stat. (%)	5	5	5
Sys. (%) Unfolding and kaon subtraction	25	25	25
Sys. (%) ν-charmed hadron correlation	$^{+4}_{-21}$	$^{+0}_{-23}$	$^{+24}_{-29}$

Table 17: Statistical and systematic errors on the charmed-hadron yield in the three different η regions.

currently known. Nevertheless the extraction of the gluon PDF in the very-small-x region performed with available tools could provide valuable information for other experiments probing the same low x range and for the future implementation of the resummation program.

To constrain the PDF by exploiting data from charm production in the very forward region, one can adopt a strategy similar to what has been done in Ref. [124], building a ratio between the cross-section measurements at different energies and pseudo-rapidities. In the left panel of Figure 66 we show the differential cross-section for charm production up to $\eta = 8$, while for illustrative purposes, in the right panel we show the ratio

$$R = \frac{d\sigma/d\eta(13\,TeV)}{d\sigma/d\eta_{ref}(7\,TeV)}$$

where the pseudo-rapidity range of the reference cross-section is $4 < \eta < 4.5$. From these figures one observes that the normalisation with respect to the 7 TeV cross-section lead to a reduction of the scale uncertainty and then to the possibility to constrain the PDF with data.

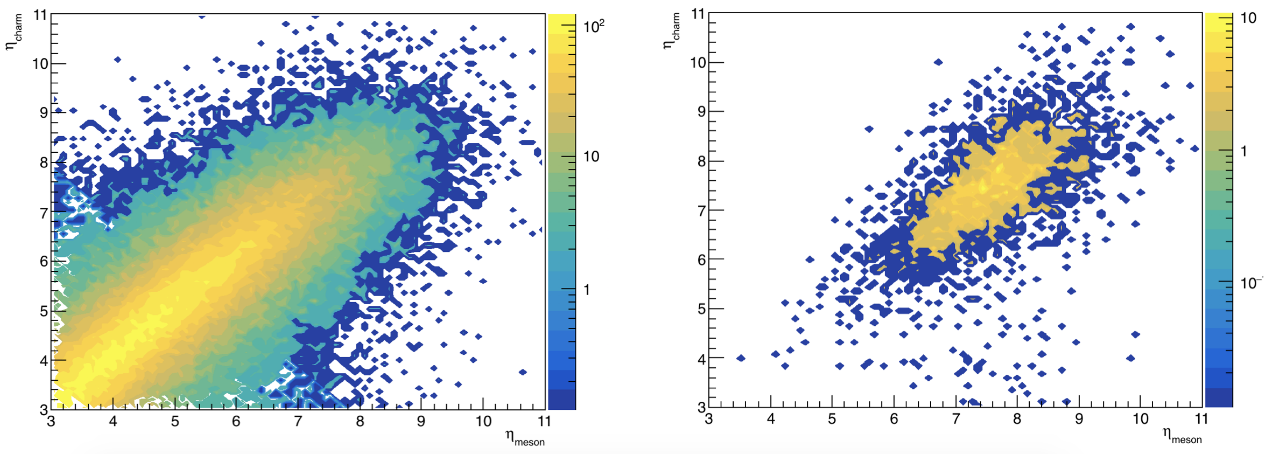

Figure 64: (Left) Correlation between pseudo-rapidities of the parent charm and the charmed hadron. (Right) Only events where the neutrino is in the SND@LHC acceptance are selected.

13.1.2 Lepton flavour universality test in ν interactions

The capability to identify all three neutrino flavours with the SND@LHC detector offers a unique possibility to test Lepton Flavour Universality (LFU) in neutrino interactions. The location of SND@LHC also allows intercepting the neutrino flux component that comes from c and b quark decays, which gives access to tau neutrinos through the decays of D_s mesons. Muon-neutrino and electron-neutrino spectra in the SND@LHC acceptance are shown in Figure 67. The component from heavy-quark decays is represented as the filled area.

The fraction of electron neutrinos produced in pion and kaon decays is about 30% of the total number at the SND@LHC detector target. The number of observed events of neutrinos from pions and kaons is reduced to 10% at the level of interactions, due to their lower energies, and hence lower cross-sections. Assuming that both tau and electron neutrinos come from the decay of charmed hadrons, the ν_e to ν_τ ratio depend only on the decay branching ratios and the charm fractions, thus becoming sensitive to the cross-section ratio of the two neutrino species

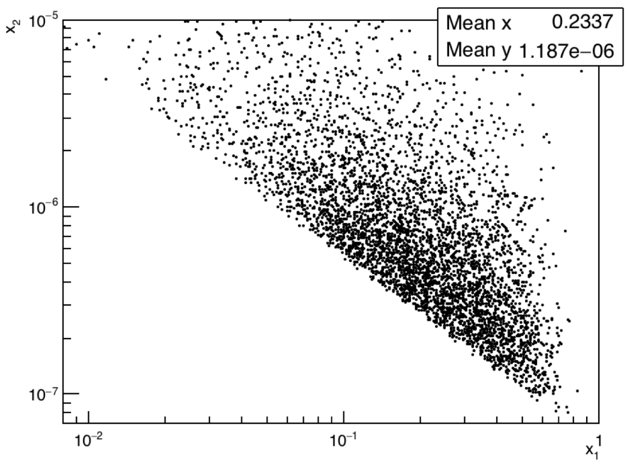

Figure 65: Correlation between x_1 and x_2 momentum fractions for events with neutrinos in the SND@LHC acceptance.

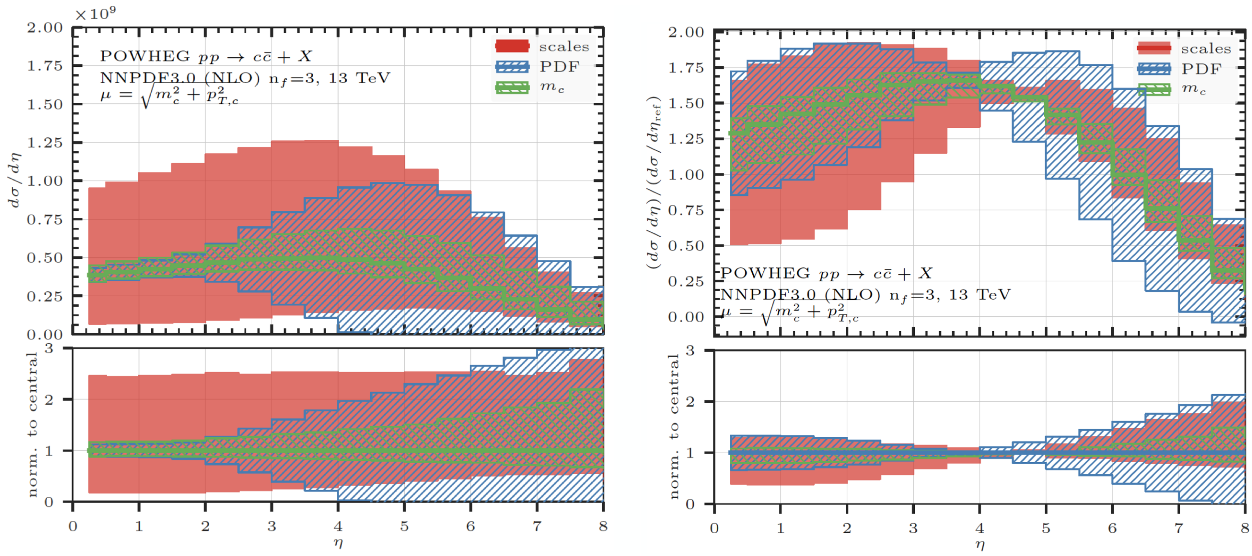

Figure 66: (Left) Differential cross-section for charm production at 13 TeV. (Right) Ratio between the differential cross-section at 13 TeV and the differential cross-section at 7 TeV, with the latter evaluated in the pseudo-rapidity range $4 < \eta < 4.5$.

and allowing for a test of the lepton flavour universality in neutrino interactions. The ν_e to ν_τ ratio (R_{13}) can be written as:

$$R_{13} = \frac{N_{\nu_e+\overline{\nu}_e}}{N_{\nu_\tau+\overline{\nu}_\tau}} = \frac{\sum_i \tilde{f}_{c_i} \tilde{Br}(c_i \to \nu_e X)}{\tilde{f}_{D_s} \tilde{Br}(D_s \to \tau\nu_\tau)}, \tag{3}$$

where $\tilde{f}_{c_i}$ are the charmed hadron fractions and $\tilde{Br}(c_i \to \nu_e X)$ are the branching ratios of each charm species. Notice that $\tilde{Br}(D_s \to \tau\nu_\tau)$ includes also the contribution from the subsequent τ decay, as estimated with the full simulation of the decay chain. The tilde symbol on the above mentioned quantities indicates that they refer to the expected values in the SND@LHC acceptance. The systematic error was evaluated by studying the fluctuations using different generators, after having equalised the branching ratio $D_s \to \tau\nu_\tau$ to the PDG value [11]. The values obtained for R_{13} and $\tilde{f}_{D_s}$ with Pythia8 [109], Pythia6 [110] and Herwig7 [125] generators are reported in Figure 68. The largest difference in R_{13} is observed between Pythia generators and Herwig7. The expected value is $R_{13} = 11.5 \pm 2.5$, corresponding to a 22% systematic uncertainty. The measurement of R_{13} will therefore be dominated by a $\sim 30\,\%$ statistical uncertainty given the modest number of expected ν_τ and $\overline{\nu}_\tau$ interactions.

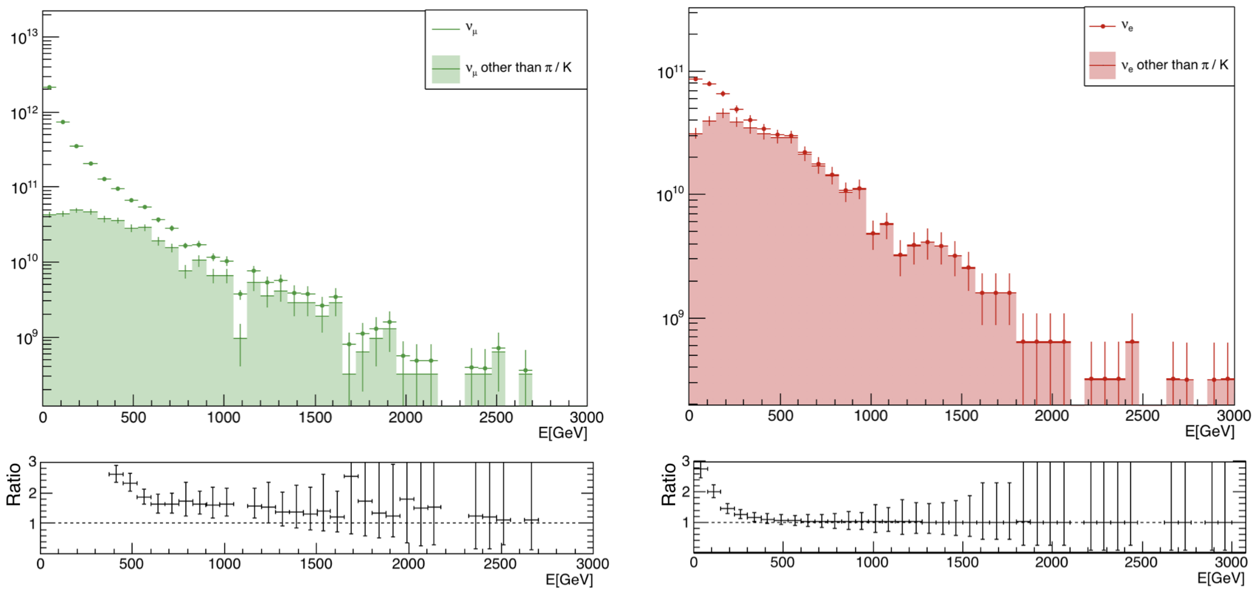

Figure 67: Energy spectrum of muon (left) and electron (right) neutrinos and anti-neutrinos in SND@LHC acceptance. Filled areas represent the component coming from charm decays.

Similarly to electron neutrinos, the muon-neutrino flux is heavily contaminated by muon neutrinos from π/k decays. The contamination is dominating at low energies, but remains relatively flat at the level of 35% for $E > 600\,$GeV, as observed by inspecting Figure 67. The ν_e to ν_μ ratio (R_{12}) can be therefore used as a test of LFU for $E > 600\,$GeV, where the contamination of ν_μ and $\overline{\nu}_\mu$ from pions/kaons ($\omega_{\pi/k}$) is uniform. In this case R_{12} is

$$R_{12} = \frac{N_{\nu_e+\overline{\nu}_e}}{N_{\nu_\mu+\overline{\nu}_\mu}} = \frac{1}{1+\omega_{\pi/k}}. \tag{4}$$

The ratio R_{12} is not affected by systematic uncertainties in the branching ratios and the charmed-hadron fractions since charmed hadrons decay almost equally into ν_e and ν_μ. Since the

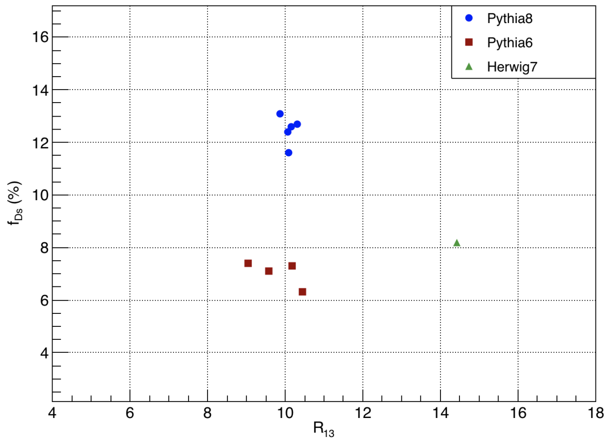

Figure 68: Correlation between variations in R_{13} and f_{Ds} for different generators.

number of expected electron-neutrino and muon-neutrino interactions above 600 GeV amount to about 200 and 300, respectively, the statistical error will be of the order of 10%. The systematic error on R_{12} is related to uncertainties in the knowledge of the light meson contamination, that has two components: the π/k production in the SND@LHC acceptance and the propagation along the beamline. As far as the first component is concerned, the simulation of the light-meson production yield in the forward region is constrained by results published by the LHCf Collaboration [103]. LHCf measured the transverse momentum spectra of neutral pions, as reported in the left panel of Figure 69 for the pseudo-rapidity range $8.9 < \eta < 9.0$. The comparison with several hadronic interaction models shows that an agreement better than 10% is achieved with the EPOS generator for $p_{\mathrm{T}} > 0.3\,\mathrm{GeV}/c$ [126] , that is the region where the majority of neutrinos with $E > 600\,\mathrm{GeV}$ are, as shown in the right panel of Figure 69. The charged meson propagation through the LHC machine is simulated with FLUKA and shows a very good agreement with measurements performed around the beamline, as described in Section 12.1. Moreover, the particle flux in TI18 will be measured by SND@LHC with high accuracy. Additional measurement can be performed in other locations along the beamline to further reduce systematic uncertainties.

Combining statistical and systematic errors, the overall uncertainty on R_{12} amounts to 15%.

13.1.3 Measurement of the NC/CC ratio

The capability to distinguish charged-current and neutral-current neutrino interactions offers the possibility to measure the ratio between NC and CC interactions. In the approximation that the differential ν and $\overline{\nu}$ fluxes as a function of their energy are equal, the NC/CC cross-section ratio

$$P = \frac{\sum_i \sigma_{NC}^{\nu_i} + \sigma_{NC}^{\bar{\nu}_i}}{\sum_i \sigma_{CC}^{\nu_i} + \sigma_{CC}^{\bar{\nu}_i}} \tag{5}$$

is equal to the ratio of the observed events in the corresponding channels. In case of deep-inelastic scattering, the P ratio can be written as a function of the Weinberg angle (θ_W) [30]:

$$P = \frac{1}{2}\left\{1 - 2\sin^2\theta_W + \frac{20}{9}\sin^4\theta_W - \lambda(1 - 2\sin^2\theta_W)\sin^2\theta_W\right\} \tag{6}$$

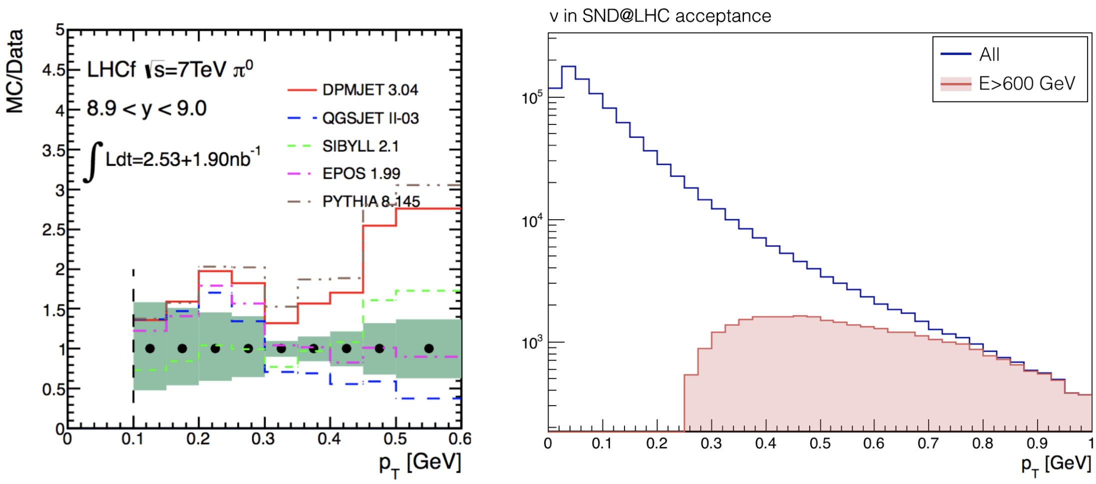

Figure 69: (Left) Ratio of p_{T} spectra of neutral pions measured at LHCf to predicted by hadronic interaction models [103]. (Right) The p_{T} spectra of neutrinos in the SND@LHC acceptance.

where we have only retained the dependence the unequal numbers of protons and neutrons in the target, represented by λ. With a detector target of tungsten, we estimate $\lambda = 0.040$, with an error at the level of a few %, resulting in a 1% correction of the ratio. We expect that non-isoscalarity gives the largest correction to the P ratio [30].

By comparing the measured P with the one expected from the SM it will be possible to verify the prediction. The statistical error on P is given by the number of neutrino interactions and amounts to less than 5%. The migration between charged-current and neutral-current (see Table 13), and the neutron background subtraction, are expected to introduce a 10% systematic uncertainty. An additional source of systematic uncertainty comes from the asymmetry between neutrino and anti-neutrino spectra, that are shown in Figure 70 for muon and electron flavours. The asymmetry between the two components is less than 20% in all energy bins, and it is mainly concentrated in the low energy spectrum of the muon neutrinos, where the contribution of π/k decay is relevant. The systematic error due to the asymmetry amounts to less than 5%.

The overall uncertainty on the measurement of the P ratio is 10%, dominated by the muon identification efficiency and the CC/NC migration. Data driven analyses may further reduce this systematic uncertainty.

13.1.4 Neutrino-induced charm production

High-energy neutrino interactions produce charmed hadrons at the level of about 10 percent of the total rate at the SND@LHC energies, and consequently, they constitute a powerful tool to study charm physics. Unlike colliding beams, neutrino interactions also produce charmed hadrons via processes like quasi-elastic and diffractive scattering, which makes them a unique tool for exclusive charm studies [7]. Figure 71 shows Feynman diagrams for the production of charmed hadrons in neutrino and anti-neutrino interactions. Data on charmed-hadron production in neutrino and anti-neutrino charged-current interactions were reported by many experiments. Among them, the NuTev [127] experiment collected a large number of charmed hadron candidates (5102 in ν_μ and 1458 in $\overline{\nu}_\mu$ interactions) in a (x, Q^2) region that overlaps with the one explored by SND@LHC.

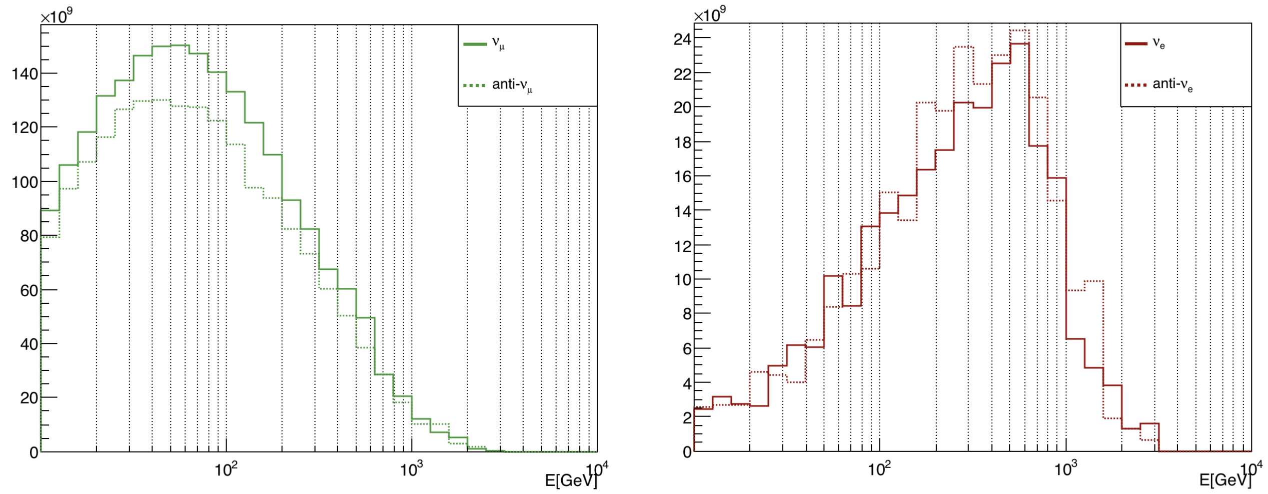

Figure 70: Comparison between neutrino and anti-neutrino energy spectrum for muon (left) and electron (right) neutrinos.

The nuclear emulsion technology offers a unique possibility to identify charmed hadrons through the observation of a two vertex topology, such that no kinematical cuts are required. The emulsion experiment with the largest neutrino flux was CHORUS [128]. It measured 2013 charm candidates coming from ν_μ, and 32 coming from $\overline{\nu}_\mu$. A tau-neutrino candidate with charmed-hadron production was reported by the OPERA experiment [129]. No charm candidate from electron-neutrino interactions was ever reported.

The relative charm-production yield in muon and electron neutrino and anti-neutrino interactions expected at SND@LHC energies is reported in Table 18, together with the expected charm yield in 150 fb^{-1}. The yields will allow updating the results of previous studies on charm physics performed with neutrino interactions, and some of the channels that were inaccessible in the past will be explored.

Unlike ordinary neutrino scattering, where the presence of valence quarks favours the d quark as the neutrino target, and thereby, compensates for the large suppression due to the Cabibbo angle, charmed-hadron production in anti-neutrino interactions selects the anti-strange quark in the nucleon, as sketched the right panel of Figure 71. Measurements at SND@LHC can be used to measure the s-quark content of the nucleon, thus providing important information for many precision tests of the SM.

When the lepton produced in the neutrino charged-current interaction is not identified, $\nu_\mu(\bar{\nu}_\mu)$ and $\nu_e(\bar{\nu}_e)$ interactions with subsequent charmed-hadron production are the main background to ν_τ searches. Given the muon identification efficiency, the expected number of charged charmed hadrons induced by ν_μ $(\bar{\nu}_\mu)$ that mimic the τ decay is 13 in 150 fb^{-1}. As demonstrated by the OPERA experiment [19], the events can be rejected (a factor of about three with a cut-based analysis) by exploiting kinematical features, such as the fact that the lepton and the hadronic jet at the neutrino interaction are expected to be back-to-back in the transverse plane. As a results, the signal-to-background ratio in the tau neutrino search is expected to be about four as reported in Table 19.

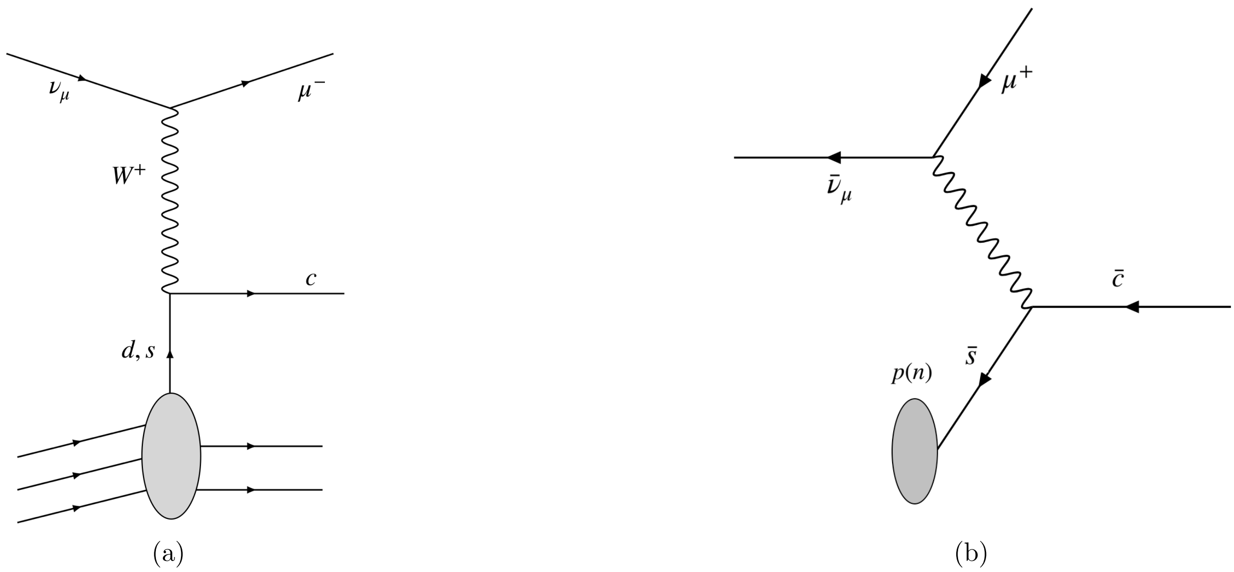

Figure 71: Charm production in neutrino (a) and anti-neutrino (b) charged-current interactions.

Neutrino flavour	$\langle$E$\rangle$ [GeV]	Charm CC-DIS Interactions	N_{charm}/N_{CC} (%)
ν_μ	510	60	8.2
ν_e	720	22	9.4
$\bar{\nu}_\mu$	585	28	9.6
$\bar{\nu}_e$	790	14	11.5
TOT		124	9.0

Table 18: (Left column) Expected number of CC-DIS interactions with subsequent charm production for the different neutrino flavours in the assumption that $150\,\text{fb}^{-1}$ are collected. (Right column) Fraction with respect to the total number of CC-DIS interactions.

13.1.5 Summary of physics results with neutrinos

Table 19 summarises the main Run 3 physics objectives with the SND@LHC detector in the analyses of neutrino interactions. The proposed measurements are reported together with the estimated uncertainties, as described in detail in the corresponding sections.

Measurement	Uncertainty Stat.	Sys.	Signal/Background
$pp \to \nu_e X$ cross-section	5%	15%	
Charmed hadron yield	5%	35%	
ν_e/ν_τ ratio for LFU test	30%	22%	
ν_e/ν_μ ratio for LFU test	10%	10%	
NC/CC ratio	5%	10%	
Observation of high-energy ν_τ			4

Table 19: Measurements proposed by SND@LHC in the analyses of neutrino interactions with Run 3 data.

13.2 Search for Feebly Interacting Particles

The increasing interest in the understanding of the nature of dark matter has lately been accompanied by a mounting experimental effort of the scientific community, both in direct and indirect searches as described in Section 2. Complementary approaches such as the direct observation of accelerator-produced dark matter via scattering off electrons have been conceived, as proposed by the SHiP experiment at the CERN SPS [30, 130].

The SND@LHC experiment is also capable of performing model-independent direct searches for FIPs by combining the search for a recoil signature with a time-of-flight (TOF) measurement to reject neutrino interactions that can act as background. With a time resolution of $\sim$200 ps, it will be possible to disentangle the scattering of massive FIPs and neutrinos, with a significance that depends on the particle mass. The region that may be explored with this technique is shown in terms of sensitivity curves from 1σ to 5σ in the plane (M_{NP}, p_{NP}) in Figure 72, where M_{NP} and p_{NP} denote the mass and momentum, respectively, of the new physics candidate to be distinguished from ordinary neutrinos. The 1σ contour in Figure 72 corresponds to a γ factor of about 50, while the 5σ one to a γ factor of about 25.

The SND@LHC experiment can explore a large variety of Beyond Standard Model (BSM) scenarios describing Hidden Sectors. In the following we consider a light dark matter (LDM) scattering off nucleons and off atomic electrons.

13.2.1 Scattering off nucleons

We consider here a model with a scalar particle χ coupled to the Standard model via a leptophobic portal, i.e. an interaction of a vector mediator V with the baryon current J^B_μ [47, 49, 131, 132, 50] described by the following Lagrangian:

$$\mathcal{L}_{\mathrm{leptophob}} = -g_B V^\mu J^B_\mu + g_B V^\mu (\partial_\mu \chi^\dagger \chi + \chi^\dagger \partial_\mu \chi), \quad J^B_\mu = \frac{1}{3} \sum_q \bar{q} \gamma_\mu q \tag{7}$$

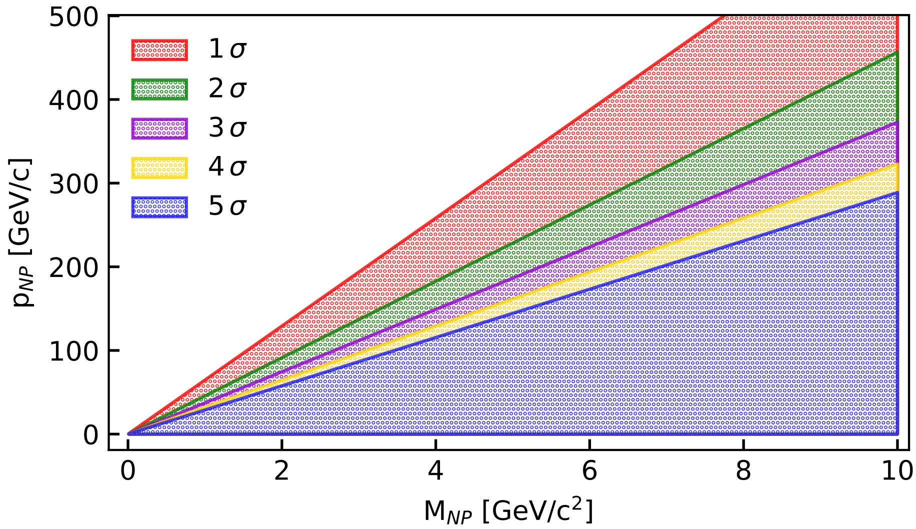

Figure 72: Sensitivity curves for a TOF measurement, illustrated from 1σ up to 5σ in the plane $(M_{\mathrm{NP}}, p_{\mathrm{NP}})$ of the FIP candidates to be detected in the SND@LHC, assuming a time resolution of ~ 200 ps.

Constraints on this portal come from invisible π and η decays, monojet signatures and invisible decays of J/ψ and Υ [47, 133], as shown in Fig. 74. The monojet signatures at ATLAS and CMS require a large missing transverse energy $E_T \sim 100$ GeV for tagging and suppressing the background, which produces a rather limited sensitivity to $\mathcal{O}(1\text{ GeV})$ mediators. For the Υ and J/ψ decays, the sensitivity is limited to narrow mass regions $m_V \sim m_{\Upsilon,J/\psi}$.

Here and below, we consider the case $m_\chi = m_V/3$. The analysis and results for other choices of the mass are qualitatively similar. $\chi\bar{\chi}$ pairs originate from decays of Vs. In pp collisions, the mediator may be produced via the following processes:

1. decays of unflavoured mesons π, η,

$$\pi \to V + \gamma, \quad \eta \to V + \gamma, \tag{8}$$

2. proton bremsstrahlung, $p + p \to V + X$,

3. Drell-Yan process, $q + \bar{q} \to V + X$.

We follow the description of these production channels from [133]. For the production from mesons, we use the polar angle-energy distributions of π and η-mesons from [134]. The subsequent spectra of V and χ particles have been obtained semi-analytically using an approach presented in [135]. The distribution of χ particles produced via bremsstrahlung has been obtained in a similar way. For the Drell-Yan production, we have implemented the model (7) in MadGraph5 [136] using FeynRules [137, 138]. We then obtained the geometrical acceptance and energy distribution of χ particles entering the SND@LHC detector by simulating the leading-order process $p+p \to V, V \to \chi\bar{\chi}$. We have found that the main production channel for masses $m_V < m_\eta$ is the decay of mesons, for masses $m_\eta < m_V \lesssim 3$ GeV the proton bremsstrahlung, and $m_V \gtrsim 3$ GeV the Drell-Yan process.

In order to compute the branching ratio

$$\mathrm{Br}_{V\to\chi\bar{\chi}} = \frac{\Gamma_{V\to\chi\bar{\chi}}}{\Gamma_{V\to\chi\bar{\chi}} + \Gamma_{V\to\mathrm{hadrons}}}, \tag{9}$$

we estimate the decay width into hadrons $\Gamma_{V\to\mathrm{hadrons}}$ via the decay width into quarks (from Equation (7)), with the quark mass replaced by the mass of the corresponding meson).

χ particles entering the SND@LHC detector volume may scatter off nucleons N, either elastically or inelastically. We adopt the description of the elastic process from [131] and consider scattering off protons only, which leads to a visible experimental signature of one charged track originating at the point of interaction. For the inelastic scattering, we use the parton model described in Ref. [48] with the PDFs provided by LHAPDF [139] with CT10nlo PDF sets.

The number of scattering events is estimated as

$$N_{\mathrm{events}} = 2\cdot N_{\chi}^{\mathrm{SND}}\cdot n_{\mathrm{target}}\cdot (Z\sigma_{\mathrm{scatt}}^{\mathrm{elastic}}(\langle E_{\chi}\rangle) + A\sigma_{\mathrm{scatt}}^{\mathrm{DIS}}(\langle E_{\chi}\rangle))\cdot l_{target} \tag{10}$$

where N_{χ}^{SND} is the number of χ particles produced within the acceptance of the SND@LHC detector (the factor of two stays for $\bar{\chi}$), n_{target} is the atomic number density of the target, σ_{scatt} is the scattering cross-section. The expected number of events scales as α_B^3, where $\alpha_B = g_B^2/4\pi$, with one power coming from the production, and the other two from the scattering.

	$\chi p\to\chi p$ Selection eff.	Background
NC DIS	2.8×10^{-3}	1.26
NC RES	1.7×10^{-1}	0.48

Table 20: Selection efficiency and background yield for the dark matter elastic scattering off protons for $\mathcal{L} = 150\,\mathrm{fb}^{-1}$.

We discuss here the background yield in the two channels. The simulation includes the following interaction processes: $\nu_e(\bar{\nu}_e)$ and $\nu_\mu(\bar{\nu}_\mu)$ CC and NC Deep Inelastic Scattering (DIS), CC and NC Resonant Scattering (RES), CC and NC Quasi-Elastic Scattering (QE), Elastic Scattering on protons (EL), CC and NC Coherent Scattering (COH). A full Monte Carlo simulation was performed by means of the software packages described in Section 12. The experimental signature of the elastic scattering process off protons, $\chi p\to\chi p$, consists of a single proton reconstructed in the detector target region. The background consists of neutrino interactions where only one charged hadron track is reconstructed at the primary vertex. Once visibility criteria (Table 12) are applied to the tracks produced in neutrino scattering, the only processes contributing to background are NC DIS and NC RES, as reported in Table 20. The background yield can be reduced by $\sim$30% if the visibility cut for π^0 and γ, now conservatively set at 400 and 200 MeV, respectively, is reduced to 100 MeV. Further reduction based on the kinematics is not considered here and it is supposed to reduce the background to a negligible level.

The DIS process is dominant for neutrinos, given the higher mass of the Z-boson mediator. Neutrino NC deep-inelastic interactions cannot be distinguished from the DIS signal by using the topology only. Therefore, the sensitivity curve is derived under the assumption of a 3σ

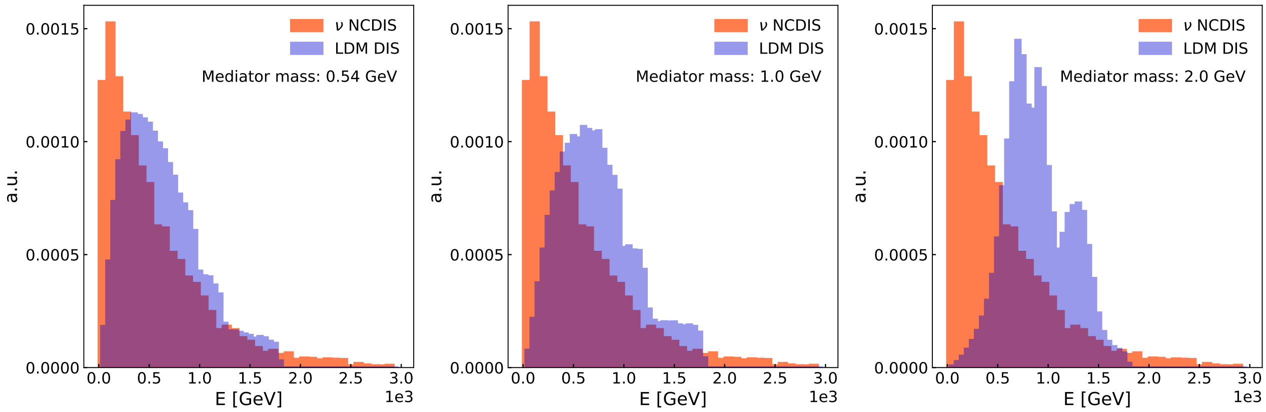

Figure 73: Energy spectrum of NC DIS neutrino interactions superimposed to that of a dark matter DIS interaction, for three mass values of the mediator.

level excess, corresponding to about 60 events. Figure 73 shows that the energy distribution for neutrinos and LDM, when they interact via DIS, tend to be separated at larger (from about 1 GeV) masses of the mediator.

Figure 74 shows the sensitivity to the leptophobic portal assuming the integrated luminosity $\mathcal{L} = 150\,\mathrm{fb}^{-1}$. The two processes are drawn separately. There is a large region of the parameter space where SND@LHC extends the limits of current searches [140, 141, 142, 143, 144].

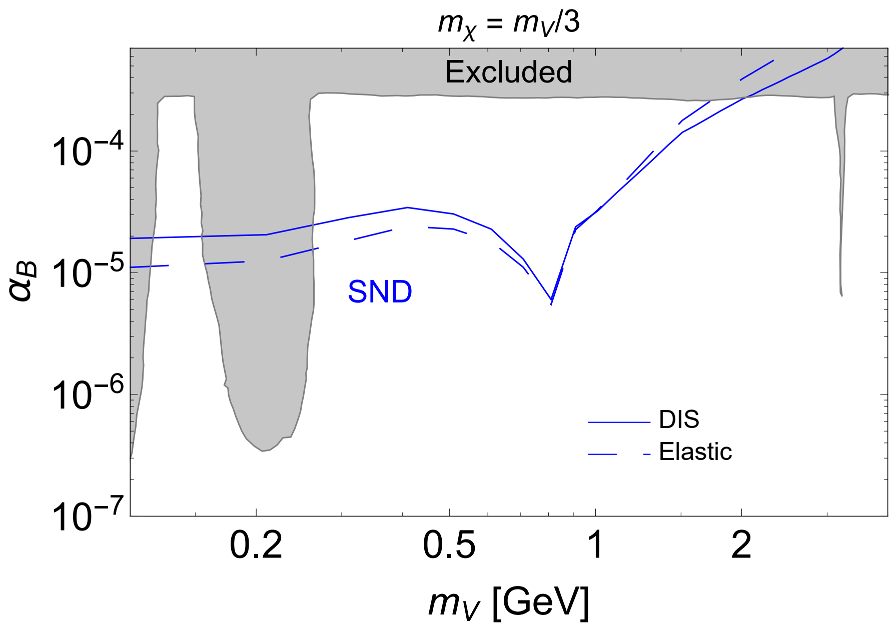

Figure 74: Sensitivity of the SND@LHC experiment to the leptophobic portal for both elastic scattering off protons (dashed blue line) and deep-inelastic scattering (solid blue line). The grey region is already excluded by the CDF monojet searches [140, 141], BES searches for invisible J/Ψ decays [142], E949 rare K decays [143] and π^0 decays at the Brookhaven alternating gradient synchrotron [144].

13.2.2 Elastic scattering off electrons

In this section we consider the Vector Portal in a minimal SM extension, with the production of a vector mediator *Dark Photon* $\mathcal{A}'$ (DP):

$$\mathcal{L}_{\mathcal{A}'} = -\frac{1}{4}F'_{\mu\nu}F'^{\mu\nu} + \frac{m^2_{\mathcal{A}'}}{2}A'^{\mu}A'_{\mu} - \frac{1}{2}\epsilon F'_{\mu\nu}F^{\mu\nu}\,, \tag{11}$$

kinetically mixed with the photon field $F^{\mu\nu}$ via the coupling ϵ.

For this study we consider prompt decays of DP into a pair of light dark matter candidates χ (i.e. $m_\chi \sim O(1\,\mathrm{GeV}/c^2)$ either fermionic or scalar, charged under a new $U'(1)$ symmetry:

$$\mathcal{L}_\chi = g_D\,A'^{\mu} \times \begin{cases} \bar{\psi}_\chi\gamma_\mu\psi_\chi \\ i[(\partial_\mu\phi^\dagger_\chi)\phi_\chi - \phi^\dagger\partial_\mu\phi_\chi] \end{cases} \tag{12}$$

being ψ_χ and ϕ_χ the fermionic and scalar candidates, respectively. The parameter g_D denotes the gauge coupling of the introduced dark sector U'.

In the regime $m_{A'} > 2\,m_\chi$ (invisibly decaying DP) and $\alpha_D = g_D^2/4\,\pi \gg \epsilon\,e$, it is reasonable to assume a short-lived DP with $\mathrm{BF}(A' \to \chi\chi^\dagger) \sim 1$.

At SND@LHC, a multitude of processes give rise to the production of DPs and, consequently, LDM particles. In the considered mass range $m_{\mathcal{A}'} \lesssim 1\,\mathrm{GeV}$, two mechanisms are leading:

- *Meson decays*: DPs abundantly originate from radiative decays of light mesons in

$$\pi^0,\ \eta,\ \eta' \to \gamma\mathcal{A}',$$
$$\omega \to \pi^0\mathcal{A}'\,.$$

- *Bremsstrahlung of protons*: interacting primary protons at the LHC collision point radiate DPs at a very low angular spread.

It is here noted that on-shell production of DPs from prompt-QCD interactions contributes to a negligible extent, thus it is ignored for this study.

The scattering $\chi\,e^- \to \chi\,e^-$ is detected through the reconstruction of the recoil electron-induced shower in the target region. Possible backgrounds to this search consist of neutrino interactions where exclusively one charged track, either an electron or positron, is reconstructed at the primary vertex. Different contributing channels have been investigated, namely: neutrino-electron elastics scattering (ES) $\nu_x\,e^- \to \nu_x\,e^-$, exhibiting the same topology of the signal; $\nu_e(\bar{\nu}_e)$ CC Deep Inelastic Scattering (DIS), CC Resonant Scattering (CC RES) and CC Quasi-Elastic Scattering (CC QE) with soft undetectable tracks at the neutrino vertex.

Once visibility criteria (Table 12) are applied to the tracks produced in neutrino scattering, the only processes that contribute to background are CC QE, CC RES and ES, as reported in Table 21. The overall background yield is less than one in all channels and can be further reduced by applying kinematical cuts on the electron slope and energy, as demonstrated in Ref. [55]. Zero background is therefore assumed in the following analysis.

A full MC simulation has also been performed for the signal. LDM candidates have been produced by means of the Pythia8 [109, 145] and MadDump [132] MC generators, the latter tuned to describe the current detector configuration and model physical parameters: a benchmark scenario is assumed, in which $m_{\mathcal{A}'} = 3\,m_\chi$ and $\alpha_D = 0.1$.

We report in Figure 75 the projected 90% C.L. exclusion limits in the plane (M_χ, Y), where $Y = \epsilon^2 \alpha_D \left(M_\chi/M_{A'}\right)^4$, for the full data-taking period ($150\,\mathrm{fb}^{-1}$), compared to existing constraints. It has to be noted that the sensitivity is within the limit set recently by the NA64 experiment [146], in orange in Figure 75. Nevertheless, SND@LHC will use a complementary approach, based on the direct detection rather than on the missing-energy technique. Among the direct detection searches, SND@LHC will extend the region of the parameter space explored by the MiniBooNE neutrino experiment [147], highlighted in grey in Figure 75.

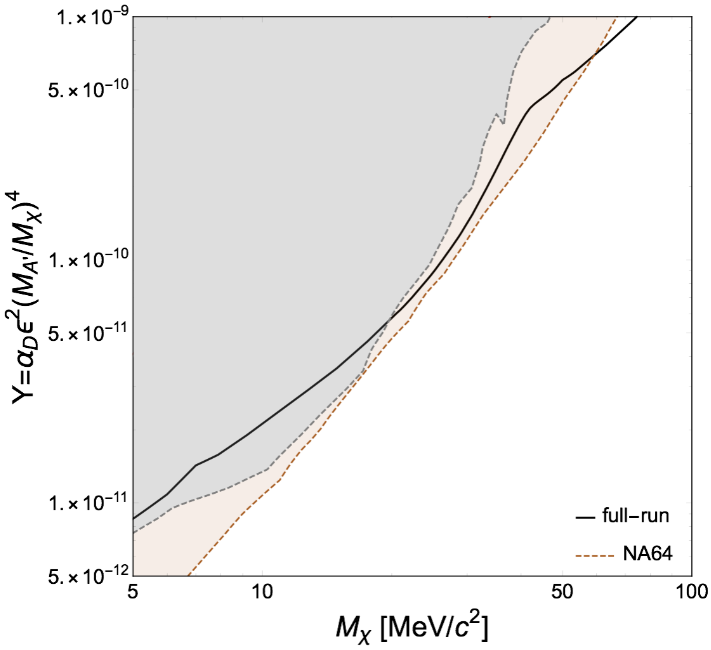

Figure 75: SND@LHC 90% C.L. exclusion limits in the 0-background scenario for a LDM candidate χ originating from the prompt decay of a DP $\mathcal{A}'$, assuming as benchmark parameters $m_{\mathcal{A}'} = 3\,m_\chi$ and $\alpha_D = 0.1$. The grey region is excluded by MiniBooNE [147] while the orange one by NA64 [146].

	$\chi\, e \to \chi\, e$	
	Selection eff	Background
EL	$3.6{\times}10^{-2}$	0.16
CC RES	$4.0{\times}10^{-3}$	0.002
CC QE	$2.2{\times}10^{-2}$	0.11

Table 21: Selection efficiency and background yield for the light dark matter scattering off electrons.

14 Overall cost and schedule

14.1 Cost

While the overall detector layout, as well as the measurement strategy remain, several important technological changes have been made to the detector since the LoI [1], in order to optimise the construction time and the resources required. The emulsion film size has been reduced from $400 \times 400\,\mathrm{mm}^2$ to $192 \times 192\,\mathrm{mm}^2$, avoiding the need for R&D on production tooling, and associated costs. The dimensions of the tungsten plates have been equally reduced. Only one company replied to producing plates with the large dimensions while several companies are available to deliver the reduced size. The corresponding loss of fiducial volume has been compensated by a higher density tungsten alloy and by a 5% increase of the target wall thickness. The settled choice of technology for the three downstream muon stations consists of scintillator bars, analogous to the bars used for the veto stations and the upstream muon station. Instead of staggered bars, all muon scintillator planes have the bars organised side-by-side to save longitudinal space and avoid interference with the tunnel wall downstream of the detector. By default the last three muon stations will have two detector planes oriented orthogonal to each other, but space has been reserved for a third stereo layer, should further studies show that it it is necessary to suppress ghost hits. The readout system has been fully harmonised by employing the same FE boards and DAQ boards as foreseen for the target tracker, for all the electronic detectors.

The global cost estimate, updated since the LoI [1], is shown in Table 22, together with the main groups responsible for the construction of each subsystem. The estimate is based on the detailed cost breakdowns for each subsystem (see corresponding sections) and the preparatory works. The production and construction costs of the detector systems are based on the concept of deliverables, which include the detector components and assembly, the associated electronics and supply systems, as well as transport to CERN. Wherever applicable, the material cost estimate includes the industrial support labour. The costs also include spares but no contingency. The cost of the emulsion films corresponds to three years of data-taking with a total integrated luminosity of $150\,\mathrm{fb}^{-1}$, corresponding to six replacements of $44\,\mathrm{m}^2$. The large difference in the cost of the target tracker and the muon system between the LoI and the TP comes from the fact that the LoI had the electronics and readout systems included in the sub-detector cost.

The reliability of the cost estimate is considered Class 2 $\left({}^{+(5-20)\%}_{-(5-15)\%}\right)$ as the costs of the individual items in the breakdowns are based on dedicated commercial offers, or the same or similar systems recently produced or constructed elsewhere. The cost of the emulsion films in the LoI was based on the raw material cost from Nagoya. The current cost is based on an offer from the Slavich Company (Russia) for the complete production. The cost for the reduced size tungsten plates is based on already ordered plates. The SciFi technology for the target tracker has been constructed for the LHCb and for the LHC-BGV [148] detectors, and four out of the five chambers to be used in the SND@LHC target tracker have already been constructed for the SHiP-charm experiment and refurbished for SND@LHC. The cost of the cooling box has a relatively large uncertainty depending on the choice between boron carbide or borated polyethylene for the neutron shielding. The cost of all scintillator bars are based on complete offers. All detector services are based on commercially available hardware. The iron blocks for the muon filters are available at CERN. For the readout and control system, the FE ASIC was ordered together with LHCb, and the DAQ boards are available commercially for delivery in spring 2021. The rest of the online system, and detector supplies are based on commodity hardware widely available. The cost breakdown in Table 11 to prepare the experimental area and the infrastructure are based on yet more detailed breakdowns, including work plans, elaborated by the responsible equipment and service groups at CERN. The works require only material, equipment and procedures that have been used elsewhere. From discussions with the CERN management it is expected that CERN will contribute with the infrastructure as part of the host lab responsibility.

Owing to already requested funding, reuse of detector components, and the use of standard equipment, 40% of the detector cost can be considered pledged. This includes allocation for emulsion for the 2022 data-taking, during which one replacement is expected (i.e. a total of $2 \times 44\text{m}^2$).

The preparation of the emulsion bricks and the development of the films require a dark room and development facility. An equipped facility exists in building 162 (S-13, 17, 19) and 169 (S-203 and 18) that has been heavily used by WA75 [149], CHORUS [150], OPERA [56], and more recently by NA65/DsTau [151] and SHiP-charm [113]. It is expected that SND@LHC will continue to use this facility, shared in 2022–2024 with other expected users (FASERν [3], NA65/DsTau [151] and SHiP-charm [113]). Discussion with the other users are ongoing to draw up a plan for shared use, and determine the changes that will need to be done to the lab to support transport, brick assembly, development, and handling and storage/disposal of chemicals for all experiments. Possible sharing of several components has been identified, such as a mobile crane and table for assembly, development racks and trays, and ancillary material, as well as microscopes for quality control. In terms of changes to the lab facility, SND@LHC only requires defining an appropriate scheme for storage and disposal of chemicals. The shared use with all experiment requires a more extensive renovation to support the needs of all future users, including reorganising the sub-activites within the facility. Furthermore, the current access and dark room chicane is too narrow, access should be moved to the existing double-door. Doors should be equipped with electronic locks, and the current air conditioning needs to be upgraded to achieve lower humidity. Since FASERν and SND@LHC have similar schedules for the emulsion replacement and development, it is envisaged to swap the use of the periods immediately before and after each LHC Technical Stop. This requires temporary storage of the exposed detector/detector prepared for installation. The storage should be located in an underground area with only natural radioactivity to reduce exposure to cosmic radiation. SND@LHC and FASERν will put forward a common request to CERN for the renovation of the lab. It will also include a request to extend the emulsion facility with two additional rooms for storage of equipment and drying of emulsion films, and the request for the underground storage. The cost for the emulsion lab facility in Table 22 only includes equipment specifically needed for SND@LHC.

Five scanning microscopes are available in the SND@LHC collaboration, four of which are installed in outside institutes and one of which is stored at CERN. The cost for the emulsion detector includes upgrades of all microscopes. The collaboration will request a small room at CERN for the permanent installation of one scanning station.

SND@LHC will not require a conventional control room for the operation of the detector. It is envisaged to operate the detector from a dedicated office at CERN. The space will be requested from CERN.

Preparation of an MoU dedicated to the detector construction has started. It will define the final boundaries between the responsibilities for the deliverables. A second MoU will be prepared to define the financial strategy for the maintenance and the operation of the detector.

Item	Cost (kCHF)		Responsible
	TP	LoI	
Infrastructure	141.6	120.0	CERN[24]
Emulsion lab facility	66.0	not incl.	GNUE(KR)[13], INFN Naples(IT)[9,c], CERN[24]
Scanning microscopes	130.0	not incl.	LPI(RU)[19], INFN Bologna(IT)[7,b], INFN Naples(IT)[9,c], UZH(CH)[26], CERN[24]
Veto system	10.3	10.0	UZH(CH)[26]
Emulsion target	904.1	405.0	INFN Naples(IT)[9,c], MISIS(RU)[21], METU(TR)[27,f], NU(JP)[11]
Target tracker	68.5	280.0	EPFL(CH)[25]
Muon system	88.4	160.0	HU(DE)[3], INFN Bologna(IT)[7,b], JGU(DE)[5], UZH(CH)[26]
Electronics (all)	238.1	incl. in det.	EPFL(CH)[25], HU(DE)[3], INFN Bologna(IT)[7,b], JGU(DE)[5], UZH(CH)[26]
DAQ + online	29.0	not incl.	EPFL(CH)[25]
Total	**1676.0**	**975.0**	

Table 22: Breakdown of the global cost of SND@LHC, including infrastructure, as estimated for the Technical Proposal, together with the institutes currently responsible. The large difference in the cost of the target tracker and the muon system between the LoI and the TP comes from the fact that the LoI had the electronics and readout systems included in the sub-detector cost. The difference in the cost of the emulsion is explained in the text. The label for each institute refers to the list of institutes in the Author List. Note that not all SND@LHC institutes have indicated financial commitments yet.

14.2 Schedule

The SND@LHC project timeline is motivated by the unique opportunity to perform the measurements in Run 3 of the LHC, and the high and broad interest in the physics case. The schedule assumes full project approval by the end of March 2021 and being ready for data taking by the beginning of 2022 with a complete detector. It takes into account the current detailed schedule of the LHC in 2021 and 2022 (version 3.1). According to the schedule the detector must be fully installed, and commissioning in situ be performed, by the second week of January 2022. To cause minimal interference, the work plan for SND@LHC aims at taking maximum advantage of the periods where Sector 1-2 in the LHC is accessible during the second half of 2021.

The schedule relies critically on finalising all preparatory works for the experimental area, infrastructure, and services by the end of October 2021. The time needed for the interventions have been estimated to about eight weeks, including time for preparation on the surface and scheduling. The detailed timeline for the works to prepare the experimental area and the infrastructure has been elaborated in collaboration with the CERN equipment and service groups, the LHC coordination, and safety, and is shown in Figure 76. It is considered fully realizable. It takes into account the expected commissioning with beam in week 39 of 2021, and the availability of the groups. The work plan is organised such that as much as possible can be

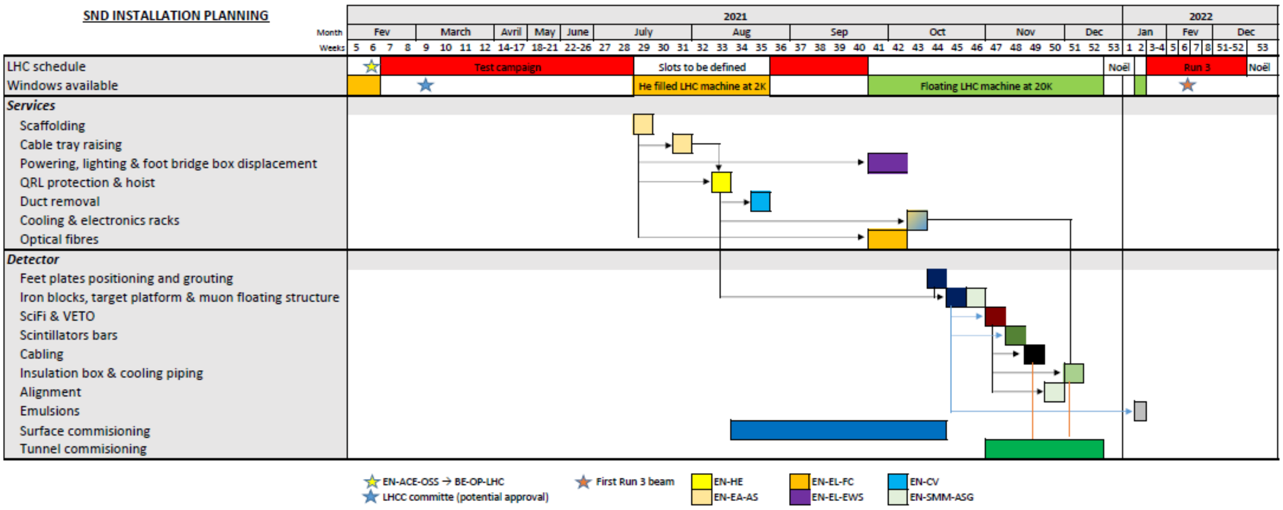

Figure 76: Preliminary schedule for the works to prepare the experimental area and to install the detector.

done during the months of July–August with a minimum of access to the tunnel. The remaining works will be performed in the month of October. Special attention has been paid to ensure that all works and installation can be carried out with the LHC in cold state with no impact on the schedule and plans for the machine in 2021. A small set of minimal interventions that are incompatible with the state of the LHC in 2021, were carried out in 2020 to cleanup the zone, reroute existing cables, as well as improving the electrical distribution [88]. It has been verified that the works scheduled for 2021 on the infrastructure and the transport, and installation of the detector, are already covered by existing work safety authorizations or others that are in preparation. It is expected that any additional procedure that may arise can be done between the approval and the start of the first underground works in July 2021. The critical path for the infrastructure items is defined by the cooling station. Six months are needed for the design and commissioning of the chillers in a lab before they are installed in the tunnel. Owing to the fact that the station is the same as the one installed for FASER, a project approval by the end of March 2021 is considered safe for a timely installation.

The proposed plan of the work packages allows work on the final items of infrastructure and services to go in parallel with the first phase of detector installation, consisting of mechanics, racks, electronics and cooling.

The detector installation and commissioning is expected to take two months, and will start in October 2021. The preparation and installation of the emulsion bricks will be done as late as possible before the closure of the LHC for the start of re-commissioning with beam, to minimise unnecessary exposure. In the current schedule the installation of the emulsion bricks is foreseen for the second week of January 2022.

In order to cope with the short time for the installation underground and the in-situ commissioning, it is planned to partially setup the detector, including the DAQ system, on the surface in advance and run tests with cosmics. The setup will also be essential to test and practice the emulsion replacement and commission detector before installation underground. Several options are considered for the location.

The operational schedule involves replacing the emulsion films every 25 fb^{-1}, expected twice a year. A second complete set of tungsten plates will be available to prepare the replacement bricks in advance. The construction of the 4×5 emulsion bricks requires less than one week in the dark room. In the baseline plan, this operation will be done right before the LHC Technical Stops. The sharing of the dark room facility will mean that the replacement bricks will have to be prepared a bit earlier every second stop and be temporarily stored in a location well shielded from cosmic radiation.

The bricks do not require replacement exactly every $25\,\mathrm{fb}^{-1}$. There is margin to adapt the replacements to the planning of the LHC Technical Stops. A conservative approach will be taken, in particular in the first year of operation. The cooling box, and the hybrid target system with the target tracker, have been designed to allow rapid extraction of the exposed bricks and installation of the new bricks such that the complete replacement can be done in a shift of eight hours, not including access and transport. The detailed procedure, including the transport and access, with the radiation protection and the detector teams, is in preparation.

Similarly to the detector preparation, the development should take place as soon as possible after extraction. With the sharing of the lab and getting immediate access to the lab only every second Technical Stop, the exposed bricks will need temporary underground storage, to be shielded from cosmic radiation.

The possibility of performing the actual replacement of the emulsion bricks in only one eight-hour shift opens the possibility to replace the emulsion in any longer interruption of the operation of the LHC, should it be needed.

14.3 Risk analysis

It is recognized that the preparatory works and detector installation in 2021 are on a challenging critical path to commence data taking with a full detector in 2022. However, the definition of the infrastructure and services is mature and the preparatory works have already been elaborated in detail with the CERN equipment and service groups. The works are either routine works or works that have been recently done for other installations (e.g. FASER), environment and conditions are well understood, and standard material and equipment are used for which lead-times are well known. The scheduling of the works can be adapted to changes in the LHC schedule. The Engineering Change Request associated with all the interventions has been prepared and has already been through a first circulation with all involved groups and management. The document will be circulated for formal approval immediately following formal approval of the SND@LHC project.

The SND@LHC detector is based on well-known technologies, no further R&D is needed, and the collaboration has significant experience with the detector concept and the technologies from the OPERA, SHiP, SHiP-charm, and LHCb experiments.

All preparations for the detector construction are proceeding as expected in terms of the availability of material and personnel. The rationalization applied to the choice of detector technologies since the LoI significantly reduces risks in the production of the detector. Several items are already ordered, or lead-times are known, and several components are either available or have already been purchased, while several others have been constructed. The reduced dimensions, and hence reduced weight, of the $200 \times 200\,\mathrm{mm}^2$ emulsion bricks reduces several risks, associated with procurement and quality of both emulsion films and tungsten plates, and eases the handling and the installation/extraction. Effort is put on being ready for commissioning on the surface with a partial setup in September 2021.

A delay of an item would not remit start of data taking and would still allow important measurements of backgrounds and analysing neutrino flux. The open geometry and simplicity of the design would allow any remaining item to be installed with only minor efforts such that they could be done in the first Technical Stop.

Redundancy have been built in to the critical systems, such as the cooling, in order to guarantee that the detector can either be operated or put in safe conditions until the first opportunity for access. Access to the area requires only standard LHC access procedures.

15 Organisation

SND@LHC is currently a collaboration of 20 institutes, in total representing 10 countries plus CERN.

The formal organisation of SND@LHC currently consists of an Institutions Board (IB) with a formal Chairperson, Spokesperson, and Technical Coordinator.

The IB is composed of representatives from each Institute, and is the forum for decision and policy-making. It represents the ultimate authority of SND@LHC. It elects its own Chairperson, the Spokesperson, and the Technical Coordinator. The Technical Board is composed of the sub-system project leaders, which are ratified by the IB. The present appointments are:

Spokesperson: G. De Lellis, Naples University and INFN, IT
IB Chairperson: N. Polukhina, Russian Academy of Science, RU
Technical Coordinator: R. Jacobsson (CERN)
EXSO: R. Jacobsson (CERN)

Safety contacts are L. Di Giulio (CERN/EP) and M. Andreini (CERN/HSE)

16 Future prospects

Forward physics with neutrinos at the LHC is just past dawn but involves a number of important challenges. The SND@LHC detector concept, with its efficient techniques for identifying the flavour in neutrino interactions and measuring energy, will operate in a new environment but has the potential to pave the way for a more ambitious and extended programme beyond Run 3. Moreover, the Run 3 physics programme is limited by the statistics that will be produced, by the systematic uncertainties, and by the geometrical constraints imposed by the current location. At the same time, while currently no viable alternative exists to achieve the high 3D resolution and compactness of the ECC that is the driving force behind the reconstruction of neutrino interactions, the technology has limitations that will make it unattractive at the experimental conditions of HL-LHC. This demands R&D on new technologies.

The limitation coming from the geometrical constraints of the current site can be overcome by civil engineering. For instance the floor may be recast at the level of the collision axis in order to leave space for a larger target and a longer detector including a magnet. The magnetised region would be used to measure the charge and momentum of the muons. This will improve the energy measurement for ν_μ CC interactions and allow disentangling ν_μ from $\bar{\nu}_\mu$ interactions. This upgrade will also allow separating the ν_τ and $\bar{\nu}_\tau$ interactions in the $\tau \to \mu$ decay mode. Figure 77 shows a schematic drawing of the different detector elements and the layout of the detector in the TI18 tunnel. The apparatus would be made of three different sections: the target with the electromagnetic calorimeter (highlighted in yellow), the hadronic calorimeter with the muon identification system (orange) followed downstream by a magnetised volume (green).

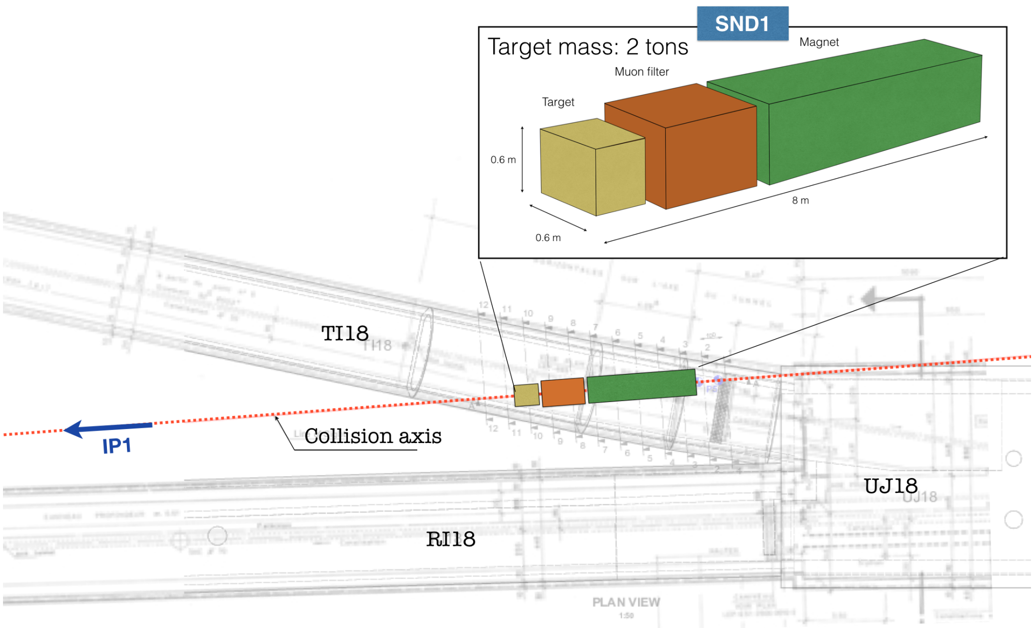

Figure 77: Schematic drawing of an upgraded version of the current detector beyond Run 3.

The explored pseudo-rapidity range would be similar to the current proposal, $7.2 < \eta < 8.6$. Given the high luminosity regime in Run 4, the goal would be to replace the emulsion films in the target region with electronic trackers, for a fully active apparatus. Assuming a larger target mass of about 2 tonnes and an integrated luminosity of $3000\,\mathrm{fb}^{-1}$, event yields would be a factor of about 50 larger than the current proposal, thus giving access to e.g. about 1000 ν_τ interactions.

Particularly interesting is the possibility of locating a neutrino detector in a region that gives overlap in pseudo-rapidity with LHCb. This will make it possible to achieve a combined measurement of the heavy-flavour production. The resulting knowledge about the associated production of neutrinos would reduce systematic uncertainties and allow directly measuring the neutrino cross-sections with high precision.

Therefore, the Collaboration is planning to continue with detector R&D and design a second apparatus based on same concept (segmented into three regions) and similar size to be placed in a different cavern underground at an angle with respect to the beam axis of about 22 mrad ($\eta \sim 4.5$). The search for a suitable location will include those around the LHCb experiment itself.

References

[1] SND@LHC collaboration, *Scattering and Neutrino Detector at the LHC*, Tech. Rep. CERN-LHCC-2020-013. LHCC-I-037, CERN, Geneva (Aug, 2020).

[2] LHCb collaboration, *Measurements of prompt charm production cross-sections in pp collisions at $\sqrt{s} = 13$ TeV*, *JHEP* **03** (2016) 159 [1510.01707].

[3] FASER collaboration, *Detecting and Studying High-Energy Collider Neutrinos with FASER at the LHC*, *Eur. Phys. J. C* **80** (2020) 61 [1908.02310].

[4] CTEQ collaboration, *Handbook of perturbative QCD: Version 1.0*, *Rev. Mod. Phys.* **67** (1995) 157.

[5] J.M. Conrad, M.H. Shaevitz and T. Bolton, *Precision measurements with high-energy neutrino beams*, *Rev. Mod. Phys.* **70** (1998) 1341 [hep-ex/9707015].

[6] J.A. Formaggio and G.P. Zeller, *From eV to EeV: Neutrino Cross Sections Across Energy Scales*, *Rev. Mod. Phys.* **84** (2012) 1307 [1305.7513].

[7] G. De Lellis, P. Migliozzi and P. Santorelli, *Charm physics with neutrinos*, *Phys. Rept.* **399** (2004) 227.

[8] D. Marfatia, D.W. McKay and T.J. Weiler, *New physics with ultra-high-energy neutrinos*, *Phys. Lett. B* **748** (2015) 113 [1502.06337].

[9] C.A. Argüelles et al., *White Paper on New Opportunities at the Next-Generation Neutrino Experiments (Part 1: BSM Neutrino Physics and Dark Matter)*, 1907.08311.

[10] M. Ackermann et al., *Astrophysics Uniquely Enabled by Observations of High-Energy Cosmic Neutrinos*, *Bull. Am. Astron. Soc.* **51** (2019) 185 [1903.04334].

[11] PDG, P.A. Zyla et al., *Review of Particle Physics*, *PTEP* **2020** (2020) .

[12] IceCube collaboration, *Measurement of the multi-TeV neutrino cross section with IceCube using Earth absorption*, *Nature* **551** (2017) 596 [1711.08119].

[13] M. Bustamante and A. Connolly, *Extracting the energy-dependent neutrino-nucleon cross section above 10 tev using icecube showers*, *Phys. Rev. Lett.* **122** (2019) 041101.

[14] Gargamelle collaboration, *Total Cross-Sections for electron-neutrino and anti-electron-neutrino Interactions and Search for Neutrino Oscillations and Decay*, *Nucl. Phys. B* **133** (1978) 205.

[15] C. Baltay et al., *$\nu_\mu - \nu_e$ Universality in Charged Current Neutrino Interactions*, *Phys. Rev. D* **41** (1990) 2653.

[16] ZEUS collaboration, *Measurement of high Q^2 charged current cross-sections in e+p deep inelastic scattering at HERA*, *Eur. Phys. J. C* **32** (2003) 1 [hep-ex/0307043].

[17] DONuT collaboration, *Final tau-neutrino results from the DONuT experiment*, *Phys. Rev. D* **78** (2008) 052002 [0711.0728].

[18] OPERA collaboration, *Discovery of τ Neutrino Appearance in the CNGS Neutrino Beam with the OPERA Experiment*, *Phys. Rev. Lett.* **115** (2015) 121802 [1507.01417].

[19] OPERA collaboration, *Final Results of the OPERA Experiment on ν_τ Appearance in the CNGS Neutrino Beam*, *Phys. Rev. Lett.* **120** (2018) 211801 [1804.04912].

[20] OPERA collaboration, *Final results of the search for $\nu_\mu \to \nu_e$ oscillations with the OPERA detector in the CNGS beam*, *JHEP* **06** (2018) 151 [1803.11400].

[21] A. De Rujula and R. Ruckl, *Neutrino and muon physics in the collider mode of future accelerators*, in *SSC Workshop: Superconducting Super Collider Fixed Target Physics*, pp. 571–596, 5, 1984, DOI.

[22] A. De Rujula, *NEUTRINO PHYSICS AT FUTURE COLLIDERS*, 1984.

[23] A. De Rujula, E. Fernandez and J. Gomez-Cadenas, *Neutrino fluxes at future hadron colliders*, *Nucl. Phys. B* **405** (1993) 80.

[24] F. Vannucci, *Neutrino physics at LHC/SSC*, Tech. Rep. LPNHE-93-03, Paris 6. Lab. Phys. Nucl. Théor. Hautes Enérg., Paris (Aug, 1993).

[25] CERN, *Large Hadron Collider Workshop: Aachen, Germany 4 - 9 Oct 1990. Large Hadron Collider Workshop, v.2*, (Geneva), CERN, 1990. 10.5170/CERN-1990-010-V-2.

[26] S. Buontempo, G. Dallavalle, G. De Lellis, D. Lazic and F. Navarria, *CMS-XSEN: LHC Neutrinos at CMS. Experiment Feasibility Study*, 1804.04413.

[27] N. Beni et al., *Physics Potential of an Experiment using LHC Neutrinos*, *J. Phys. G* **46** (2019) 115008 [1903.06564].

[28] FASER collaboration, *FASER: ForwArd Search ExpeRiment at the LHC*, 1901.04468.

[29] N. Beni et al., *Further studies on the physics potential of an experiment using LHC neutrinos*, *J. Phys. G* **47** (2020) 125004 [2004.07828].

[30] S. Alekhin et al., *A facility to Search for Hidden Particles at the CERN SPS: the SHiP physics case*, *Rept. Prog. Phys.* **79** (2016) 124201 [1504.04855].

[31] CHARM collaboration, *A Precise Determination of the Electroweak Mixing Angle from Semileptonic Neutrino Scattering*, *Z. Phys. C* **36** (1987) 611.

[32] A. Blondel et al., *Electroweak Parameters From a High Statistics Neutrino Nucleon Scattering Experiment*, *Z. Phys. C* **45** (1990) 361.

[33] M. Schumann, *Direct Detection of WIMP Dark Matter: Concepts and Status*, *J. Phys.* **G46** (2019) 103003 [1903.03026].

[34] P.J. Fox, *TASI Lectures on WIMPs and Supersymmetry*, *PoS* **TASI2018** (2019) 005.

[35] R.K. Ellis et al., *Physics Briefing Book*, 1910.11775.

[36] M. Battaglieri et al., *US Cosmic Visions: New Ideas in Dark Matter 2017: Community Report*, 1707.04591.

[37] CRESST collaboration, *First results from the CRESST-III low-mass dark matter program*, *Phys. Rev. D* **100** (2019) 102002 [1904.00498].

[38] SuperCDMS collaboration, *Projected Sensitivity of the SuperCDMS SNOLAB experiment*, *Phys. Rev. D* **95** (2017) 082002 [1610.00006].

[39] LDMX collaboration, *Light Dark Matter eXperiment (LDMX)*, 1808.05219.

[40] J. Beacham et al., *Physics Beyond Colliders at CERN: Beyond the Standard Model Working Group Report*, *J. Phys. G* **47** (2020) 010501 [1901.09966].

[41] K. Bondarenko et al., *Direct detection and complementary constraints for sub-GeV dark matter*, 1909.08632.

[42] L. Roszkowski, E.M. Sessolo and S. Trojanowski, *WIMP dark matter candidates and searches—current status and future prospects*, *Rept. Prog. Phys.* **81** (2018) 066201 [1707.06277].

[43] B. Batell, M. Pospelov and A. Ritz, *Exploring Portals to a Hidden Sector Through Fixed Targets*, *Phys.Rev.* **D80** (2009) 095024 [0906.5614].

[44] P. deNiverville, M. Pospelov and A. Ritz, *Observing a light dark matter beam with neutrino experiments*, *Phys.Rev.* **D84** (2011) 075020 [1107.4580].

[45] P. deNiverville, D. McKeen and A. Ritz, *Signatures of sub-GeV dark matter beams at neutrino experiments*, *Phys.Rev.* **D86** (2012) 035022 [1205.3499].

[46] MiniBooNE collaboration, *Low Mass WIMP Searches with a Neutrino Experiment: A Proposal for Further MiniBooNE Running*, 1211.2258.

[47] B. Batell, P. deNiverville, D. McKeen, M. Pospelov and A. Ritz, *Leptophobic Dark Matter at Neutrino Factories*, 1405.7049.

[48] D.E. Soper, M. Spannowsky, C.J. Wallace and T.M.P. Tait, *Scattering of Dark Particles with Light Mediators*, 1407.2623.

[49] B.A. Dobrescu and C. Frugiuele, *GeV-Scale Dark Matter: Production at the Main Injector*, *JHEP* **02** (2015) 019 [1410.1566].

[50] P. Coloma, B.A. Dobrescu, C. Frugiuele and R. Harnik, *Dark matter beams at LBNF*, *JHEP* **04** (2016) 047 [1512.03852].

[51] C. Frugiuele, *Probing sub-GeV dark sectors via high energy proton beams at LBNF/DUNE and MiniBooNE*, *Phys. Rev.* **D96** (2017) 015029 [1701.05464].

[52] P. deNiverville and C. Frugiuele, *Hunting sub-GeV dark matter with the NOνA near detector*, *Phys. Rev. D* **99** (2019) 051701 [1807.06501].

[53] G. Magill, R. Plestid, M. Pospelov and Y.-D. Tsai, *Millicharged particles in neutrino experiments*, 1806.03310.

[54] MiniBooNE DM collaboration, *Dark Matter Search in Nucleon, Pion, and Electron Channels from a Proton Beam Dump with MiniBooNE*, 1807.06137.

[55] SHiP collaboration, *Sensitivity of the SHiP experiment to light dark matter*, 2010.11057.

[56] R. Acquafredda et al., *The OPERA experiment in the CERN to Gran Sasso neutrino beam*, *JINST* **4** (2009) P04018.

[57] OPERA collaboration, *Observation of a first ν_τ candidate in the OPERA experiment in the CNGS beam*, *Phys. Lett. B* **691** (2010) 138 [1006.1623].

[58] OPERA collaboration, *Evidence for $\nu_\mu \to \nu_\tau$ appearance in the CNGS neutrino beam with the OPERA experiment*, *Phys. Rev.* **D89** (2014) 051102 [1401.2079].

[59] OPERA collaboration, *Search for $\nu_\mu \to \nu_e$ oscillations with the OPERA experiment in the CNGS beam*, *JHEP* **07** (2013) 004 [1303.3953].

[60] K. Roed, M. Brugger and G. Spiezia, *An overview of the radiation environment at the LHC in light of R2E irradiation activities*, *CERN-ATS-Note-2011-077 TECH* *https://cds.cern.ch/record/1382083* (May 9, 2012) .

[61] R.G. Alía et al., *LHC and HL-LHC: Present and Future Radiation Environment in the High-Luminosity Collision Points and RHA Implications*, *IEEE TRANSACTIONS ON NUCLEAR SCIENCE* **65** (January 2018) 448.

[62] T.T. Bohlen, F. Cerutti, M.P.W. Chin, A. Fassò, A. Ferrari, P.G. Ortega, A. Mairani, P.R. Sala, G. Smirnov, and V. Vlachoudis , *The FLUKA Code: Developments and Challenges for High Energy and Medical Applications* , *Nuclear Data Sheets* **120** (2014) 211.

[63] T.T. Böhlen, F. Cerutti, M.P.W. Chin, A. Fassò, A. Ferrari, P.G. Ortega et al., *The FLUKA Code: Developments and Challenges for High Energy and Medical Applications*, *Nucl. Data Sheets* **120** (2014) 211.

[64] A. Lechner et al., *Validation of energy deposition simulations for proton and heavy ion losses in the CERN Large Hadron Collider*, *Physical Review Accelerators and Beams* **22** (2019) 071003.

[65] S. Roesler, R. Engel, and J. Ranft, *The Monte Carlo Event Generator DPMJET-III*, *Proceedings of the Monte Carlo 2000 Conference, Lisbon, October 23-26 2000, (A. Kling, F. Barao, M. Nakagawa, L. Tavora, P. Vaz eds.) Springer-Verlag Berlin* (2001) 1033.

[66] A. Fedynitch, *Cascade equations and hadronic interactions at very high energies*, Nov, 2015. https://cds.cern.ch/record/2231593.

[67] D. Kramer et al., *LHC RadMon SRAM detectors used at different voltages to determine the thermal neutron to high energy hadron fluence ratio*, *IEEE Trans. Nucl. Sci.* **58** (2011) 1117.

[68] OPERA collaboration, *Procedure for short-lived particle detection in the OPERA experiment and its application to charm decays*, *Eur. Phys. J. C* **74** (2014) 2986 [1404.4357].

[69] N. Armenise et al., *High-speed particle tracking in nuclear emulsion by last-generation automatic microscopes*, *Nucl. Instrum. Meth. A* **551** (2005) 261.

[70] L. Arrabito et al., *Hardware performance of a scanning system for high speed analysis of nuclear emulsions*, *Nucl. Instrum. Meth. A* **568** (2006) 578 [physics/0604043].

[71] N. Armenise et al., *High-speed particle tracking in nuclear emulsion by last-generation automatic microscopes*, *Nucl. Instrum. Meth. A* **551** (2005) 261.

[72] A. Alexandrov et al., *A new generation scanning system for the high-speed analysis of nuclear emulsions*, *JINST* **11** (2016) P06002.

[73] A. Alexandrov et al., *A new fast scanning system for the measurement of large angle tracks in nuclear emulsions*, *JINST* **10** (2015) P11006.

[74] A. Alexandrov et al., *The Continuous Motion Technique for a New Generation of Scanning Systems*, *Sci. Rep.* **7** (2017) 7310.

[75] LHCb collaboration, *LHCb Tracker Upgrade Technical Design Report*, Report CERN-LHCC-2014-001. LHCB-TDR-015, http://cds.cern.ch/record/1647400 (2014).

[76] SHiP collaboration, *Measurement of associated charm production induced by 400 GeV/c protons*, Scientific Committee Paper CERN-SPSC-2017-033, SPSC-EOI-017, http://cds.cern.ch/record/2286844 (2017).

[77] PETsys electronics, “PETsys TOFPET2 ASIC.” https://www.petsyselectronics.com/web/public/products/1, 2020 (accessed December 30, 2020).

[78] D. Schug, V. Nadig, B. Weissler, P. Gebhardt and V. Schulz, *Initial Measurements with the PETsys TOFPET2 ASIC Evaluation Kit and a Characterization of the ASIC TDC*, in *IEEE Transactions on Radiation and Plasma Medical Sciences 2018*, 2018, DOI [1808.05833].

[79] V. Nadig, D. Schug, B. Weissler and V. Schulz, *Evaluation Of The PETsys TOFPET2 ASIC In Multi-Channel Coincidence Experiments*, 1911.08156.

[80] T. Harion et al., *STiC — a mixed mode silicon photomultiplier readout ASIC for time-of-flight applications*, *JINST* **9** (2014) C02003.

[81] C. Betancourt et al., *Application of large area SiPMs for the readout of a plastic scintillator based timing detector*, *JINST* **12** (2017) P11023 [1709.08972].

[82] SHiP collaboration, *A prototype for the SHiP timing detector*, *Nucl. Instrum. Meth. A* **979** (2020) 164398.

[83] Enclustra, "Mercury SA1." https://www.enclustra.com/en/products/system-on-chip-modules/mercury-sa1/.

[84] "TTC website." http://ttc.web.cern.ch/intro.html.

[85] "Joint COntrols Project (JCOP)." https://jcop.web.cern.ch/, 2020 (accessed December 30, 2020).

[86] P. Santos Diaz, *SND infrastructure and installation procedure*, Tech. Rep. , https://edms.cern.ch/document/2433805 (2020).

[87] D. Zambelli, *Calculation Memo for FASER*, Tech. Rep. (2020).

[88] P. Santos Diaz and R. Jacobsson, *Minor intervention in UJ18 in view of the SND proposal*, Tech. Rep. , https://edms.cern.ch/document/2424085/1.0 (2020).

[89] P. Santos Diaz and R. Jacobsson, *Preparatory works in UJ18/TI18 prior to installation of the SND detector*, Tech. Rep. , https://edms.cern.ch/document/2425670 (2020).

[90] A. Infatino, *RP considerations for FASER/FASERnu*, Tech. Rep. 2339274 v.1, CERN, https://edms.cern.ch/document/2339274/1 (2020).

[91] HSE, "Safety Regulation SR-SO: Responsibilities and Organisational Structure in Matters of Safety at CERN." https://edms.cern.ch/ui/file/1389540/LAST$_R$*ELEASED/SR* $-$ *SO*$_E$*.pdf*.

[92] M. Al-Turany, D. Bertini, R. Karabowicz, D. Kresan, P. Malzacher, T. Stockmanns et al., *The FairRoot framework*, *J. Phys. Conf. Ser.* **396** (2012) 022001.

[93] SHiP collaboration, *Measurement of the muon flux from 400 GeV/c protons interacting in a thick molybdenum/tungsten target*, *Eur. Phys. J. C* **80** (2020) 284.

[94] "Fluka website." https://fluka.cern.

[95] G. Battistoni et al., *Overview of the FLUKA code*, *Annals Nucl. Energy* **82** (2015) 10.

[96] T. Böhlen, F. Cerutti, M. Chin, A. Fassò, A. Ferrari, P. Ortega et al., *The FLUKA Code: Developments and Challenges for High Energy and Medical Applications*, *Nucl. Data Sheets* **120** (2014) 211.

[97] V. Boccone et al., *Beam-machine Interaction at the CERN LHC*, *Nucl. Data Sheets* **120** (2014) 215.

[98] R. Bruce et al., *Simulations and measurements of beam loss patterns at the CERN Large Hadron Collider*, *Phys. Rev. ST Accel. Beams* **17** (2014) 081004 [1409.3123].

[99] N. Mokhov, I. Rakhno, I. Tropin, F. Cerutti, L. Esposito and A. Lechner, *Energy deposition studies for the High-Luminosity Large Hadron Collider inner triplet magnets*, *Phys. Rev. ST Accel. Beams* **18** (2015) 051001 [1504.00594].

[100] A. Mereghetti, V. Boccone, F. Cerutti, R. Versaci and V. Vlachoudis, *The FLUKA LineBuilder and Element DataBase: Tools for Building Complex Models of Accelerator Beam Lines*, *Conf. Proc. C* **1205201** (2012) 2687.

[101] V. Vlachoudis, *Flair: A powerful but user friendly graphical interface for FLUKA*, in *International Conference on Mathematics, Computational Methods & Reactor Physics 2009*, pp. 790–800, 2009.

[102] CERN, *Revision of the high energy hadronic interaction models PHOJET/DPMJET-III*, (Geneva), CERN, 2015.

[103] LHCf collaboration, *Measurement of forward neutral pion transverse momentum spectra for $\sqrt{s}$ = 7TeV proton-proton collisions at LHC*, *Phys. Rev. D* **86** (2012) 092001 [1205.4578].

[104] A. Lechner et al., *Validation of energy deposition simulations for proton and heavy ion losses in the CERN Large Hadron Collider*, *Phys. Rev. Accel. Beams* **22** (2019) 071003.

[105] O. Bruning and L. Rossi, "The high luminosity large hadron collider." to be published by World Scientific.

[106] S. Roesler, R. Engel and J. Ranft, *The Monte Carlo event generator DPMJET-III*, in *Advanced Monte Carlo for radiation physics, particle transport simulation and applications. Proceedings, Conference, MC2000, Lisbon, Portugal, October 23-26, 2000*, p. 1033, 2000, DOI [hep-ph/0012252].

[107] C. Andreopoulos et al., *The GENIE Neutrino Monte Carlo Generator*, *Nucl. Instrum. Meth. A* **614** (2010) 87 [0905.2517].

[108] GEANT4 collaboration, *GEANT4: A Simulation toolkit*, *Nucl. Instrum. Meth. A* **506** (2003) 250.

[109] T. Sjöstrand, S. Mrenna and P.Z. Skands, *A Brief Introduction to PYTHIA 8.1*, *Comput. Phys. Commun.* **178** (2008) 852 [0710.3820].

[110] T. Sjostrand, S. Mrenna and P.Z. Skands, *PYTHIA 6.4 Physics and Manual*, *JHEP* **05** (2006) 026 [hep-ph/0603175].

[111] V. Tyukov, I. Kreslo, Y. Petukhov and G. Sirri, *The FEDRA Framework for emulsion data reconstruction and analysis in the OPERA experiment*, *Nucl. Instrum. Meth. A* **559** (2006) 103.

[112] R. Brun, F. Rademakers and S. Panacek, *ROOT, an object oriented data analysis framework*, in *CERN School of Computing (CSC 2000)*, pp. 11–42, 2000, DOI.

[113] SHiP collaboration, *Reconstruction of 400 GeV/c proton interactions with the SHiP-charm project*, .

[114] P.T.G.P. de Bryas Dexmiers D'Archiac, "Development and commissioning of a machine learning algorithm for real time reconstruction of electromagnetic showers with a scintillating fibres tracker." EPFL, Master Thesis, 2020. https://lphe.epfl.ch/publications/theses/Master_Thesis_Paul_De_Bryas.pdf.

[115] S. Mitra, "Implementation of a Machine Learning Regression Algorithm for Energy Reconstruction of Neutrino-induced Particle Showers using a Scintillating Fibres Tracker at the SND@LHC." Maastricht University, Bacherlor's Thesis, 2020. https://www.nikhef.nl/~jdevries/Mitra_thesis.pdf.

[116] J.G.H. Cobussen, "A Machine Learning algorithm for energy reconstruction and binary classification of elastic and inelastic neutrino scattering events at the SND@LHC." Maastricht University, Bacherlor's Thesis, 2020. https://www.nikhef.nl/~jdevries/Cobussen_thesis.pdf.

[117] C. Hoppner, S. Neubert, B. Ketzer and S. Paul, *A Novel Generic Framework for Track Fitting in Complex Detector Systems*, *Nucl. Instrum. Meth. A* **620** (2010) 518 [0911.1008].

[118] T. Adye, *Unfolding algorithms and tests using RooUnfold*, in *PHYSTAT 2011*, (Geneva), pp. 313–318, CERN, 2011, DOI [1105.1160].

[119] P. Nason, *A New method for combining NLO QCD with shower Monte Carlo algorithms*, *JHEP* **11** (2004) 040 [hep-ph/0409146].

[120] S. Frixione, P. Nason and C. Oleari, *Matching NLO QCD computations with Parton Shower simulations: the POWHEG method*, *JHEP* **11** (2007) 070 [0709.2092].

[121] S. Alioli, P. Nason, C. Oleari and E. Re, *A general framework for implementing NLO calculations in shower Monte Carlo programs: the POWHEG BOX*, *JHEP* **06** (2010) 043 [1002.2581].

[122] NNPDF collaboration, *Parton distributions for the LHC Run II*, *JHEP* **04** (2015) 040 [1410.8849].

[123] L.A. Harland-Lang, A.D. Martin, P. Motylinski and R.S. Thorne, *Parton distributions in the LHC era: MMHT 2014 PDFs*, *Eur. Phys. J. C* **75** (2015) 204 [1412.3989].

[124] R. Gauld, J. Rojo, L. Rottoli and J. Talbert, *Charm production in the forward region: constraints on the small-x gluon and backgrounds for neutrino astronomy*, *JHEP* **11** (2015) 009 [1506.08025].

[125] J. Bellm et al., *Herwig 7.0/Herwig++ 3.0 release note*, *Eur. Phys. J. C* **76** (2016) 196 [1512.01178].

[126] S. Porteboeuf, T. Pierog and K. Werner, *Producing Hard Processes Regarding the Complete Event: The EPOS Event Generator*, in *45th Rencontres de Moriond on QCD and High Energy Interactions*, pp. 135–140, Gioi Publishers, 2010 [1006.2967].

[127] NuTeV collaboration, *Precise Measurement of Dimuon Production Cross-Sections in ν_μ Fe and $\bar{\nu}_\mu$ Fe Deep Inelastic Scattering at the Tevatron.*, *Phys. Rev. D* **64** (2001) 112006 [hep-ex/0102049].

[128] A. Kayis-Topaksu et al., *Measurement of charm production in neutrino charged-current interactions*, *New J. Phys.* **13** (2011) 093002 [1107.0613].

[129] OPERA collaboration, *First observation of a tau neutrino charged current interaction with charm production in the OPERA experiment*, Eur. Phys. J. C **80** (2020) 699 [1912.11012].

[130] SHiP collaboration, *SHiP Experiment - Progress Report*, Scientific Committee Paper CERN-SPSC-2019-010. SPSC-SR-248, CERN, https://cds.cern.ch/record/2654870 (Jan, 2019).

[131] P. deNiverville, C.-Y. Chen, M. Pospelov and A. Ritz, *Light dark matter in neutrino beams: production modelling and scattering signatures at MiniBooNE, T2K and SHiP*, Phys. Rev. **D95** (2017) 035006 [1609.01770].

[132] L. Buonocore, C. Frugiuele, F. Maltoni, O. Mattelaer and F. Tramontano, *Event generation for beam dump experiments*, JHEP **05** (2019) 028 [1812.06771].

[133] S. Naaz, J. Singh and R. Singh, *DUNE prospect for leptophobic dark matter*, 2004.10996.

[134] J. Feng, I. Galon, F. Kling and S. Trojanowski, *ForwArd Search ExpeRiment at the LHC*, Phys. Rev. **D97** (2018) 035001 [1708.09389].

[135] I. Boiarska, K. Bondarenko, A. Boyarsky, M. Ovchynnikov, O. Ruchayskiy and A. Sokolenko, *Light scalar production from Higgs bosons and FASER 2*, 1908.04635.

[136] J. Alwall, R. Frederix, S. Frixione, V. Hirschi, F. Maltoni, O. Mattelaer et al., *The automated computation of tree-level and next-to-leading order differential cross sections, and their matching to parton shower simulations*, JHEP **07** (2014) 079 [1405.0301].

[137] A. Alloul, N.D. Christensen, C. Degrande, C. Duhr and B. Fuks, *FeynRules 2.0 - A complete toolbox for tree-level phenomenology*, Comput. Phys. Commun. **185** (2014) 2250 [1310.1921].

[138] N.D. Christensen and C. Duhr, *FeynRules - Feynman rules made easy*, Comput. Phys. Commun. **180** (2009) 1614 [0806.4194].

[139] A. Buckley, J. Ferrando, S. Lloyd, K. Nordstrom, B. Page, M. Rufenacht et al., *LHAPDF6: parton density access in the LHC precision era*, Eur. Phys. J. **C75** (2015) 132 [1412.7420].

[140] I.M. Shoemaker and L. Vecchi, *Unitarity and Monojet Bounds on Models for DAMA, CoGeNT, and CRESST-II*, Phys. Rev. D **86** (2012) 015023 [1112.5457].

[141] H. An, X. Ji and L.-T. Wang, *Light Dark Matter and Z' Dark Force at Colliders*, JHEP **07** (2012) 182 [1202.2894].

[142] BES collaboration, *Search for the invisible decay of J / psi in psi(2S) — pi+ pi- J / psi*, Phys. Rev. Lett. **100** (2008) 192001 [0710.0039].

[143] BNL-E949 collaboration, *Study of the decay $K^+ \to \pi^+ \nu\bar{\nu}$ in the momentum region $140 < P_\pi < 199$ MeV/c*, Phys. Rev. D **79** (2009) 092004 [0903.0030].

[144] M.S. Atiya et al., *Search for the decay pi0 —> gamma X*, *Phys. Rev. Lett.* **69** (1992) 733.

[145] T. Sjöstrand, S. Ask, J.R. Christiansen, R. Corke, N. Desai, P. Ilten et al., *An Introduction to PYTHIA 8.2*, *Comput. Phys. Commun.* **191** (2015) 159 [1410.3012].

[146] D. Banerjee et al., *Dark matter search in missing energy events with NA64*, *Phys. Rev. Lett.* **123** (2019) 121801 [1906.00176].

[147] MiniBooNE DM collaboration, *Dark Matter Search in Nucleon, Pion, and Electron Channels from a Proton Beam Dump with MiniBooNE*, *Phys. Rev. D* **98** (2018) 112004 [1807.06137].

[148] The BGV Collaboration collaboration, *Non-invasive lhc transverse beam size measurement using inelastic beam-gas interactions*, *Phys. Rev. Accel. Beams* **22** (2019) 042801.

[149] S. Aoki et al., *A Hybrid Experiment to Search for Beauty Particles*, *Nucl. Instrum. Meth. A* **274** (1989) 64.

[150] CHORUS collaboration, *The CHORUS experiment to search for muon-neutrino –> tau-neutrino oscillation*, *Nucl. Instrum. Meth. A* **401** (1997) 7.

[151] S. Aoki et al., *Dstau: study of tau neutrino production with 400 gev protons from the cern-sps*, *Journal of High Energy Physics* **2020** (2020) .